



Light Dark Matter Searches and Modeling of Charge Propagation Effects in SuperCDMS Cryogenic Silicon R&D Detectors with eV-Scale Sensitivity

Zur Erlangung des akademischen Grades eines
Doktors der Naturwissenschaften (Dr. rer. nat.)

von der KIT-Fakultät für Physik des
Karlsruher Instituts für Technologie (KIT)

genehmigte

Dissertation

von

Alexander Zaytsev

aus Troitzk

Tag der mündlichen Prüfung: 03.11.2023
Referent: Prof. Dr. Ralph Engel
Korreferentin: Prof. Dr. Belina von Krosigk
Betreuerin: Prof. Dr. Belina von Krosigk

Abstract

Many cosmological and astrophysical observations point to the existence of Dark Matter (DM) in our and other galaxies. However, despite decades-long history of direct searches for DM particles, there is no confirmed detection to this day. In view of very stringent experimental constraints on DM candidates with masses above $1 \text{ GeV}/c^2$, lighter DM candidates have been attracting more attention in recent years. Searches for such DM candidates require detectors with either a low energy threshold or a mechanism to amplify the interaction energy. SuperCDMS cryogenic silicon R&D detectors called High-Voltage eV-resolution (HVeV) detectors possess both of these properties.

HVeV detectors, consisting of silicon crystals instrumented with phonon sensors, have been operated in two modes, differing by the voltage applied across the crystal: the High-Voltage (HV) mode and the Zero-Volt (0V) mode. Particles interacting with the detector material generate both phonon and ionization signals. In the HV mode, the ionization signal is amplified by the electric field and converted into an additional comparatively large phonon signal, which is then measured by the phonon sensors. In the 0V mode, however, the ionization signal is not amplified, and the sensors only measure the initial interaction energy.

In the work described in this dissertation, we start with developing an improved model of the amount of energy amplification generated by charges moving in the electric field when detectors are operated in the HV mode. We note that the expected detector response is different depending on whether particle interactions occur in the bulk of the detector or on the detector's surface. This property can be used in future DM searches for statistical discrimination between DM and background events.

After that, we take advantage of the versatility and eV-scale sensitivity of HVeV detectors conducting two DM search analyses. In the first analysis we derive the first HVeV exclusion limit on the strength of Light Dark Matter (LDM) interactions with nuclei using the data acquired in the 0V mode in an unshielded facility. We observe a spectrum of background events, steeply rising towards the energy threshold which we set below 10 eV. This unknown background prevents us from reaching unexplored DM parameter space.

In the second analysis, we study the HV data from the first underground HVeV run with multiple detectors operated in the same housing. We apply an anti-coincidence event selection to suppress external backgrounds and derive exclusion limits on the strength of var-

ious DM-electron interactions, namely the DM-electron recoils via heavy and light mediator, Dark Photon (DP) absorption and Axion-Like Particle (ALP) absorption. We improve the limits obtained in previous HVeV analyses by up to a factor of 20 and reach ALP absorption parameter space, previously unexplored by direct searches.

Acknowledgements

I would like to express my gratitude to all the people who directly or indirectly contributed to the work described in this dissertation.

First and foremost, I am immensely grateful to my supervisor, Belina von Krosigk, for her unwavering support throughout this journey. Her guidance, expertise, and encouragement have been indispensable. I am truly fortunate to have had such an understanding mentor by my side.

I am particularly grateful to the SuperCDMS colleagues who worked together with me on the projects featured in this dissertation.

Matt Wilson deserves the credit for developing the Charge Trapping and Impact Ionization (CTII) model. Matt did all the heavy lifting, calculating the analytical solutions for all the combinations of the considered effects. What was left for me is to incorporate these solutions into the general detector response model.

During the 0VeV analysis, I had the pleasure to work together with Runze (Tom) Ren. Tom performed the data processing, calibration, mean baseline and temperature live-time selection, and worked on the HV–0V comparative analysis, while I worked on the DM search with the 0V data, taking advantage of the analysis steps that Tom performed for the 0V data.

I wish to thank all the analyzers who worked together with me on the HVeV Run 3 analysis. Specifically, Taylor Aralis, who worked on the calibration and the final exclusion limit calculation, Corey Bathurst, who developed the χ^2 event selection, and Derek Sincavage, who helped with the mean baseline event selection. A very special thanks goes to Valentina Novati, who supervised this analysis from its very beginning until its completion, ensuring that we, the analyzers, stayed on the right track.

My gratitude goes to all the people who made the HVeV experiments happen: Noah Kurinsky, Enectalí Figueroa-Feliciano, Ziqing Hong, Benjamin Schmidt, Ran Chen, Valentina, Tom, and other current and former members of the SuperCDMS Northwestern and Fermilab groups.

I also want to thank all the other members of the SuperCDMS Collaboration who provided their feedback and support throughout this work. I thank the reviewers of the 0VeV and HVeV Run 3 analyses, namely Tarek Saab, Adam Mayer, Elham Azadbakht, Wolfgang Rau,

Emanuele Michielin, Stefan Zatschler, Francisco Ponce, and Sunil Golwala. Thanks to Steve Yellin, Ray Bunker, and Miriam Diamond for asking the right questions at the right time. Thanks to Mike Kelsey for teaching me detector physics. Thanks to Noah for inspiration and support. And a very special thanks to Ziqing, who was always there to answer all the questions I had during these years.

I am thankful to Francesco Toschi, Sukeerthi Dharani, and Aliya Nigamova for helping proofread this manuscript.

I also thank Ralph Engel for agreeing to act as my official supervisor at KIT.

Lastly, I would like to extend my thanks to the people who accompanied me on this journey on a more personal level.

Hanno, Matt, Sukee, Francesco, it was a pleasure working with you in the same group! Although we shared only a very limited time together in the office, this time was certainly memorable. Thank you, Hanno, for all the protein breaks we had together and for always being wholeheartedly supportive. Thank you, Sukee, for being the best “long-distance office-mate”, keeping me company on slack even when I was working from home. Thank you, Matt, for being an inspiration to me in terms of diligence and the rigor with which you approach your work. Thank you, Francesco, for the kind words and support that you gave me at the most difficult time.

My dear Aliya, thank you for being a pillar of strength in my life. None of this would have been possible without you.

Declaration of Authorship

I hereby certify that this dissertation has been composed by me and is based on my own work, unless stated otherwise. No other person's work has been used without due acknowledgement. All references and verbatim extracts have been quoted, and all sources of information have been specifically acknowledged.

List of Acronyms

0V	Zero-Volt
ADC	Analog-to-Digital Converter
ADR	Adiabatic Demagnetization Refrigerator
ALP	Axion-Like Particle
BAO	Baryon Acoustic Oscillation
CCD	Charge-Coupled Device
CDF	Cumulative Distribution Function
CL	Confidence Level
CMB	Cosmic Microwave Background
CP	Charge-Parity symmetry
CT	Charge Trapping
CTII	Charge Trapping and Impact Ionization
DAQ	Data Acquisition
DCRC	Detector Control and Readout Card
DM	Dark Matter
DP	Dark Photon
FAA	Ferric Ammonium Alum
GDF	Gaussian Derivative Filter
GGG	Gadolinium Gallium Garnet
HV	High-Voltage
HVeV	High-Voltage eV-resolution
iZIP	interleaved Z-sensitive Ionization and Phonon
II	Impact Ionization
ΛCDM	Lambda Cold Dark Matter

LDM	Light Dark Matter
LEE	Low Energy Excess
LHC	Large Hadron Collider
MACHO	Massive Astrophysical Compact Halo Object
MF	Matched Filter
MC	Monte Carlo
MOND	Modified Newtonian Dynamics
NEXUS	Northwestern Experimental Underground Site
NTL	Neganov–Trofimov–Luke
OF	Optimum Filter
OF0	Optimum Filter with no time shift
OFL	Optimum Filter with Limited time shift
OPF	Optimum Filter with Pile-up
OI	Optimum Interval
PCB	Printed Circuit Board
PDF	Probability Density Function
PMF	Probability Mass Function
PSD	Power Spectral Density
QCD	Quantum Chromodynamics
QET	Quasiparticle-trap-assisted Electrothermal-feedback Transition-edge sensor
RF	Radio Frequency
ROI	Region of Interest
RQ	Reduced Quantity
RTD	Resistance Temperature Detector
SHM	Standard Halo Model
SM	Standard Model
SI	Spin-Independent
SQUID	Superconducting Quantum Interference Device
SUSY	Supersymmetry
TES	Transition-Edge Sensor
TeVeS	Tensor-Vector-Scalar gravity

TTL Transistor–Transistor Logic

WIMP Weakly Interacting Massive Particle

Contents

1	Dark Matter	1
1.1	Evidence for Dark Matter	1
1.1.1	Galactic Rotation Curves	2
1.1.2	Gravitational Lensing	3
1.1.3	Cosmic Microwave Background	3
1.2	Dark Matter Candidates	5
1.2.1	Weakly Interacting Massive Particles	5
1.2.2	Light Dark Matter	6
1.2.3	Dark Photons	9
1.2.4	Axions and Axion-Like Particles	9
1.2.5	Other Candidates	10
1.3	Current State of Direct Dark Matter Searches	10
1.3.1	Searches via Nuclear Recoils	11
1.3.2	Searches via Electron Interactions	13
1.4	SuperCDMS SNOLAB Experiment	14
2	Cryogenic Semiconductor Detectors	17
2.1	Signals in Cryogenic Semiconductor Detectors	17
2.1.1	Ionization	17
2.1.2	Phonons	19
2.2	SuperCDMS Phonon Sensors: QETs	22
2.2.1	Transition-Edge Sensor	22
2.2.2	Electrothermal Feedback	22
2.2.3	Quasiparticle Traps	24
2.3	SuperCDMS Detectors	24
2.3.1	iZIP Detectors	25
2.3.2	HV Detectors	26
2.3.3	HVeV Detectors	26

3 Charge Trapping and Impact Ionization Model	29
3.1 Exponential CTII model	30
3.1.1 CTII Effects in Surface Events	31
3.1.2 CTII Effects in Bulk Events	33
3.1.3 Detector Response with Improved CTII Modeling	35
3.1.4 Discussion	37
4 0VeV: Light Dark Matter Nuclear Recoil Search	40
4.1 Introduction	40
4.2 Experimental Setup	41
4.3 Data Processing	42
4.3.1 Optimum Filter	43
4.3.2 Triggering and Processing	44
4.4 Energy Calibration	45
4.5 Data Selection	48
4.5.1 Live-Time Selection Criteria	49
4.5.2 Data-quality Selection Criteria	52
4.5.3 Final Energy Spectrum	53
4.6 Dark Matter Signal Model	53
4.7 Dark Matter-Nucleon Scattering Cross Section Limit	56
4.7.1 Upper Limit on the Dark Matter-Nucleon Scattering Cross Section .	57
4.7.2 Earth Shielding Effect	58
4.8 Discussion	62
5 HVeV Run 3. Dark Matter Absorption and Electron Recoil Search	63
5.1 Introduction	63
5.2 Experimental Setup, Data Acquisition and Data Processing	65
5.2.1 Experimental Setup	65
5.2.2 Data Acquisition	66
5.2.3 Pulse Template	67
5.2.4 Triggering	67
5.2.5 Energy Reconstruction and Reduced Quantities	72
5.3 Measured Energy Spectrum	73
5.3.1 Science Data Live-time Selection Criteria	74
5.3.2 Laser Data Selection Criteria	78
5.3.3 Data-Quality Selection Criteria	80
5.3.4 Energy Calibration	84
5.3.5 Energy Spectrum Used in the Limit Setting	87
5.4 Dark Matter Signal Models	87

5.4.1	Theoretical Interaction Energy Spectra	89
5.4.2	Detector Response Model	89
5.4.3	Expected Dark Matter Counts in the Experiment	92
5.5	Dark Matter Limits	92
5.5.1	Poisson Counting Method	94
5.5.2	Combination of Multiple Limits	95
5.5.3	Selection of Energy Regions	96
5.5.4	Limits without Earth Shielding Effects	101
5.5.5	Earth Shielding Effect	103
5.6	Discussion	107
6	Conclusion and Outlook	109
Bibliography		112

List of Figures

1.1	Rotation curve of M33	2
1.2	Bullet Cluster	4
1.3	CMB angular power spectrum	5
1.4	Exclusion limits on SI DM-nucleon recoils, DM-electron recoils and DP absorption	12
1.5	Low energy excess in solid-state detectors	13
1.6	SuperCDMS setup	15
1.7	SuperCDMS projections	16
2.1	Ionization model in Si	19
2.2	Illustration of a particle interaction in an Si crystal	21
2.3	Illustration of a resistance-temperature curve in a superconducting transition	23
2.4	TES bias circuit	24
2.5	Illustration of a normal and saturated TES pulse	24
2.6	QET energy transport and design geometry	25
2.7	iZIP and HV detectors	26
2.8	HVeV detector	27
2.9	HVeV QET masks	28
3.1	CTII solutions for single $e^- h^+$ -pair surface events	34
3.2	CTII solutions for single $e^- h^+$ -pair bulk events	36
3.3	Dark Photon and leakage events spectra in the improved and simple CTII models	38
3.4	Comparison of the simple and improved CTII models for the case of multi-eh events	38
4.1	HVeV Run 2 detector	42
4.2	HVeV Run 2 setup	42
4.3	OF kernel construction diagram	45
4.4	0VeV trigger example	46
4.5	HVeV Run 2 calibration	48

4.6	0VeV live-time selection	50
4.7	Histogram of the HVeV Run 2 event interarrival time	51
4.8	Illustration of the periodic noise rejection	51
4.9	Examples of pulses not consistent with the laser template	52
4.10	HVeV Run 2 χ^2 selection	53
4.11	HVeV Run 2 χ^2 selection efficiency	54
4.12	0VeV data spectrum	54
4.13	Examples of reconstructed energy distributions in the HVeV Run 2 simulation with injected pulses	55
4.14	DM-nucleon recoil signal models with 0VeV detector response	56
4.15	Illustration of Optimum Interval limit-setting procedure	58
4.16	0VeV 90% CL limit DM-nucleon scattering cross section exclusion limit	59
4.17	DM wind direction in 0VeV	60
4.18	Earth shielding effect illustration	60
4.19	0VeV DM-nucleon scattering cross section exclusion region with the Earth shielding effect	61
5.1	HVeV Run 2 DM-electron cross section limit	64
5.2	HVeV Run 2 burst event	64
5.3	HVeV Run 3 experimental setup	66
5.4	HVeV Run 3 DAQ triggering	67
5.5	HVeV Run 3 pulse templates	68
5.6	GDF and MF comparison	69
5.7	HVeV Run 3 trigger efficiency	70
5.8	HVeV Run 3 trigger alignment	71
5.9	HVeV Run 3 noise PSDs	72
5.10	HVeV Run 3 mean baseline distribution	75
5.11	HVeV Run 3 mean baseline selection illustration	75
5.12	HVeV Run 3 interarrival event time distribution	76
5.13	Anti-coincidence live-time selection illustration	77
5.14	HVeV Run 3 event rates with consecutively applied live-time selection criteria	79
5.15	HVeV Run 3 laser data energy spectrum	80
5.16	HVeV Run 3 χ^2 data-quality selection	82
5.17	Efficiency of the HVeV Run 3 χ^2 data-quality selection	82
5.18	HVeV Run 3 $\Delta\chi^2$ data-quality selection	83
5.19	Efficiency of the HVeV Run 3 $\Delta\chi^2$ data-quality selection	83
5.20	χ^2 and $\Delta\chi^2$ selection performance test	83
5.21	HVeV Run 3 combined data-quality selection efficiency	83

5.22 HVeV Run 3 event rates with consecutively applied live-time and data-quality selection criteria	84
5.23 HVeV Run 3 laser data energy spectrum with consecutively applied selection criteria	85
5.24 HVeV Run 3 energy calibration	87
5.25 HVeV Run 3 day-to-day gain variations	88
5.26 HVeV Run 3 science data energy spectrum	88
5.27 HVeV Run 3 energy resolution model	91
5.28 HVeV Run 3 DM signal models	93
5.29 HVeV Run 3 peak selection procedure	98
5.30 HVeV Run 3 peak selection procedure with exposure scaling	99
5.31 HVeV Run 3 peak selection results	100
5.32 HVeV Run 3 90% CL limits	102
5.33 Earth shielding effect illustration	105
5.34 HVeV Run 3 90% CL exclusion regions with Earth shielding effect taken into account	105
5.35 Order of magnitude estimation of the Earth shielding effect on the DM absorption limits	107
6.1 HVeV Run 4 detector holder	111

"We have already discovered it!
Through its gravitational interaction"

Arthur McDonald, Vienna, 2023

Chapter 1

Dark Matter

The work described in this dissertation is a small step in a huge sea of efforts directed towards resolving one of the most intriguing fundamental questions of modern physics — the nature of the Dark Matter (DM). For half a century, since the renowned observation of the rotation curve of the Andromeda Galaxy by Vera Rubin in 1970 [1], it has been apparent that there is more matter in the Universe than we can see. According to a widely accepted standard cosmological model, Lambda Cold Dark Matter (Λ CDM), the DM constitutes almost 85% of the mass of matter in the Universe [2]. The leading theory of its nature is that the DM consists of one or several new fundamental particle species. Therefore, we hope to either (i) detect it directly on Earth as it interacts with regular matter, (ii) create it in colliders, or (iii) observe it through its annihilation products in cosmic rays. All three discovery channels are being extensively explored by physicists around the world. The work described in this dissertation is a contribution to the efforts related to the first category, the direct detection.

In this chapter, we start with a short overview of evidence for DM existence and its particle nature (Section 1.1), discuss possible particle DM candidates (Section 1.2), review the current state of direct DM searches (Section 1.3), and then discuss the SuperCDMS SNOLAB experiment and its projected sensitivities (Section 1.4).

1.1 Evidence for Dark Matter

The first scientifically motivated claim of the existence of massive non-luminous matter in galaxy clusters came from the pioneering work of Fritz Zwicky in 1933. While studying redshifts in galaxy clusters, he observed a large dispersion of galactic velocities within the Coma Cluster [3]. Applying the virial theorem, he inferred that the mass of the cluster must be significantly larger than the observed luminous mass [4]. Forty years later, this puzzling observation began to be supported by more and more compelling evidence for the invisible mass, aptly named the Dark Matter. This section presents arguably the most convincing among them.

1.1.1 Galactic Rotation Curves

Assuming Newton's law of gravity, the velocities of rotation of gravitationally bound stars on circular orbits around galactic centers should follow the relation:

$$v = \sqrt{\frac{GM(r)}{r}}, \quad (1.1)$$

where G is the gravitational constant, r is the distance from the galaxy center, and $M(r)$ is the mass concentrated within the radius r . Considering that most of the luminous mass in spiral galaxies is concentrated within their central bulges, the velocities of stars outside of the bulge should decrease as $r^{-1/2}$.

Measurements of galactic rotation curves played a revolutionary role in the shaping of the DM paradigm. The first spectroscopic measurement of the Andromeda Galaxy rotation curve, performed by Vera Rubin using an image tube spectrograph, showed an unexpectedly flat behavior at radii up to 24 kpc [1]. Radio observations of the 21 cm hydrogen line in numerous other spiral galaxies demonstrated flat rotation curves that extend far beyond the visible stellar disks [5]. Many more similar measurements confirmed this behavior in other galaxies, as shown, for example, in a compilation of rotation curves in Ref. [6].

To explain the observed velocity trends, there should be an additional non-luminous mass, with a distribution that extends beyond the visible parts of the galaxies and beyond the extent of their measured nondecreasing rotation curves. These formations are called DM halos. Figure 1.1 shows the rotation curve of the Triangulum Galaxy (M33) with a suggested distribution of visible stellar mass, gaseous mass and DM halo mass that together provide a good fit to the observed velocity curve [7].

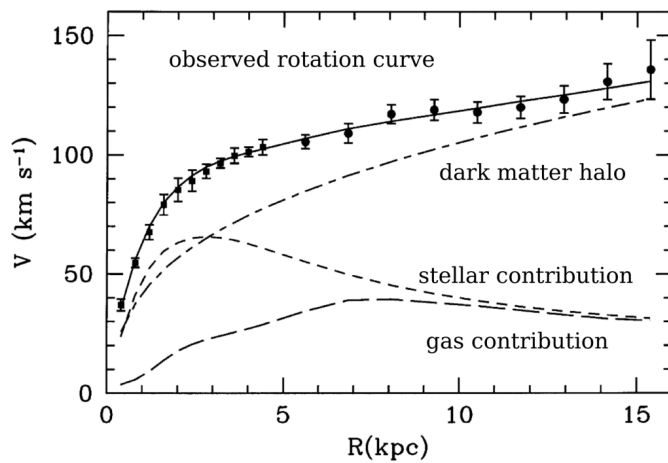


Figure 1.1: Rotation curve of the Triangulum Galaxy (points) with the best-fitting model (solid line) consisting of the Dark Matter halo (dash-dotted line), the stellar disk (short-dashed line), and the gas contribution (long-dashed line). Adapted from Ref. [7] by J. Rothe [8].

1.1.2 Gravitational Lensing

A seemingly logical expectation would be that the invisible mass around galaxies consists of Massive Astrophysical Compact Halo Objects (MACHOs), such as neutron stars, white dwarfs, red dwarfs, planets, or black holes. Although invisible on their own, such objects would still be detectable via the gravitational lensing effect — the bending of light due to the presence of a massive object [9]. The EROS collaboration monitored 33 million stars in the Milky Way over a period of 6.7 years in an attempt to detect variations in their brightness caused by MACHOs via the gravitational lensing effect. Only one microlensing event was observed, whereas \sim 39 events would be required to explain the invisible mass of the galaxy [10]. This observation rules out MACHOs as the main component of the DM halos.

The strong gravitational lensing effect is also used to infer the mass distribution of galaxy clusters based on their ability to distort the light from the objects behind them. A gravitational lensing analysis of the CL 0024 galaxy cluster showed a smooth concentration of DM centered near the brightest galaxies, comprising more than 98% of the cluster's mass [11].

Both, the rotation curves and the lensing effect, use purely gravitational arguments in favor of DM existence. An alternative explanation for the observed discrepancies between these gravitational effects and the mass of visible matter could be obtained with a modified theory of gravity. Modified Newtonian Dynamics (MOND) is an umbrella term for various attempts to create a new theory of gravity that resolves the observed phenomena without the need for DM. A currently leading MOND theory, the Bekenstein's Tensor-Vector-Scalar gravity (TeVeS), is capable of explaining the rotation curves and most of the lensing observations [12]. However, there is one gravitational observation that poses a significant challenge to TeVeS and to other MOND theories — the Bullet Cluster.

The Bullet Cluster is a result of a collision of two galactic clusters. Most of its luminous mass is concentrated in X-ray emitting plasma, the distribution of which is dramatically affected by the collision. However, the gravitational map of the cluster inferred from the lensing effect shows that most of the mass of the colliding clusters have passed through each other unaffected (see Figure 1.2). The mismatch between the distributions of luminous mass and the distribution of mass inferred from the lensing effect was aptly titled “A direct empirical proof of the existence of Dark Matter”, as it cannot be explained by a modification of the laws of gravity [13].

1.1.3 Cosmic Microwave Background

Perhaps the most compelling evidence in support of the existence of DM lies in the success of the Λ CDM cosmological model in correctly predicting various phenomena such as the formation of large-scale structures, the abundance of hydrogen and helium, and, most significantly, the structure of the Cosmic Microwave Background (CMB).

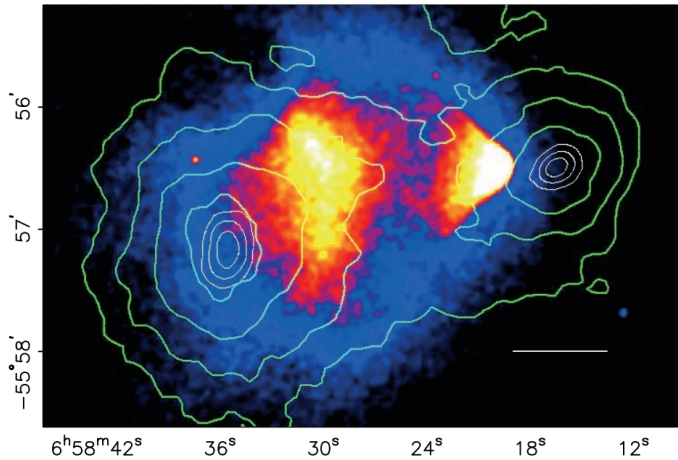


Figure 1.2: X-ray image of the Bullet Cluster with an overlaid gravitational lensing reconstruction of its mass distribution shown by the green contours. Unlike the distribution of X-ray emitting luminous mass, the overall mass distribution seems largely unaffected by the collision of the galaxy clusters. Figure from Ref. [13].

According to the Λ CDM model, the early Universe, consisting of a hot plasma of baryons, photons, positrons and electrons, was cooling down in the course of its expansion. 380000 years after the Big Bang, the ambient temperature decreased below the ionization energy of helium and hydrogen, binding the electrons and baryons to neutral atoms. Since then, photons decoupled from matter, forming the remnant radiation background of the Universe. As the Universe continued to expand, the energy of the decoupled radiation has been redshifted to the microwave region, giving it its name, the Cosmic *Microwave Background* (CMB) [14]. The temperature of CMB in the present Universe is 2.7255 ± 0.0006 K [15].

As measured by COBE [16], WMAP [17], and Planck [18], the CMB radiation is almost perfectly isotropic, with temperature fluctuations of the order of $\delta T/T \sim 10^{-5}$. These fluctuations are believed to be an imprint of the density distribution of matter in the early Universe. If at the time of radiation decoupling, a photon was in a denser area of the Universe, it experienced a slightly larger redshift and therefore became slightly colder than the average CMB radiation. Conversely, photons from less populated regions appear hotter. To explain the current large scale formations in the Universe without the DM, CMB temperature fluctuations of the order of $\delta T/T \sim 10^{-3}\text{--}10^{-4}$ would be necessary. The existence of non-baryonic matter, the DM, is required to explain the observed small magnitude of the fluctuations [19].

A demonstrative success of the Λ CDM model is in its description of the oscillatory behavior of the angular power spectrum of the CMB (Figure 1.3). As the DM accumulates in regions of high density, it creates gravitational wells, attracting baryon-photon plasma. The plasma contracts and then expands again under its own pressure, creating what is called Baryon Acoustic Oscillations (BAOs). As the radiation decouples from the matter, it carries

the remnants of the BAO in its angular power spectrum [20]. The six-parametric Λ CDM model fits the observed spectrum with a convincing precision, providing the best-to-date measurement of the Universe composition. According to the latest measurement by the Planck collaboration, baryonic matter comprises only 4.9% of the total energy density of the Universe, the DM — 26.4%, with the remaining energy assigned to the so-called dark energy which drives the expansion of the Universe [21].

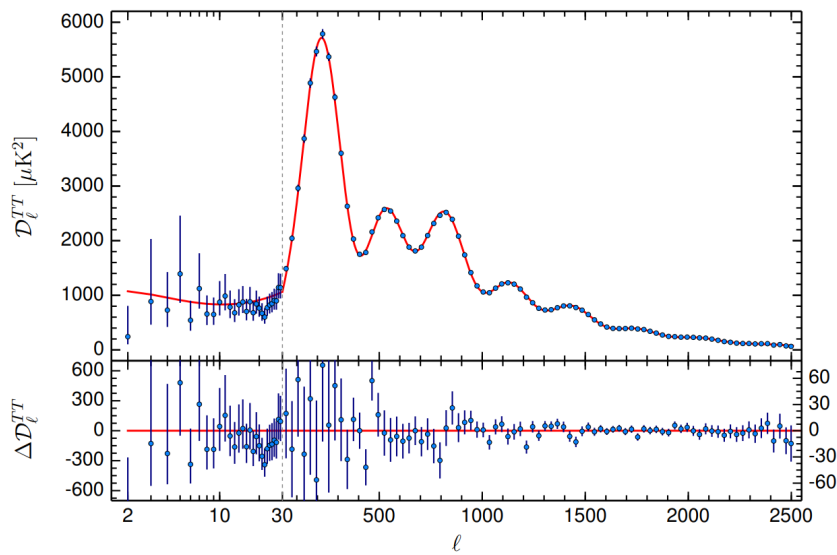


Figure 1.3: Cosmic Microwave Background temperature angular power spectrum measured by the Planck telescope, fitted with the six-parametric Λ CDM model, with fit residuals shown on the lower plot. Figure from Ref. [22].

1.2 Dark Matter Candidates

With the abundant evidence supporting the existence of DM, many DM candidates have been proposed over the years. Some of the proposed hypotheses are being experimentally tested, while others are beyond the reach of the current experimental technologies. In this section, we discuss DM candidates that arguably have the highest potential to be probed by ongoing or planned direct DM searches. We start with the Weakly Interacting Massive Particles (WIMPs) and then focus on the candidates and the detection mechanisms probed by the analyses described in Chapters 4 and 5 of this dissertation.

1.2.1 Weakly Interacting Massive Particles

WIMP is perhaps the most motivated DM candidate, as it is the simplest realization of the Λ CDM model. Within this concept, the DM particles exist in abundance in the early Universe, being created from and annihilated to lighter particles in thermal equilibrium. As

the Universe expands and cools down, the DM creation and annihilation processes cease and the DM freezes out of thermal equilibrium, creating the relic abundance. To provide the relic abundance observed today, the DM self-annihilation cross section should be of the order of $\langle \sigma_a v \rangle \sim 10^{-26} \text{ cm}^3/\text{s}$, where v is the relative velocity of annihilating particles. This value corresponds to a particle with a mass of the order of $100 \text{ GeV}/c^2$, interacting at the weak scale (hence the name Weakly Interacting Massive Particle) [23]. Coincidentally, a particle with such properties is also predicted within the scope of the Supersymmetry (SUSY) theory aiming to resolve the hierarchy problem of particle physics [24]. The ability of WIMPs to simultaneously solve two fundamental problems of modern physics made them the primary goal of direct detection searches over the last four decades. By now, most of the motivated WIMP parameter space of interaction strength *versus* mass has been probed and excluded by ton-scale liquid Xe detectors [25–27] (see Section 1.3). Moreover, no evidence of SUSY has been found at the Large Hadron Collider (LHC) [28]. As the hope to discover WIMPs gradually dwindles, other DM candidates have started to gain more and more attention in recent years.

1.2.2 Light Dark Matter

At masses below $2 \text{ GeV}/c^2$, the annihilation cross section of WIMPs that interact via the Standard Model (SM) weak interaction becomes too small to explain the relic DM abundance. This limit is known as the Lee-Weinberg limit [29]. DM candidates with masses below $2 \text{ GeV}/c^2$, collectively referred to as Light Dark Matter (LDM) or sub-GeV DM, require a different interaction mechanism to escape the Lee-Weinberg limit.

The common concept of the LDM models is that rather than interacting via the SM weak force, the DM constitutes a new “dark sector” of particles with a weak “portal” to the SM. There are multiple proposed production mechanisms of LDM, reviewed, for example, in Ref. [30]:

- **Freeze-out DM:** a force mediator different from Z-boson allows the thermal freeze-out of DM particles below the Lee-Weinberg limit of $2 \text{ GeV}/c^2$ [31, 32];
- **Freeze-in DM:** in this scenario, the DM is not thermalized with the SM particles, and its abundance is explained by the annihilation of SM particles into the DM particles [33];
- **Asymmetric DM:** in this model, a hypothesized primordial asymmetry in the DM sector, akin to the baryonic matter-antimatter asymmetry, leads to a relic abundance after the DM annihilation [34];
- **3-to-2 freeze-out:** here the final DM abundance is defined by a number-changing 3-to-2 process of Strongly Interacting Massive Particles (SIMPs), while they stay in a thermal equilibrium with the SM particles via elastic scattering [35];

- **Elastically Decoupling Relic (ELDER):** similarly to the previous case, strongly self-interacting DM stays in thermal equilibrium with the SM particles, but the relic abundance is determined by the cross section of the elastic scattering rather than by the cross section of the 3-to-2 process [36].

Since LDM is one of the DM candidates searched for within this dissertation, we describe the detection mechanisms utilized in our analyses.

Regardless of the relic density formation mechanism, the relic DM particles are characterized by the cross section of their interactions with SM particles and searched for in direct detection experiments. One of the possible interaction channels is the Spin-Independent (SI) elastic scattering on nuclei. The scattering kinematics, derived for WIMP searches in Ref. [37], also applies to LDM searches. Assuming that 100% of the DM halo consists of a DM species with a SI DM-nucleon elastic scattering cross section σ_n^{SI} , the differential nucleon recoil rate is given by:

$$\frac{dR}{dE_{\text{NR}}} = \frac{\rho_{\text{DM}}}{2\mu_n^2 m_{\text{DM}}} \sigma_n^{\text{SI}} A^2 F^2(E_{\text{NR}}) \int_{v_{\min}}^{\infty} \frac{1}{v} f(\mathbf{v}) d^3 \mathbf{v}, \quad (1.2)$$

where E_{NR} is the recoil energy, ρ_{DM} is the local DM density, m_{DM} is the mass of the DM particle, A is the number of nucleons in the nucleus used as a target, $F(E_{\text{NR}})$ is the Helm nuclear form-factor [38], and μ_n is the reduced DM-nucleon mass:

$$\mu_n = \frac{m_{\text{DM}} m_n}{m_{\text{DM}} + m_n}, \quad (1.3)$$

where m_n is the mass of a nucleon.

In Equation 1.2, \mathbf{v} is the DM velocity with respect to the target and $f(\mathbf{v})$ is its distribution. The DM velocity distribution in the galactic rest frame $f(\mathbf{v}_{\text{gal}})$ is defined by the Maxwellian distribution truncated at the galactic escape velocity v_{esc} [39, 40]:

$$f(\mathbf{v}_{\text{gal}}) = \frac{N}{(\pi v_0)^{3/2}} \exp\left(-\frac{|\mathbf{v}_{\text{gal}}|^2}{v_0}\right) \Theta(v_{\text{esc}} - |\mathbf{v}_{\text{gal}}|), \quad (1.4)$$

$$\mathbf{v}_{\text{gal}} = \mathbf{v} + \mathbf{v}_E, \quad (1.5)$$

where N is the normalization constant, Θ is the Heaviside step function, v_0 is the asymptotic value of the Maxwellian velocity distribution (average DM speed in the galactic frame), and \mathbf{v}_E is the average Earth velocity with respect to the DM halo.

The lower bound of the integral in Equation 1.2 is the minimum value of the DM velocity that can result in a recoil energy E_{NR} , given by:

$$v_{\min} = \sqrt{\frac{m_N E_{\text{NR}}}{2\mu_N^2}}, \quad (1.6)$$

with m_N and μ_N being the nucleus mass and the reduced DM-nucleus mass respectively. Then, as derived in Ref. [37], the integral has an exponential solution:

$$\int_{v_{\min}}^{\infty} \frac{1}{v} f(\mathbf{v}) d^3 v \sim \exp \left(-\frac{m_N E_{\text{NR}}}{\mu_N^2 v_0^2} \right). \quad (1.7)$$

Equations 1.2 and 1.7 show that for the low DM masses, large recoil energies are kinematically suppressed. Probing nuclear recoils of DM with a mass of ~ 100 MeV/ c^2 requires an experiment with an energy threshold of ~ 10 eV or smaller. In the analysis described in Chapter 4, we set a threshold lower than 10 eV and derive an exclusion limit on the SI DM-nucleon scattering cross section using Equation 1.2, with a correction derived in Refs. [23, 41] for the edge case scenario in which v_{\min} is close to the galactic escape velocity.

To circumvent the kinematic suppression of energy transferred to a heavy nucleus, DM-electron recoils have been suggested as a more readily detectable mechanism of interaction of DM with masses as low as 1 MeV/ c^2 [42, 43]. As derived in Ref. [42], in LDM models in which the DM particles interact with SM particles through a new vector boson A' kinetically mixed with the SM hypercharge U(1) $_Y$, the differential DM-electron recoil rate in a crystal target is given by:

$$\frac{dR}{d \ln E_r} = N_{\text{cell}} \sigma_e \alpha \frac{m_e^2}{\mu_e^2} \frac{\rho_{\text{DM}}}{m_{\text{DM}}} \int \frac{E_r}{q} \eta(v_{\min}(q, E_r)) F_{\text{DM}}(q)^2 |f_{\text{crystal}}(q, E_r)|^2 d \ln q, \quad (1.8)$$

where E_r is the electron recoil energy, σ_e is the DM-electron recoil cross section, N_{cell} is the number of crystal cells in the target, α is the fine structure constant, m_e is the electron mass, μ_e is the DM-electron reduced mass, and q is the momentum transfer. $\eta(v_{\min})$ is an integral over the DM velocities as in the nuclear recoil case:

$$\eta(v_{\min}) \equiv \int_{v_{\min}(q, E_r)}^{\infty} \frac{1}{v} f(\mathbf{v}) d^3 v, \quad (1.9)$$

with $v_{\min}(q, E_r)$ given by:

$$v_{\min}(q, E_r) = \frac{E_r}{q} + \frac{q}{2m_{\text{DM}}}. \quad (1.10)$$

The DM form factor $F_{\text{DM}}(q)$ is defined as:

$$F_{\text{DM}}(q) = \frac{m_{A'}^2 + \alpha^2 m_e^2}{m_{A'}^2 + q^2} \simeq \begin{cases} 1, & m_{A'} \gg \alpha m_e, \\ \frac{\alpha^2 m_e^2}{q^2}, & m_{A'} \ll \alpha m_e, \end{cases} \quad (1.11)$$

where $m_{A'}$ is the mass of the DM force mediator. Depending on the mass of the mediator, two cases are usually considered: $F_{\text{DM}} = 1$ with a heavy mediator $m_{A'} \gg \alpha m_e$, and $F_{\text{DM}} \propto 1/q^2$ with an ultra-light mediator $m_{A'} \ll \alpha m_e$.

The electronic structure of the target is taken into account by the dimensionless crystal

form factor $f_{\text{crystal}}(q, E_r)$. Several ways of calculating this form factor for various materials have been recently suggested. In the analysis described in Chapter 5, we rely on the density-functional theory calculations, described in Ref. [42] and released as a public software package known as QEDark [44]. Other suggested approaches for the crystal form factor calculation can be found in Refs. [45–47].

1.2.3 Dark Photons

Staying in the framework of the new gauge group $U(1)_D$ with the vector boson A' , it has been suggested that the boson A' itself, referred to as the Dark Photon (DP), constitutes the DM abundance that is gravitationally observed today [48, 49]. A possible production mechanism in this model is the misalignment mechanism, in which the DP field value is not at a potential minimum in the early Universe due to quantum fluctuations during inflation (exponential expansion of space in the first moments after the Big Bang). As the field attempts to minimize its potential, it oscillates around the minimum. Quantizations of different modes of such oscillations represent a macroscopic number of nonrelativistic DP particles A' . With a sufficiently weak coupling to the SM, the lifetime of DPs can be long enough for them to survive until today [50, 51].

A promising detection mechanism for this type of DM is its absorption by electrons. As derived in Refs. [49, 52], the DP absorption rate in a semiconductor target is given by:

$$R = \frac{1}{\rho} \frac{\rho_{\text{DM}}}{m_{A'}} \varepsilon_{\text{eff}}^2 \sigma_1(m_{A'}), \quad (1.12)$$

where ρ is the density of the target material, $\sigma_1(m_{A'})$ is the real part of the energy-dependent complex conductivity of the target, taken for the energy equal to the DP mass, and ε_{eff} is the effective kinetic mixing of the DP and SM photon that takes into account in-medium effects. The effective mixing angle is related to the true mixing parameter ε as

$$\varepsilon_{\text{eff}}^2 = \frac{\varepsilon^2 m_{A'}^2}{(m_{A'}^2 - 2m_{A'}\sigma_2 + \sigma_2^2 + \sigma_1^2)}, \quad (1.13)$$

where σ_2 is the imaginary part of the complex conductivity [49, 52].

Taking into account the nonrelativistic DM velocities in the DM halo, the absorbed DP energy in direct-detection experiments is approximated by its rest energy, $m_{A'}$. As a result, the expected energy spectrum of the DP-electron absorption is a delta function at $m_{A'}$ with an amplitude given by Equation 1.12.

1.2.4 Axions and Axion-Like Particles

Axions have originally been proposed in particle physics to solve the Charge-Parity (CP) violation problem in strong interactions. CP-violating processes are predicted by the theory of

Quantum Chromodynamics (QCD), but have not been experimentally observed. A mechanism, known as the Peccei-Quinn mechanism, suppresses the CP-violating processes and predicts the existence of a pseudo-Goldstone boson with a non-zero mass, the axion [53–55].

Produced via the misalignment mechanism, QCD axions are a good candidate for DM [56]. However, due to their very small interaction strength, directly linked to their very small mass ($\sim 10^{-5}$ – 10^{-3} eV/ c^2 [57–60]), their direct detection with current technologies is extremely challenging [61].

A broader DM candidate is an Axion-Like Particle (ALP) — a general pseudo-Goldstone boson of a global U(1) symmetry breaking with the same production mechanism as for the axion. As the ALPs are not linked to the strong CP violation problem, the requirements for their mass and coupling to the SM are relaxed, allowing them to exist in an experimentally accessible region of the mass-*versus*-coupling parameter space [61].

As in the case of DPs, absorption of ALPs by electrons is a viable detection mechanism. The rate of absorption in a semiconductor target is derived in Ref. [52] and is given by:

$$R = \frac{\rho_{DM}}{\rho} \frac{3g_{ae}^2 m_a}{16\pi\alpha m_e^2} \sigma_1(m_a), \quad (1.14)$$

where g_{ae} is the axion-electron coupling and m_a is the mass of the ALP. The rest of the variables are as defined before.

1.2.5 Other Candidates

There are a multitude of other plausible candidates for DM, spanning tens of orders of magnitude in mass. For example, some of the DM candidates mentioned in the latest topical report of the Snowmass community [62] include:

- **WIMPzillas:** nonthermally produced WIMPs with masses in the range 10^{12} – 10^{16} GeV/ c^2 [63];
- **Primordial Black Holes:** black holes formed in the early Universe via gravitational collapse of regions of extreme density [64];
- **Strangelets:** macroscopic “nuggets” of u, d and s quarks, formed in a first-order QCD phase transition [65];
- **Sterile Neutrinos:** right-hand chirality neutrinos, interacting only gravitationally, mixed with the SM neutrinos via the Higgs mechanism [66].

1.3 Current State of Direct Dark Matter Searches

The large number of various DM candidates motivates a multitude of experimental efforts directed toward investigating different regions of DM parameter space, normally expressed

as a two-dimensional plane of DM mass and some interaction strength parameter (different for different DM models). There are three main methods of experimental DM detection:

- **Direct detection:** In these experiments, DM particles constituting the galactic DM halo are expected to interact with the detector's material, depositing some energy which can be detected via various channels. We provide a brief overview of the direct detection experiments in this section, focusing on the channels relevant to this dissertation;
- **Indirect detection:** Indirect detection experiments search for products of DM self-annihilation into SM particles or for products of DM decays. They can potentially be observed in cosmic rays, for example, as an excess in γ -ray, positron, or antiproton spectra. For an overview of indirect DM searches see Refs. [67, 68];
- **Production in colliders:** colliders explore the possibility of producing DM particles from SM particles. The DM is searched for as the missing energy and momentum in the collision products (see, for example, Ref. [69]).

“Light shining through the wall” experiments utilize another way of DM detection which does not fit the above classification. These experiments probe the coupling between photons and bosonic DM by shining a laser through a wall in the presence of a strong magnetic field. The photons are expected to convert into the dark boson state, pass through the wall, and then convert back into their ordinary state, causing a signal in the detector behind the wall (see, for example, the ALPS-II experiment [70]).

1.3.1 Searches via Nuclear Recoils

We focus on direct DM searches, starting with a long-standing field of DM-nucleon recoil searches. With no confirmed direct DM detection to this date, we describe the experiments and technologies in terms of the extent of their ability to probe various regions of the DM parameter space. Figure 1.4 (a) shows the two-dimensional parameter space of the SI DM-nucleon cross section *versus* DM mass with a selection of the latest exclusion limits from direct detection experiments. Liquid noble gas detectors are especially successful at constraining the DM parameter space at masses above a few GeV/c^2 . Their ability to simultaneously measure ionization and scintillation signals allows them to discriminate electron- and nuclear-recoil events, efficiently rejecting electron-recoil backgrounds. In addition, their relatively easy scalability allows them to reach exposures above the ton-year scale. These factors allowed to improve the sensitivity of the liquid noble gas detectors by two orders of magnitude in the last decade [71]. The next generation liquid Xenon experiment, DARWIN, is expected to probe the nuclear recoil parameter space above a few GeV/c^2 down to the “neutrino fog” — the limitation from the irreducible neutrino background with large systematic uncertainties [71, 72].

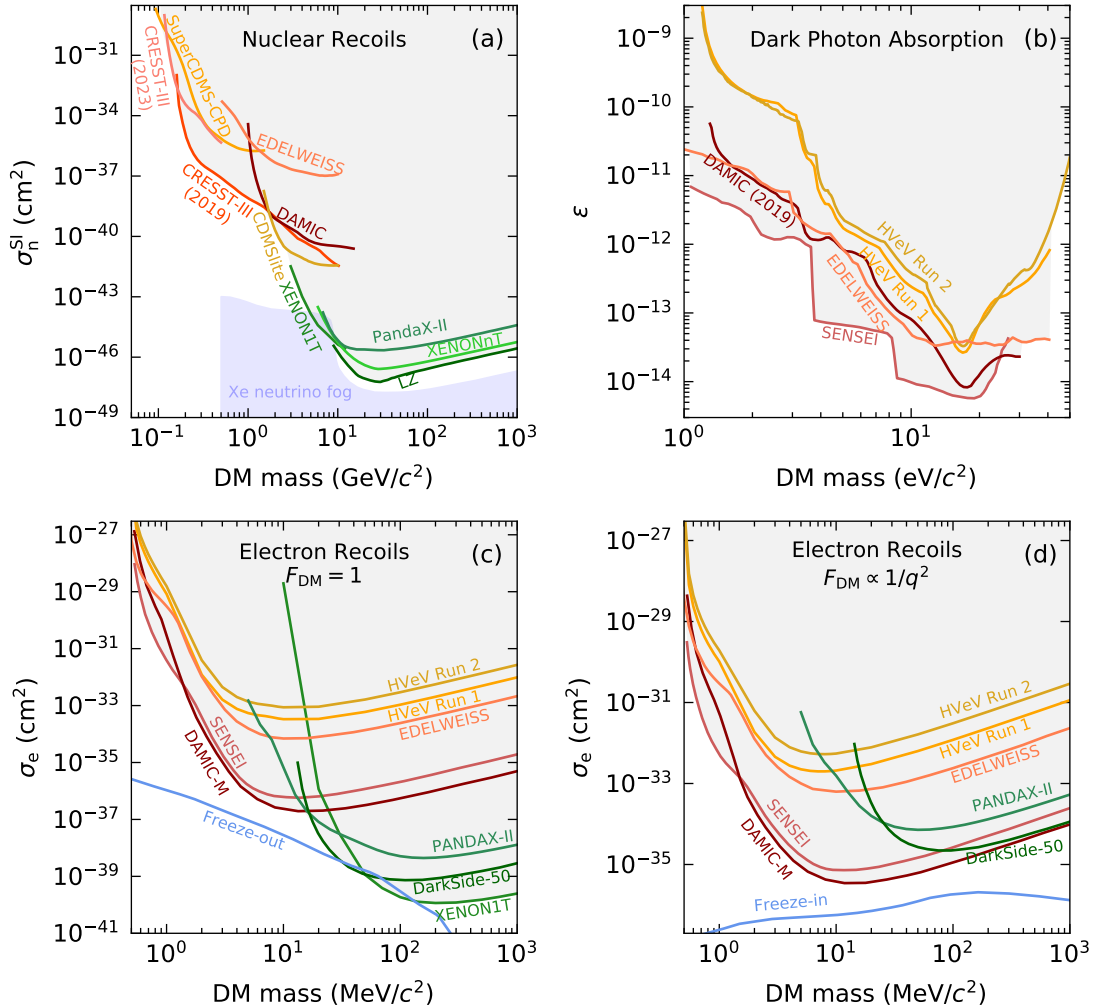


Figure 1.4: Current most stringent exclusion limits on the Dark Matter (DM) parameter space of different DM models. Gray shaded areas show the excluded regions. (a) Parameter space of nuclear recoil searches: Spin-Independent DM-nucleon recoil cross section *versus* DM mass. Shown are exclusion limits from LZ [25], XENON1T (2021) [73], XENONnT [26], PandaX-II [27], CDMSlite [74], DAMIC [75], EDELWEISS [76], CRESST-III (2019) [77], CRESST-III (2023) [78], and SuperCDMS-CPD [79]. Blue shaded area shows the onset of neutrino fog for a xenon target [71]. (b) Parameter space of the searches for Dark Photon (DP) absorption: DP mixing angle *versus* DP mass. Shown are exclusion limits from SENSEI [80], EDELWEISS [81], DAMIC [82], and SuperCDMS HVeV Run 1 [83] and Run 2 [84]. (c-d) Parameter space of electron recoil searches: DM-electron recoil cross section *versus* DM mass for DM form factor $F_{\text{DM}} = 1$ (c) and $F_{\text{DM}} \propto 1/q^2$ (d). Shown are exclusion limits from XENON1T (2019) [85], DarkSide-50 [86], PandaX-II [87], DAMIC-M [88], SENSEI [80] (recasted as in Ref. [88]), EDELWEISS [81], SuperCDMS HVeV Run 1 [83] and Run 2 [84]. Theoretical predictions for the parameter values required to produce the DM relic abundance via freeze-out or freeze-in mechanisms are shown in blue [89].

To probe sub-GeV DM masses, an energy threshold below 100 eV is required. Cryogenic crystalline phonon detectors have a low enough noise level to reach thresholds as low as ~ 10 eV, which allows them to probe DM masses down to $\sim 100 \text{ MeV}/c^2$ (see Refs. [78, 79], as well as Chapter 4 of this dissertation). However, the reach of these detectors to low cross-section values is at this time limited by the so-called Low Energy Excess (LEE), the excesses of events at energies below a few hundred eV, reported by many experiments probing such low energies with solid-state detectors (see Figure 1.5) [90]. Due to the differences in the observed LEE spectra between experiments and their variability over time, a DM origin is mostly excluded or strongly disfavored. Moreover, it is possible that the sources of LEEs are different in different experiments.

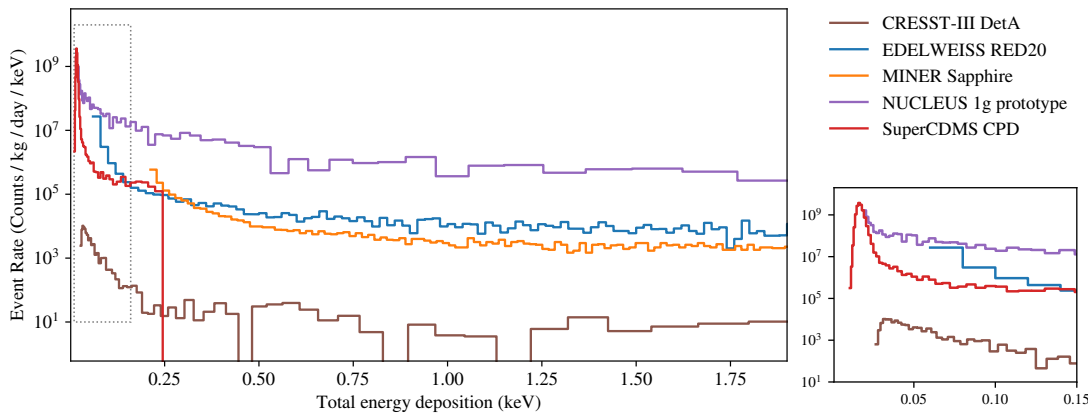


Figure 1.5: Energy spectra measured by solid-state detectors. The measurements demonstrate a steep rise in observed event rates at energies below a few hundred eV. This feature is referred to as the Low Energy Excess (LEE) in the Light Dark Matter search community and is not currently well understood. The Dark Matter hypothesis is disfavored to the differences in observed rates and their time dependencies. The inset shows the spectra zoomed-in at energies below 150 eV. Shown data are released within Ref. [90] rather than in individual publications, therefore we do not provide references to individual shown experiments. Figure from Ref. [90].

1.3.2 Searches via Electron Interactions

Figure 1.4 (b-d) shows the parameter space of DP absorption searches (b), as well as DM-electron recoil searches mediated via a heavy mediator ($F_{\text{DM}} = 1$) (c) or via an ultra-light mediator ($F_{\text{DM}} \propto 1/q^2$) (d). DM interactions with electrons cause ionization signals in detectors. Relatively low ionization energies in semiconductors make them excellent materials for probing such interactions. Currently, the leading technology in terms of probing low-energy DM-electron interactions is the Charge-Coupled Devices (CCDs), capable of registering a single ionized electron (see the exclusion limits from SENSEI [80] and DAMIC [82, 88] in

Figure 1.4). However, the LEE problem affects not only the nuclear recoil searches, but also the searches for DM-electron interactions [90, 91].

Cryogenic semiconductor detectors with ionization signal amplification, such as SuperCDMS HVeV detectors introduced in Section 2.3.3, are also capable of resolving events with single-electron ionization signals. In addition, they provide an excellent time resolution and can be operated with and without amplification of the ionization signal — features, that the CCDs lack. In Chapter 5, we analyze the SuperCDMS HVeV Run 3 data, where we utilize the HVeV time resolution to suppress the LEE events that were detrimental to the HVeV Run 1 [83] and Run 2 [84] DM searches. We set new exclusion limits on DM-electron recoil cross section, as well as on the DP and ALP absorption parameter space.

1.4 SuperCDMS SNOLAB Experiment

The Cryogenic Dark Matter Search (CDMS) project is a series of direct-detection experiments, utilizing cryogenic semiconductor detectors to search primarily for WIMPs. CDMS took the first DM search data in 1996. With the data taken at the Soudan Underground Laboratory, Minnesota, CDMS papers published in 2004, 2006 and 2009 set the world-leading exclusion limits on the SI DM-nucleon recoil cross section for DM masses above $15 \text{ GeV}/c^2$ [92–94].

In the following years, as the liquid noble gas detectors started to take over the lead in WIMP searches above $\sim 10 \text{ GeV}/c^2$, the focus of cryogenic solid-state experiments started to shift towards lower masses. Data from the CDMS low ionization threshold experiment (CDMSlite) set the world-leading (at the time) limits on the SI nuclear recoils for DM masses between 1.6 and $6 \text{ GeV}/c^2$ [74, 95, 96]. At the same time, the CDMS upgraded experiment, SuperCDMS Soudan, has completed its operation [97], paving the way towards the next step in CDMS history — SuperCDMS SNOLAB.

The goal of SuperCDMS SNOLAB is to probe LDM with masses down to $0.5 \text{ GeV}/c^2$ via nuclear recoils. Secondary scientific goals include searches for electron-coupled DM interactions, such as LDM electron recoils, and DP and ALP electron absorption. Improved detector design will allow for a lower energy threshold, compared to previous generations of CDMS experiments. In addition, the location at the SNOLAB underground facility provides an excellent shielding from cosmic rays with its overburden of 6010 mwe (meter water equivalent). The initial payload will consist of four towers of six detectors each. Two different types of detectors will be deployed, HV and interleaved Z-sensitive Ionization and Phonon (iZIP) detectors (see Section 2.3 for more detail), each having germanium (Ge) and silicon (Si) variants. The mix of detector technologies and target materials will allow for a better understanding of background, which is crucially important in view of the LEE observed in solid-state detectors.

Figure 1.6 shows a schematic diagram of the SuperCDMS SNOLAB assembly, placed

on top of a seismic platform. Detectors, organized in towers, will be placed in a multilayer copper housing, the SNOBOX, and cooled down to the base temperature of 15 mK with a dilution refrigerator. The SNOBOX is surrounded by layers of different shields, including a magnetic shield, a radon diffusion barrier, low-activity lead, polyethylene and water shields. The shields and the SNOBOX are penetrated by an electronic stem (E-Stem) which houses cable connections, and a cryogenic stem (C-Stem) which connects the SNOBOX with the fridge [98].

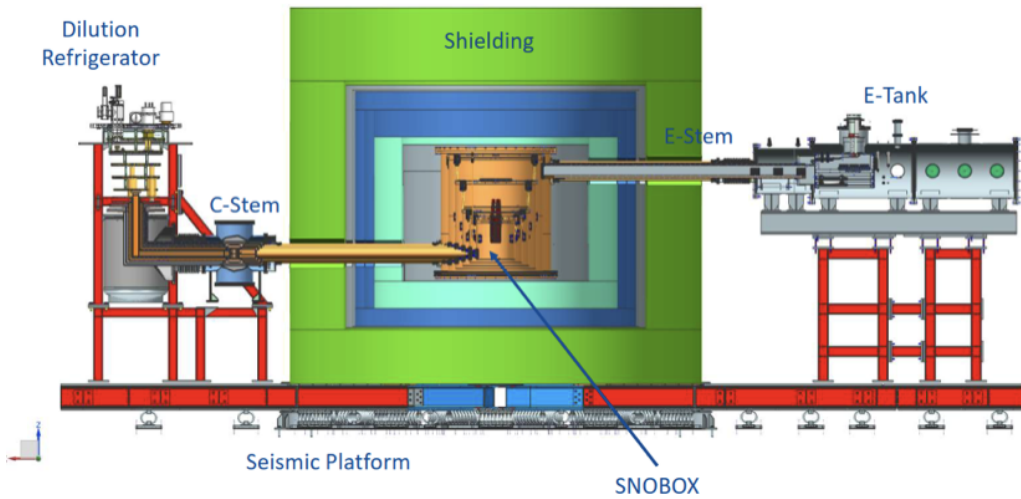


Figure 1.6: Rendering of the SuperCDMS SNOLAB experiment. The copper detector housing, SNOBOX, is surrounded by layers of different shields, penetrated by the cryogenic stem (C-Stem) and the electronic stem (E-Stem). The C-stem is connected to the dilution refrigerator. The E-stem is connected to the electronic tank (E-Tank). The assemble rests on top of a seismic platform. Figure from Ref. [98]

Figure 1.7 shows the expected sensitivities of the HV and iZIP Si and Ge SuperCDMS SNOLAB detectors to various DM parameter spaces, including (a) SI DM-nucleon recoils; (b) DP-electron absorption; (c) DM-electron recoils via heavy mediator ($F_{\text{DM}} = 1$); and (d) DM-electron recoils via ultra-light mediator ($F_{\text{DM}} \propto 1/q^2$). These sensitivity expectations are based on spectrum simulations with included known backgrounds, as described in Ref. [98], with no LEE. For the case of nuclear recoils, sensitivities are shown based on two different limit-setting methods: the Optimum Interval (OI) method that does not subtract known backgrounds (dashed lines) [99, 100] and the profile likelihood ratio method that incorporates knowledge of backgrounds and thus produces stronger limits (solid lines). The expected sensitivities cover many square decades of unexplored DM parameter space, providing a strong motivation for the SuperCDMS SNOLAB program. The start of the data taking is planned for 2024.

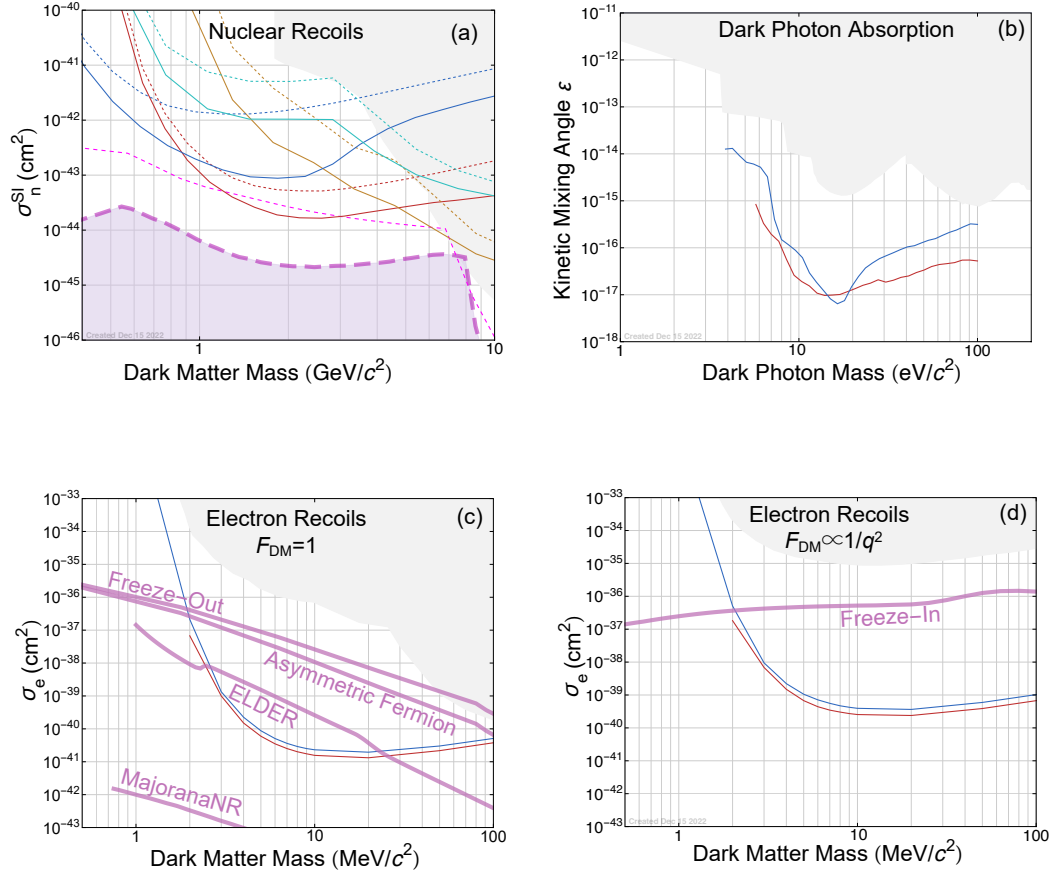


Figure 1.7: Expected sensitivity of different SuperCDMS SNOLAB detectors to various Dark Matter (DM) models using different analysis strategies: (red-brown) Ge HV, (blue) Si HV, (mustard) Germanium iZIP, (cyan) Silicon iZIP, (solid) Profile-Likelihood Ratio analysis, (dashed) Optimum Interval analysis; (gray shaded) current exclusion limits. (a) Spin-Independent DM-nucleon recoils: (magenta long dashed and shaded) neutrino fog based on Refs. [101, 102]; (magenta short dashed) “single neutrino” sensitivity, where one neutrino event can be expected on average; (b) Dark Photon absorption; (c) DM-electron recoils via heavy mediator ($F_{\text{DM}} = 1$); (magenta) theoretical predictions from various DM models; (d) DM-electron recoils via ultra-light mediator ($F_{\text{DM}} \propto 1/q^2$). Figures from Ref. [98].

Chapter 2

Cryogenic Semiconductor Detectors

As shown in the previous chapter, cryogenic semiconductor detectors are a promising DM detection technology, capable of probing lower DM masses compared to the liquid noble gas detectors. This chapter provides a brief overview of the physical principles employed in cryogenic semiconductor detectors (Section 2.1), then describes the phonon sensors used by SuperCDMS (Section 2.2), and, lastly, discusses the SuperCDMS SNOLAB detectors, as well as the detectors used to collect the data analyzed in this dissertation, the SuperCDMS High-Voltage eV-resolution (HVeV) detectors (Section 2.3).

2.1 Signals in Cryogenic Semiconductor Detectors

Particles interacting with nuclei or electrons in semiconductor crystals produce two types of signals: ionization and phonons. This section provides a short overview of the physical mechanisms behind these signals, as well as the qualitative relations between the energy deposited in an interaction and the magnitude of the expected ionization and phonon signals.

2.1.1 Ionization

In intrinsic semiconductors, such as Si and Ge, the electron energy states form two groups of allowed levels separated by a gap. The groups are called the valence band and the conduction band, while the size of the gap between them is called the band gap energy, E_{gap} . At cryogenic temperatures near 0 K, all the electrons are in the valence band, occupying all its possible energy levels, leaving no vacancies. In this configuration, electrons cannot move in the crystal, since there are no available states for them to move to. If an electron gains energy higher than the band gap, it jumps into the conduction band, where it can move spatially within the crystal. Additionally, it leaves a vacancy in the valence band. Neighboring electrons in the valence band can jump into this vacancy, moving the vacancy into a new position. Thus, the vacancy itself appears as a moving positively charged quasiparticle, referred to as

a hole. In an ideal crystal with no defects and impurities, electrons (meaning electrons in the conduction band) and holes are always created in pairs, denoted as e^-h^+ . They are also referred to as charge carriers, since they can move a charge across the crystal. If an electron in the conduction band and a hole meet in the crystal, they recombine, that is the electron moves into the hole in the valence band, thus eliminating both charge carriers. In crystalline Si and Ge, recombination is normally accompanied by an emission of phonons — collective lattice excitations.

To understand the detector response to particle interactions, it is important to derive the relation between the deposited energy E_{dep} and the number of e^-h^+ pairs created in the interaction. This relation is different for the cases in which an incoming particle interacts with a nucleus or with an electron. Let's first consider an electron interaction, in which some energy $E_{\text{dep}} \geq E_{\text{gap}}$ is deposited into an electron via a scattering or an absorption process, creating an e^-h^+ pair. The energy of the initial e^-h^+ pair is then redistributed to either creating more e^-h^+ pairs and/or to emitting phonons. Due to the loss of energy spent on the phonon emission, the energy required to produce one e^-h^+ pair is higher than the band gap energy. It is usually denoted as ϵ_{eh} . In the simplest ionization model used, for example, in Refs. [80, 103], the number of e^-h^+ pairs produced in an event with deposited energy E_{dep} is expressed as

$$n_{\text{eh}} = 1 + \text{Floor} \left(\frac{E_{\text{dep}} - E_{\text{gap}}}{\epsilon_{\text{eh}}} \right), \quad (2.1)$$

where operator Floor means rounding to the nearest smaller integer.

Ionization is, however, a statistical process, which means that the number of produced e^-h^+ pairs is subject to statistical fluctuations. To account for this, a Monte-Carlo simulation of phonon and charge production cascades in Si was performed in Ref. [104] to derive probabilities of ionizing n_{eh} e^-h^+ pairs as functions of deposited energy. Up to the deposited energy of 50 eV, Ref. [104] provides the probability functions for three band gap energy values: 1.1692 eV, 1.1627 eV and 1.1230 eV. We interpolate these functions to derive probabilities corresponding to the band gap energy value used in our analyses, 1.131 eV [105]. Figure 2.1 shows the resulting probability functions for the range of energies between E_{gap} and 25 eV.

Above 50 eV, the model in Ref. [104] provides the following functional form for probabilities to produce n_{eh} e^-h^+ pairs:

$$p_{\text{eh}}(n_{\text{eh}} | E_{\text{dep}}) = \frac{1}{\sqrt{2\pi n_{\text{eh}} F_\infty}} \exp \left[-\frac{1}{2} \left(\frac{n_{\text{eh}} \epsilon_{\text{eh},\infty} - E_{\text{dep}}}{\sqrt{n_{\text{eh}} F_\infty \epsilon_{\text{eh},\infty}}} \right)^2 \right], \quad (2.2)$$

with the asymptotic values of the mean energy per e^-h^+ pair $\epsilon_{\text{eh},\infty}$ and the Fano factor F_∞ given by:

$$\epsilon_{\text{eh},\infty} = 1.6989 E_{\text{gap}} + 0.0843 A + 1.2972, \quad (2.3)$$

$$F_\infty = -0.0281 E_{\text{gap}} + 0.0015 A + 0.1383, \quad (2.4)$$

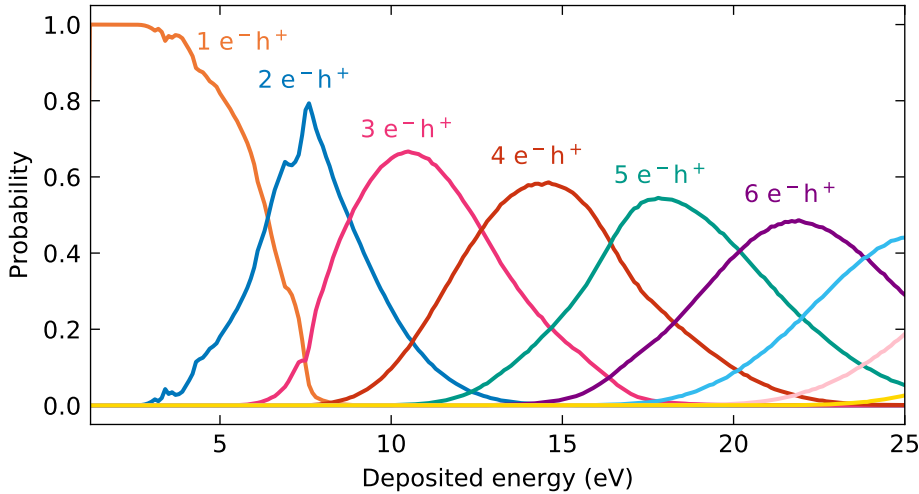


Figure 2.1: Probabilities to produce a specified number of e^-h^+ pairs in Silicon as functions of energy transferred to an electron calculated with the model described in Ref. [104], assuming the band gap energy $E_{\text{gap}} = 1.131 \text{ eV}$. E_{gap} is the lowest energy shown on the x-axis. At energies below E_{gap} , the probability to produce an e^-h^+ pair is equal zero.

where A denotes the ratio of charge-phonon to charge-charge scattering and is taken to be 5.2 eV^2 [106]. Note that Equations 2.3 and 2.4 are given here with more significant figures compared to Ref. [104]. The more precise values are obtained directly from the authors of Ref. [104] and needed to better match the probability functions below 50 eV with the functions provided by Equation 2.2 [107].

In a search for DM-electron interactions described in Chapter 5, we use the interpolated ionization probability functions described in this section, as well as Equations 2.2–2.4 at energies above 50 eV.

The case of ionization in nuclear recoils is in general out of the scope of this dissertation. For completeness, we provide a reference to the recent experimental measurement of the ionization yield in Si in nuclear recoils with energies down to 100 eV, see Ref. [108]. At energies above $\sim 15 \text{ keV}$, Lindhard theory is normally used [109].

2.1.2 Phonons

Phonons are quasiparticles that describe collective excitations of the crystal lattice. At cryogenic temperatures of the order of 10 mK, the energy of phonons in thermal equilibrium, called “thermal” phonons, is very low, of the order of $1 \mu\text{eV}$ [110]. Particle interactions in the crystal create athermal phonons of much larger energies, making them an excellent low-noise proxy for the interaction energy. We consider three main categories of phonons.

First category is the *prompt phonons*. They are created as a direct response of the lattice to a particle scattering off a nucleus. In addition, if a fraction of the deposited energy is

transferred to an electron, it moves into the conduction band and quickly loses its excess of energy via lattice scattering or by creating more $e^- h^+$ pairs, until it occupies the lowest energy level in the conduction band. The phonons created in this process are also considered prompt. As a result, the only deposited energy that is not immediately converted into prompt phonons, is the energy spent to promote electrons to the conduction band. The total energy of prompt phonons is then given by:

$$E_{\text{prompt}} = E_{\text{dep}} - n_{\text{eh}} E_{\text{gap}}, \quad (2.5)$$

where E_{dep} is the energy deposited by the incoming particle, n_{eh} is the number of created $e^- h^+$ pairs, and E_{gap} is the band gap energy of the crystal [111].

The other two phonon production mechanisms we consider are related to the charge carriers created in the ionization process and to the way they move in the crystal. We need to consider two separate scenarios: a detector without a voltage applied across the crystal and a detector with a voltage bias that creates an electric field in the crystal.

If there is no voltage bias across the crystal, created $e^- h^+$ pairs first lose their excess of energy via lattice scattering and then recombine, producing *recombination phonons*. The energy of recombination phonons is then given by

$$E_{\text{recomb}} = n_{\text{eh}} E_{\text{gap}}. \quad (2.6)$$

Thus, the total phonon energy E_{ph} in the detector with no voltage bias is equal to the energy, deposited by the particle interaction:

$$E_{\text{ph}} = E_{\text{prompt}} + E_{\text{recomb}} = E_{\text{dep}}. \quad (2.7)$$

However, if there is a voltage bias across the crystal, the charge carriers of opposite sign are pulled apart by the electric field, which prevents them from recombining. The charges are accelerated by the field and scatter off the lattice, producing more phonons and converting all the energy passed to the charges from the electric field into the phonon energy. This process is known as the Neganov–Trofimov–Luke (NTL) effect [112, 113] and the phonons are referred to as *NTL phonons*. The energy of NTL phonons is given by the number of $e^- h^+$ pairs and the difference of the electric potential $\Delta\varphi$ that they travel through:

$$E_{\text{NTL}} = n_{\text{eh}} e \Delta\varphi, \quad (2.8)$$

where e is the elementary charge. Normally, charges travel through the entire bulk of the crystal, each reaching the corresponding electrode that creates the voltage bias. In that case the NTL energy is given by

$$E_{\text{NTL}} = n_{\text{eh}} e V_{\text{bias}}, \quad (2.9)$$

where V_{bias} is the bias voltage. However, charge carriers can get trapped on impurity states, preventing them from reaching the electrode. Additionally, unpaired charge carriers can be knocked out of the impurity states in the bulk of the crystal. These processes are called Charge Trapping (CT) and Impact Ionization (II), respectively. Charges undergoing or created in these processes traverse only a part of the potential difference of the crystal, resulting in NTL phonon energies different from an integer number of eV_{bias} . We model these effects in Chapter 3 and derive the Probability Density Functions (PDFs) of the NTL energy for various scenarios.

Once charges reach the electrodes on the crystal surfaces, they release their energy into the lattice, producing recombination phonons. Neglecting the CT and II effects, the total phonon energy in a detector with a voltage bias is given by

$$E_{\text{ph}} = E_{\text{prompt}} + E_{\text{recomb}} + E_{\text{NTL}} = E_{\text{dep}} + n_{\text{eh}} e V_{\text{bias}}. \quad (2.10)$$

Figure 2.2 shows schematically all three described types of phonons in a voltage-biased crystal. The energy of phonons shown in red is equal to the deposited energy E_{dep} , while the NTL phonons shown in blue produce additional energy, greatly amplifying the deposited energy. With a strong voltage bias such that $eV_{\text{bias}} \gg E_{\text{dep}}$, the spectrum of the total phonon energy has distinct quantized peaks, corresponding to the integer numbers of created $e^- h^+$ pairs. This allows to measure ionization signal, without directly measuring the charge collected by electrodes.

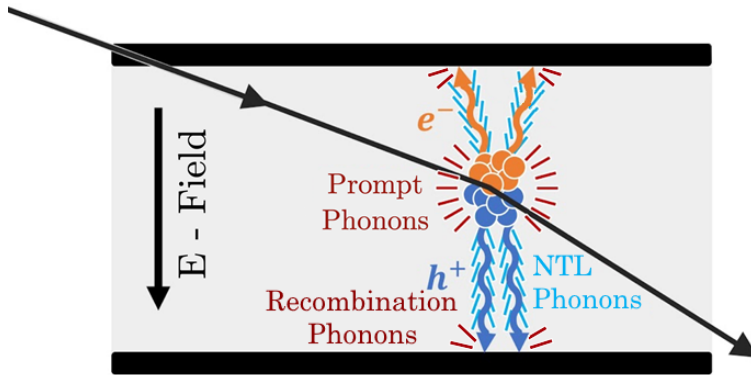


Figure 2.2: Illustration of a particle scattering off a nucleus in a semiconductor crystal with an applied voltage bias (shown as an electric field E). Two created $e^- h^+$ pairs are shown, together with prompt, recombination and NTL phonons. Adapted from Ref. [114].

Initially, phonons are produced with energies of the order of 1–10 meV or larger, with a very short mean free path. As they undergo *anharmonic down-conversion* and *isotope scattering* processes with the rates proportional to E^5 and E^4 , respectively (see Ref. [115]), they decay into phonons of lower energies, until their mean free path becomes comparable

with the size of the crystal. Phonons with energies of a few hundred μeV propagate in the crystal ballistically, that is almost with no interactions, reflecting off the crystal surfaces [111, 116]. If the crystal is instrumented with phonon sensors with a good surface coverage, the phonons are absorbed by the sensors before thermalizing. In general, only a fraction of the total phonon energy gets converted into a readout signal. This fraction is referred to as the detector energy efficiency. It largely depends on the quality of the sensors, the size of the crystal surface area covered by them, and the efficiency of the phonon absorption when they hit the sensors. We discuss the phonon sensors used in the SuperCDMS detectors in the next section.

2.2 SuperCDMS Phonon Sensors: QETs

Sensors used in SuperCDMS detectors to collect phonons and translate their energy into a measurable current are called Quasiparticle-trap-assisted Electrothermal-feedback Transition-edge sensors (QETs) [117]. We describe their principle of operation by explaining each part of this rather complicated acronym, starting from the end.

2.2.1 Transition-Edge Sensor

A Transition-Edge Sensor (TES) is a film of metal (in the case of SuperCDMS, tungsten W) held in its superconducting phase transition. The temperature at which a material becomes superconducting is known as its critical temperature, T_c . However, the transition between the normal mode with some resistance R_n and the superconducting mode with zero resistance is not immediate: there is a finite temperature interval ΔT_c in which the resistance almost linearly drops from R_n to 0, as shown in Figure 2.3. Within this interval, small changes in temperature of the order of μK cause measurable sharp changes in resistance of the order of $\text{m}\Omega$ [118].

2.2.2 Electrothermal Feedback

To hold the TES in the transition, it is first cooled down below its critical temperature T_c and then voltage biased with a current source and a shunt resistor R_{sh} connected in parallel. The shunt resistor and the current are chosen such that the resulting voltage across the TES provides exactly enough resistive heating to keep the temperature of the TES in the transition region. The heating power P is inversely proportional to the temperature-dependent TES resistance $R_{\text{TES}}(T_{\text{TES}})$:

$$P = \frac{V_{\text{bias}}^2}{R_{\text{TES}}(T_{\text{TES}})}, \quad (2.11)$$

where V_{bias} is the voltage across the TES, and T_{TES} is its temperature. At the same time, the thermal power loss through the coupling between the TES and a thermal bath (for example,

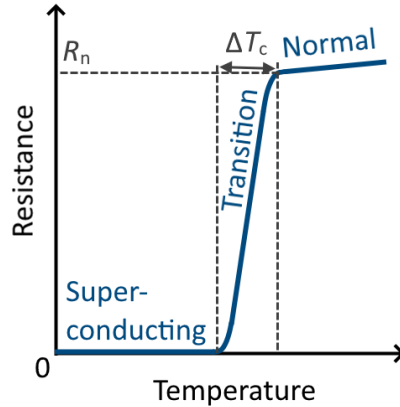


Figure 2.3: Illustration of a resistance temperature dependence of a Transition-Edge Sensor (TES) in three modes: superconducting, normal and in transition. ΔT_c denotes the transition width. R_n shows the lowest resistance in the normal mode. The steep linear dependence in transition allows TES to register small temperature variations by measuring variations in resistance.

the crystal on which the TES is located) is given by

$$P = K(T_{\text{TES}}^5 - T_{\text{bath}}^5), \quad (2.12)$$

where T_{bath} is the temperature of the thermal bath and K is the thermal conductivity between the TES and the bath [118]. In equilibrium, these two processes cancel each other out, defining the equilibrium TES temperature T_0 and the equilibrium TES resistance $R_0 = R_{\text{TES}}(T_0)$. Together they are sometimes referred to as the TES working point.

When the TES receives additional heat Q (normally, from phonons produced in the crystal), its temperature rises above the equilibrium temperature T_0 , causing a sharp rise of the resistance. As a result, the current flowing through the TES decreases, breaking the equilibrium between Equations 2.11 and 2.12. Being out of equilibrium, the thermal power loss through the coupling to the bath quickly drives the TES temperature and thus the TES current back to their equilibrium values. This process is referred to as the *electrothermal feedback*.

The current flowing through the TES is measured with a Superconducting Quantum Interference Device (SQUID) readout (see Ref. [114] for more detail). Figure 2.4 shows a simplified TES-SQUID circuit, in which the current in the TES branch is inductively coupled to a SQUID. Heat depositions in the TES are seen as negative pulses in the measured current, with their integral proportional to the amount of heat. When the TES temperature stays in the linear part of the transition curve, the shape of the pulse is defined by the electrothermal feedback. However, when the amount of deposited heat is large enough to drive the TES out of the transition mode, it goes into the normal mode, where the temperature dependence of

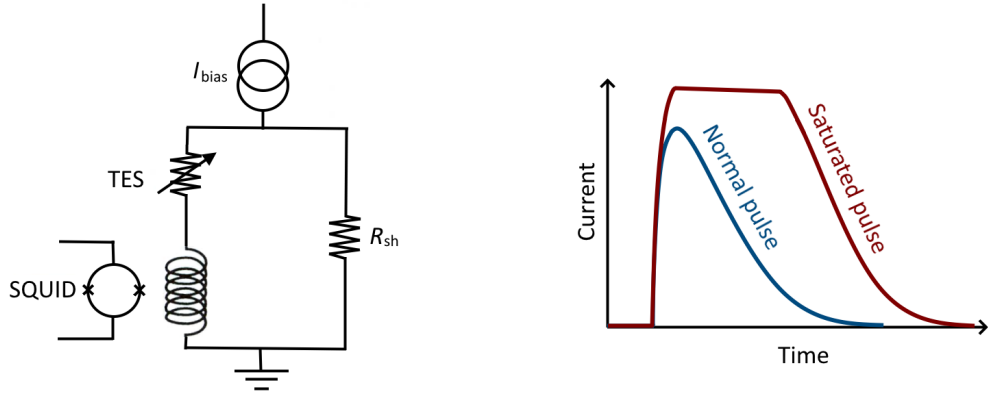


Figure 2.4: Simplified Transition-Edge Sensor (TES) bias circuit with a Superconducting Quantum Interference Device (SQUID) readout. The TES and a shunt resistor R_{sh} are connected to a source of bias current I_{bias} . The SQUID is coupled to the TES via an inductance element. Adapted from Ref. [117].

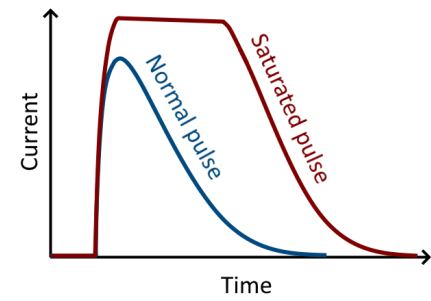


Figure 2.5: Illustration of a normal and a saturated pulse in the Transition-Edge Sensor (TES). The pulse saturation is caused by the TES temperature rising above the superconducting transition, abruptly changing the resistance-temperature dependence.

the resistance is less pronounced. As a result, large energy pulses appear saturated, as shown in Figure 2.5. Note that although the pulses in the TES current are negative, throughout this dissertation we show them as positive pulses for convenience.

2.2.3 Quasiparticle Traps

To efficiently collect athermal phonons from the crystal, the W TESs are coupled with superconducting aluminum (Al) fins with large surface areas, as shown in Figure 2.6. Athermal phonons with energies above the Al superconducting gap energy ($\sim 350 \mu\text{eV}$ [110]) break Cooper pairs [119] in the Al, creating free Bogoliubov quasiparticles [120]. The quasiparticles diffuse in the Al fins and eventually get trapped on the interface between W and Al which has lower energy levels compared to the energy levels in Al. The interface acts as a *quasiparticle trap*, which converts the energy of quasiparticles into phonons, heating up the TES.

QET sensors are used in all SuperCDMS detectors discussed in the next section.

2.3 SuperCDMS Detectors

As mentioned in Section 1.4, two types of detectors will be used in the SuperCDMS SNOLAB experiment, HV and iZIP, each having Si and Ge variants. More specifically, there will be

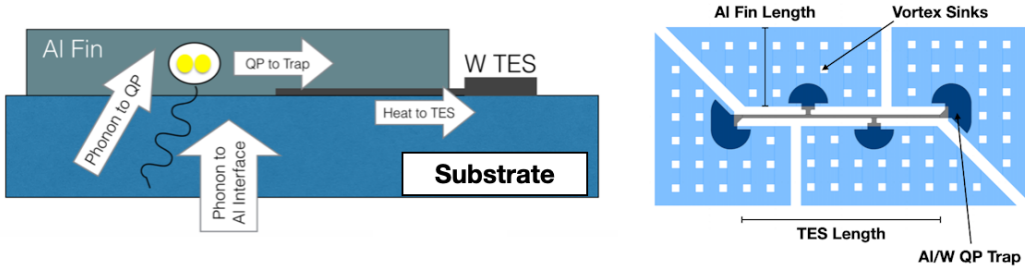


Figure 2.6: (Left) Illustration of the energy transport in a Quasiparticle-trap-assisted Electrothermal-feedback Transition-edge sensor (QET). Phonons from the Silicon substrate are absorbed by the Aluminum (Al) fin, breaking Cooper pairs and creating quasiparticles (QP). QPs trap on the Al-Tungsten (W) interface, depositing heat into the W Transition-Edge Sensor (TES). (Right) Design geometry of a QET. W TES is shown in gray. Al fins are shown in light blue. AI/W QP traps are shown in dark blue. The vortex sinks are holes in the Al fins to prevent magnetic vortices. Figure from Ref. [110].

2 Si iZIP, 10 Ge iZIP, 4 Si HV and 8 Ge HV detectors. We describe their configurations and main parameters in Sections 2.3.1 and 2.3.2.

In addition to the iZIP and HV detectors, new types of detectors based on the same operational principles have been developed in various SuperCDMS R&D programs. One class of the SuperCDMS R&D detectors is known as the HVeV detectors. They are introduced in Section 2.3.3. The data collected by the HVeV detectors in two different runs are the main focus of this dissertation.

2.3.1 iZIP Detectors

The iZIP detectors are high purity Ge (Si) crystals in the shape of a cylinder, 33.3 mm tall and 100 mm in diameter, with a mass of 1.39 (0.61) kg [121]. They are instrumented with QET phonon sensors, arranged into 12 readout channels, 6 on each face of the crystal, interleaved with electrodes used for measuring ionization signals. Low voltage biases, $\pm 3\text{ V}$ for Ge and $\pm 4\text{ V}$ for Si variants, are applied to the top and bottom electrodes, creating a vertical electric field in the crystal bulk and a transverse field near the crystal faces between the electrodes and the grounded phonon sensors. Such a configuration of the electric field allows for the discrimination between surface and bulk events, or fiducialization, as the surface events produce asymmetric signals in the top and bottom electrodes. Moreover, simultaneous measurement of the phonon and ionization signals allows for a discrimination between electron and nuclear recoils, as they have a different phonon-to-ionization signal ratio. As a result, the iZIP detectors are expected to operate in a nearly background free regime when searching for bulk nuclear recoils. The expected phonon resolution is 33 (19) eV in the Ge (Si) variants, while the expected resolution of the ionization signal is 160 (180) eV [98]. Figure 2.7 (left) shows a photograph and the phonon channel layout of the iZIP detector.

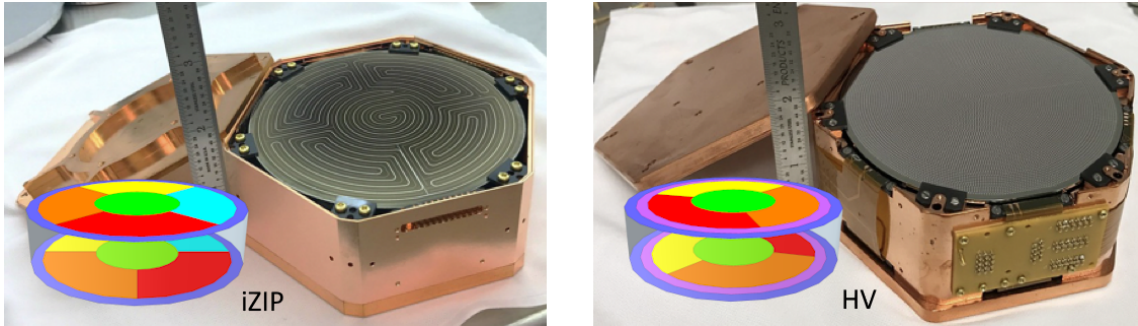


Figure 2.7: Prototypes of the SuperCDMS detectors: interleaved Z-sensitive Ionization and Phonon (iZIP) detector (left) and High-Voltage (HV) detector (right). Diagrams show the layouts of the phonon channels.

2.3.2 HV Detectors

The HV detectors are made from Si and Ge crystals, identical to those used for the iZIP detectors with the same dimensions. They differ, however, by the sensors attached to the crystals. The HV detectors are instrumented with phonon sensors only, but with better surface coverage that provides better phonon collection efficiency, compared to the iZIP detectors. A high voltage bias up to 100 V is applied between the crystal faces, creating a strong uniform electric field in the entire detector. This allows to take advantage of the NTL amplification, described in Section 2.1.2. As the NTL phonon signal is proportional to the applied bias, it boosts low energy electron recoils above the detector energy threshold. This makes HV detectors especially well suited for electron-coupled DM searches. High phonon sensor coverage provides a better position reconstruction which is used to reject events close to the sidewalls of the crystal. The expected phonon resolution of the HV detectors is 34 (13) eV in the Ge (Si) variants [98], which makes them also competitive in nuclear recoil searches. Figure 2.7 (right) shows a photograph and the phonon channel layout of the HV detector.

2.3.3 HVeV Detectors

The SuperCDMS R&D HVeV detectors were developed based on the HV detectors with the goal of improving their resolution to such a level that allows registering a single ionized charge in the crystal with the help of NTL amplification. HVeV detectors are made of high purity Si crystals with the dimensions of $10 \times 10 \times 4 \text{ mm}^3$ and a mass of 0.93 g. One of the two square faces of the crystal is lithographically patterned with phonon sensors, QETs, arranged into two readout channels — an inner channel and an outer channel (see Figure 2.8, right). The opposite face of the crystal is patterned with an aluminum grid. While the QETs are held at the ground potential, the aluminum grid on the opposite face can be biased with high voltage of the order of 100 V, creating a uniform electric field across the crystal. The crystal

is clamped between two Printed Circuit Boards (PCBs) which provide electrical connections and a heat sink (see Figure 2.8, left).



Figure 2.8: (Left) High-Voltage eV-resolution (HVeV) detector clamped between two Printed Circuit Boards. (Right) Top surface of the HVeV detector, instrumented with arrays of phonon sensors arranged into two readout channel.

The first version of the HVeV detector achieved an energy resolution of ~ 14 eV [122]. This allowed it to reach previously unexplored DM-electron interactions down to the band gap energy of Si with less than a day of exposure in a surface run without shielding (HVeV Run 1 [83]).

The second generation of HVeV detectors has a vastly improved energy resolution. It was achieved as a result of two modifications made to the HVeV design. First, the detector used in the HVeV Run 1 had a 40 nm amorphous Si layer between the crystal and the QETs. It was believed that such a layer should have reduced the probability of charges leaking into the crystal from the bias electrodes. However, tests showed that the amount of leakage does not significantly increase when the QETs are printed directly on the crystal surface. Therefore, the amorphous Si layer is not present in the second generation of HVeV detectors. The second modification is a change of the area covered by the QETs. In the first generation of HVeV detectors, the QETs covered only 13% of the crystal top surface. In the second generation, various other QET configurations are used. These configurations are referred to as the QET masks. The mask used in the HVeV Run 2 is called the NFC mask. It has a 50% surface coverage. This change, combined with the removal of the amorphous Si layer, has resulted in an improvement of the energy efficiency from 5% measured with the HVeV Run 1 detector to 27% measured with an HVeV NFC detector [110]. The improved energy efficiency has a direct impact on the resolution. HVeV NFC detector achieved a resolution of (2.65 ± 0.02) eV [110] — an improvement by a factor of 5, compared to the HVeV Run 1.

The HVeV NFC detector was operated during another surface run, HVeV Run 2, in two modes: with a voltage bias and without it. The data with the voltage applied is referred to as the High-Voltage (HV) data (not to be confused with the HV detectors), while the data acquired without the bias across the crystal is referred to as Zero-Volt (0V) data. The HV data were analyzed and used for probing DM-electron interactions in Ref. [84]. The 0V data are analyzed in Chapter 4 of this dissertation with the goal of probing DM-nucleon recoils.

In HVeV Run 3, in addition to another HVeV NFC detector, detectors with different QET masks were used, namely the NFH and NFF masks (although the detector with the NFF mask was not operational due to a fault in the mask). Furthermore, a copy of the HVeV Run 1 detector (referred to as HVeV R1) was used as the fourth detector. Figure 2.9 shows the QET masks of these detectors, with the NFC mask having the highest surface coverage. These four detectors were operated simultaneously in the same housing in an underground run at the Northwestern Experimental Underground Site (NEXUS) at Fermilab, with a \sim 100 m of rock overburden. In Chapter 5, we derive exclusion limits on the electron-coupled DM parameter space using the HV data from this run.

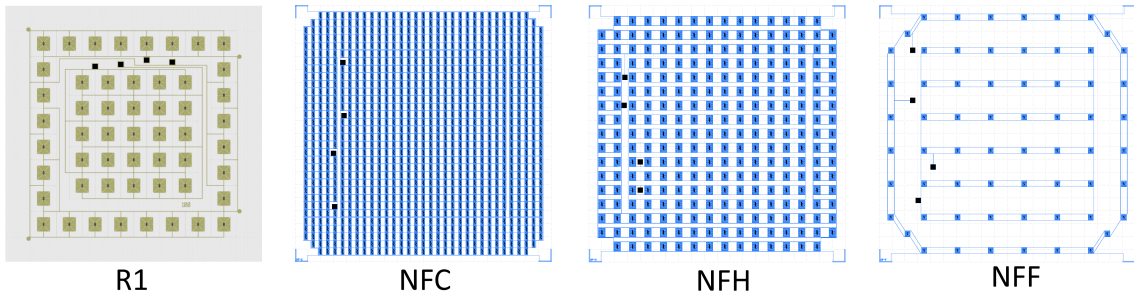


Figure 2.9: Masks of the Quasiparticle-trap-assisted Electrothermal-feedback Transition-edge sensors (QETs), used in the HVeV Run 3 detectors. From left to right, the masks are known as R1, NFC, NFH and NFF. Each blue rectangle (olive for the case of R1) is a QET. The QETs are arranged into two readout channel in each of the masks. Four black squares on each of the masks show contacts for the readout wire bonding.

Chapter 3

Charge Trapping and Impact Ionization Model

When a charge carrier moves through the crystal, it can interact with impurity states, getting trapped on unoccupied impurity energy levels, or liberating additional loosely bound charge carriers from them. These effects are called Charge Trapping and Impact Ionization (CTII). As described in Section 2.1.2, in a voltage biased detector, charge carriers generate NTL energy proportional to the distance traveled along the electric field. Without the CTII effects, independent of where an e^-h^+ pair is created, the combined distance traveled by the two charges is equal to the detector thickness. In this case, the NTL energy produced by each e^-h^+ pair is the same. The Charge Trapping (CT) effect, however, prevents some charges from reaching detector surfaces, shortening their traveled distances. In addition, the Impact Ionization (II) effects create unpaired charge carriers that travel from where their initial location to the detector surface. As a result, trapped and impact-ionized charges produce a different amount of NTL energy, compared to normal e^-h^+ pairs. Therefore, modeling the CTII effects is necessary for correctly predicting the amount of NTL energy produced in the detector.

We begin the main part of this dissertation with a description of an analytical model of CTII effects that we developed in order to improve the detector response modeling (Section 3.1). The CTII model introduced in Ref. [123] and used in the first HVeV analyses [83, 84] describes the distributions of the NTL energy produced by trapped charges or charges created in the II processes with Heaviside step functions, which is a significant simplification. Such a description suffers from a number of limitations:

- it does not accurately model the shape of the energy spectrum between the quantized peaks;
- it ignores the combinatorial effect of having two charges in the case of bulk events;
- it neglects high-order effects, such as creation of more than one charge in consecutive

II processes or consecutive II and CT processes occurring with the same charge;

- and it does not allow for different CTII probabilities for holes and electrons.

To overcome these limitations, we develop an improved CTII model based on the characteristic lengths of the CTII processes. We show that although the simplified model from Ref. [123] describes the detector response to surface events relatively well, it is not sufficient for modeling the response to events occurring in the bulk. Therefore, we use the improved model in the analysis described in Chapter 5.

3.1 Exponential CTII model

The underlying physical assumption of the model is that there are three possible processes that can occur to a charge carrier (an electron or a hole) when it traverses the bulk of the crystal under the influence of an electric field. It can get trapped on an impurity state, it can create a free electron by promoting it from an impurity state into the conduction band, or it can promote an electron from the valence band to an impurity level, creating a free hole. The probabilities to participate in these processes may be different for holes and electrons; therefore, in total we consider six different CTII processes: electron trapping (CTe), hole trapping (CTh), creation of a hole by an electron (Ileh), creation of an electron by an electron (Ilee), creation of an electron by a hole (Ilhe) and creation of a hole by a hole (Ilhh).

The model assumes that each of the six CTII processes has a small constant probability of occurring at any point of the charge's trajectory, independent of the location in the bulk of the crystal, of the path already traveled by the charge, and of other charges simultaneously traversing the crystal. Under these assumptions, the PDF of the distance z traveled by a charge along the electric field lines before a particular process occurs is described by an exponential distribution:

$$P_i(z) = \frac{1}{\tau_i} e^{-z/\tau_i}, \quad (3.1)$$

where i denotes the type of the process (CTe, CTh, Ilee, Ilhe, Ilhe or Ilhh) and τ_i is the characteristic length of this process. The electric field is assumed to be uniform, with the field lines parallel to the axis z . Equation 3.1, repeated for each of the six processes, each with its own characteristic length, together with the condition that the charges terminate when reaching the crystal surface, are the fundamental building blocks of our bulk CTII model. Due to the shape of the underlying distributions, sometimes we refer to this model as the “exponential CTII model”.

The end product of the model is a PDF of the NTL energy, produced in an event. This energy is proportional to the distance traveled by the charges along the field lines. We adopt the following units: a unit of distance is equal to the thickness of the crystal along the electric field, while a unit of energy corresponds to the NTL energy produced by a charge

traversing this thickness. In these units, $z = 0$ and $z = 1$ correspond to the opposite faces of the crystal, and a charge going from $z = 0$ to $z = 1$ produces NTL phonons with the total energy $E = 1$. We denote these units of energy as “neh”, as they show the number of fully NTL-amplified $e^- h^+$ pairs. With such units, there is a one-to-one correspondence between the PDFs of the total NTL energy and the total distance traveled by the charges along the electric field.

The six characteristic lengths τ_i are the only fundamental input parameters of the model. However, for convenience, we often define the characteristic lengths via probabilities for each of the six processes to occur to a charge if it traverses the entire thickness of the crystal. These probabilities are related to the characteristic lengths as:

$$p_i = \int_0^1 P_i(x) dx = 1 - e^{-1/\tau_i}, \quad (3.2)$$

where i is the type of the CTII process (CTe, CTh, Ilee, Ileh, IIhe, or IIhh).

We consider three types of events: surface events, in which charges are produced on the crystal face; bulk events, in which $e^- h^+$ pairs are produced in the bulk at a uniformly distributed depth z_0 ; and one-charge bulk leakage events, in which only one charge is produced in the bulk due to a particle interacting with an impurity or due to a spontaneous leakage of charge from an impurity state. The resulting PDFs of the NTL energy are different for each of these types of events due to the different possible combination of occurring CTII processes.

3.1.1 CTII Effects in Surface Events

We start with surface events, in which one charge carrier is created at one of the crystal faces and pulled towards the opposite face by the electric field. For concreteness, let us assume that the initial charge is an electron. Solutions for the case of a hole as an initial charge are found by mutually substituting all the e and h indices in all the following equations. To find the PDF of NTL energy we consider various possible combinations of CTII processes that may occur to an initial electron. In the most simple scenario, no CTII processes happen and the electron successfully reaches the opposite face of the crystal, creating NTL phonons with energy $E = 1$. The probability of this scenario to occur is the multiplication of probabilities of all three possible electron CTII processes not occurring at distances $z < 1$:

$$\rho_{\text{surf},0} = \bar{C}_{\text{CTe}}(1) \bar{C}_{\text{Ilee}}(1) \bar{C}_{\text{Ileh}}(1) = e^{-1/\tau_{\text{CTe}}} e^{-1/\tau_{\text{Ilee}}} e^{-1/\tau_{\text{Ileh}}} = e^{-T_e}. \quad (3.3)$$

Here we used the complementary Cumulative Distribution Functions (CDFs) of the CTII processes,

$$\bar{C}_i = 1 - C_i, \quad (3.4)$$

with the CDFs obtained by integrating Equation 3.1:

$$C_i(z) = \left(1 - e^{-z/\tau_i}\right). \quad (3.5)$$

In addition, we introduce the following notation for convenience:

$$T_e \equiv \frac{1}{\tau_{CTe}} + \frac{1}{\tau_{Ilee}} + \frac{1}{\tau_{Ileh}}. \quad (3.6)$$

The part of the resulting NTL energy PDF corresponding to the scenario of no CTII processing occurring is then a delta function at $E = 1$ with an amplitude equal to the derived probability:

$$F_{\text{surf},0}(E) = \delta(E - 1) e^{-T_e}. \quad (3.7)$$

The next possible scenario is that the electron gets trapped after traversing the distance z , without creating additional charges via II processes. Again, we need to use the complementary CDFs to take into account the probability of II processes not happening at the distance z . The PDF of the total distance traveled by the charge reduced by the probability of no II processes occurring is then given by

$$p_{\text{surf},1}(z) = \frac{1}{\tau_{CTe}} e^{-z/\tau_{CTe}} \bar{C}_{Ilee}(z) \bar{C}_{Ileh}(z) = \frac{1}{\tau_{CTe}} e^{-zT_e}. \quad (3.8)$$

Using the equivalence between the travelled distance and the NTL energy and applying the termination condition at $z = 1$, we get another part of the NTL energy PDF:

$$F_{\text{surf},1}(E) = \begin{cases} \frac{1}{\tau_{CTe}} e^{-ET_e} & 0 \leq E < 1 \\ 0 & \text{else.} \end{cases} \quad (3.9)$$

The II processes require more care, as the charges to which such processes occur do not terminate and may or may not participate in more CTII processes afterwards. Let us consider a scenario in which an electron creates a hole after traveling a distance z , with no other CTII processes occurring to the initial electron and to the created hole. The probability of this scenario to be realized includes the probabilities of CTe and Ilee processes not occurring in the entire bulk of the detector, Ileh occurring once at the location z and not occurring afterwards at the remaining distance $1 - z$, and the probabilities of any CTII processes not occurring to the created hole, while it traverses the distance z in the opposite direction. Introducing T_h analogously to T_e in Equation 3.7, we get:

$$\begin{aligned}
p_{\text{surf},2}(z) &= \bar{C}_{\text{CTe}}(1)\bar{C}_{\text{Ilee}}(1)P_{\text{Ileh}}(z)\bar{C}_{\text{Ileh}}(1-z)\bar{C}_{\text{CTh}}(z)\bar{C}_{\text{IIhe}}(z)\bar{C}_{\text{IIhh}}(z) \\
&= e^{-1/\tau_{\text{CTe}}}e^{-1/\tau_{\text{Ilee}}}\frac{1}{\tau_{\text{Ileh}}}e^{-z/\tau_{\text{Ileh}}}e^{-(1-z)/\tau_{\text{Ileh}}}e^{-z/\tau_{\text{CTh}}}e^{-z/\tau_{\text{IIhe}}}e^{-z/\tau_{\text{IIhh}}} \\
&= \frac{1}{\tau_{\text{Ileh}}}e^{-T_e - zT_h}.
\end{aligned} \tag{3.10}$$

To make a transition to the PDF of produced NTL energy, we derive the relation between the energy E and the variable z from the geometry of the process. In this particular case, an electron travels the entire bulk of the crystal, whereas the hole traverses the distance z in the opposite direction, so the relation is $E = 1 + z$, with z limited to the interval between 0 and 1. The energy PDF part corresponding to this scenario is then given by

$$F_{\text{surf},2}(E) = \begin{cases} \frac{1}{\tau_{\text{Ileh}}}e^{T_h - T_e - ET_h} & 1 \leq E < 2 \\ 0 & \text{else.} \end{cases} \tag{3.11}$$

We derive analytical solutions for other possible combinations of CTII processes in the same manner. The II processes pose a challenge, as the number of charges, and therefore the number of process combinations and the complexity of the solutions grow exponentially with the number of allowed II processes. For this reason, we limit the order of the II processes to 2 for the surface events, which means that a charge participated or produced in an II process can take part in no more than one additional II process. Charges that reached the maximum allowed order of II processes are propagated to the corresponding crystal face unhindered, with no more CTII effects allowed. This simplification limits the applicability of the model to cases of low II probabilities. For the HVeV detectors, the probability of the II processes is measured to be of the order of 1% [84, 124], therefore, the probability of second-order II effects is sufficiently small, of the order of 10^{-4} .

The full catalog of the analytical solutions for the NTL energy PDF constituents $F_{\text{surf},j}(E)$, corresponding to every possible combination of CTII effects up to the second order, is provided in Ref. [125] (in preparation). In Figure 3.1 we show all these functions for $p_{\text{CTe}} = p_{\text{CTh}} = 0.12$ and $p_{\text{Ileh}} = p_{\text{Ilee}} = p_{\text{IIhh}} = p_{\text{IIhe}} = 0.01$. The sum of all the considered scenarios gives the final NTL energy PDF for surface events:

$$F_{\text{surf}}(E) = \sum_j F_{\text{surf},j}(E). \tag{3.12}$$

3.1.2 CTII Effects in Bulk Events

Turning now to the bulk events, we introduce an additional parameter z_0 , which describes the position of the events in the crystal's bulk. To find the NTL energy PDFs for such

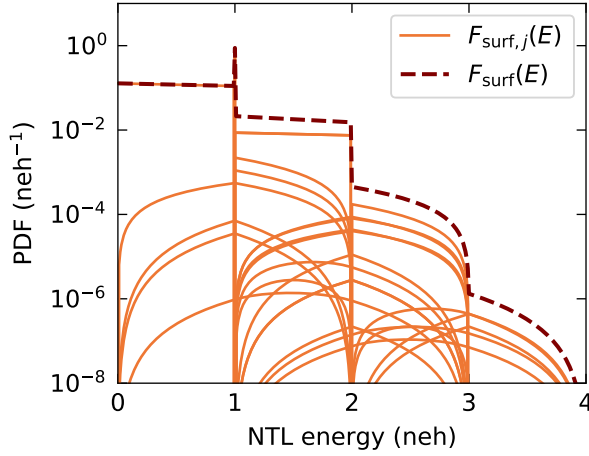


Figure 3.1: Analytical solutions for Neganov–Trofimov–Luke (NTL) energy distributions produced in single- e^-h^+ -pair surface events by charges undergoing all the possible combinations of Charge Trapping and Impact Ionization (CTII) processes up to the second order (solid lines). 1 neh energy unit corresponds to the NTL energy produced by 1 fully amplified e^-h^+ pair. The dashed line shows the total Probability Density Function of the NTL energy of produced phonons. The following CTII probabilities are considered: $p_{CTe} = p_{CTh} = 0.12$, $p_{Ilee} = p_{Ileh} = p_{Ihe} = p_{Ihh} = 0.01$.

events, we use the same technique as for surface events, with an additional integration over z_0 , assuming that the events are uniformly distributed in the bulk. For example, in a bulk event with an e^-h^+ pair produced at z_0 , the probability for the electron to be trapped at the location z and for the hole to travel to the face $z = 0$ without any CTII effects, is given by:

$$\begin{aligned} p_{\text{bulk},1}(z | z_0) &= \bar{C}_h(z_0) \bar{C}_{Ilee}(z - z_0) \bar{C}_{Ileh}(z - z_0) P_{CTe}(z - z_0) \Theta(z - z_0) \Theta(1 - z) \\ &= \frac{1}{\tau_{CTe}} e^{-T_h z_0 - T_e(z - z_0)} \Theta(z - z_0) \Theta(1 - z), \end{aligned} \quad (3.13)$$

where the Heaviside step functions Θ explicitly limit the variable z to the interval $(z_0, 1)$ and the following notation is used:

$$\bar{C}_h(z_0) \equiv \bar{C}_{CTh}(z_0) \bar{C}_{Ihe}(z_0) \bar{C}_{Ihh}(z_0). \quad (3.14)$$

With the hole traveling the distance z_0 and the electron traveling the distance $z - z_0$, the NTL energy, equal to the total distance traveled by the charges, is $E = z$. Using this trivial relation and integrating Equation 3.14 over z_0 , we get the following component of the NTL energy PDF:

$$F_{\text{bulk},1}(E) = \begin{cases} \frac{1}{\tau_{\text{CTe}}(T_e - T_h)} (e^{T_h E} - e^{T_e E}) & 0 \leq E < 1 \\ 0 & \text{else.} \end{cases} \quad (3.15)$$

We consider two types of bulk events: events in which an interaction in the crystal produces an $e^- h^+$ pair, and events in which initially only one charge is produced (bulk charge leakage). Solutions for all possible combinations of CTII processes in these types of events are produced in the same way as described in the example above. For the one-charge bulk events, processes up to the second order are considered, as in the case of surface events. In the case of $e^- h^+$ -pair bulk events, however, there are initially two charges, which makes the amount of possible combinations of processes quadratically larger. It makes it very challenging to model second-order effects, so we limit the model to the first-order effects for the case of $e^- h^+$ -pair bulk events, which means that a charge participated or produced in an II process has a 100% probability of reaching the corresponding surface. A Kolmogorov-Smirnov test shows that with 100 000 events simulated with no limitations on the CTII process order, the model limited to first-order effects starts to be rejected with a 90% confidence for II probabilities higher than 10% [126]. Therefore, we expect the first-order model to be sufficient for the HVeV detectors, in which much lower II probabilities are expected [84, 124].

Figure 3.2 shows the solutions $F_{\text{bulk},j}$ (left) and $F_{\text{bulkleak},j}$ (right) for all the considered combinations of CTII effects in bulk events producing an $e^- h^+$ pair (subscript “bulk”) or a single charge (subscript “bulkleak”). The same typical CTII probabilities as in the case of surface events are assumed. The sums of all the considered combinations define the final NTL energy PDFs for these types of events:

$$F_{\text{bulk}}(E) = \sum_j F_{\text{bulk},j}(E), \quad (3.16)$$

$$F_{\text{bulkleak}}(E) = \sum_j F_{\text{bulkleak},j}(E). \quad (3.17)$$

The full catalog of all the constituent analytical functions $F_{\text{bulk},j}(E)$ and $F_{\text{bulkleak},j}(E)$ can be found in Ref. [125] (in preparation).

3.1.3 Detector Response with Improved CTII Modeling

In events producing multiple $e^- h^+$ pairs, the total energy of the NTL phonons is equal to the sum of the energy of the NTL phonons produced by each $e^- h^+$ pair. Assuming that the charges propagate through the crystal independently from each other without affecting each other’s CTII probabilities, the PDF of the total phonon energy is given by the convolution of the PDFs of the NTL energy produced by each $e^- h^+$ pair. Put in other words, the PDF of NTL energy in an event with n $e^- h^+$ pairs is given by the PDF of NTL energy produced

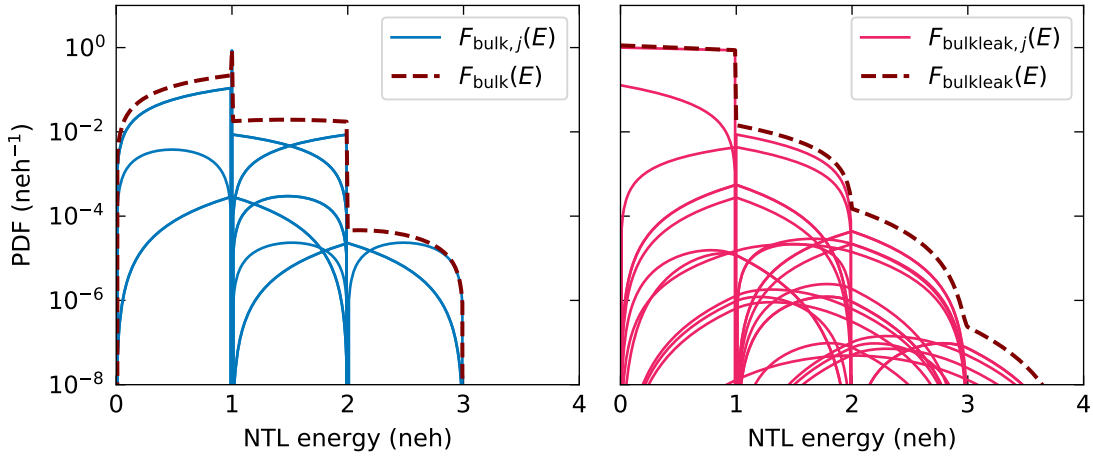


Figure 3.2: (Left) Analytical solutions for Neganov–Trofimov–Luke (NTL) energy distributions produced in single- e^-h^+ -pair bulk events by charges undergoing all the possible combinations of Charge Trapping and Impact Ionization (CTII) processes up to the first order (blue solid lines). (Right) Solutions for single-charge bulk leakage events with the combinations of CTII processes up to the second order (pink solid lines). 1 neh energy unit corresponds to the NTL energy produced by 1 fully amplified e^-h^+ pair. The dashed lines show the total Probability Density Functions (PDFs) of the NTL energy of produced phonons. The following CTII probabilities are considered: $p_{CTe} = p_{CTh} = 0.12$, $p_{Ile} = p_{Ileh} = p_{Ilh} = p_{Ilh} = 0.01$.

by one e^-h^+ pair convolved with itself $n - 1$ times. Writing it down recursively, we get:

$$F_{\text{type}}^{(n)}(E) = F_{\text{type}}^{(n-1)}(E) * F_{\text{type}}(E), \quad (3.18)$$

where the subscript “type” can be “surf”, “bulk” or “bulkleak”, depending on the type of considered events, and the energy E is in units of “neh” as defined in the beginning of Section 3.1. For completeness, let’s define $F_{\text{type}}^{(0)}(E)$ as the PDF of NTL energy produced in events with no e^-h^+ pairs. This energy is always 0, so $F_{\text{type}}^{(0)}(E) = \delta(E)$.

If a Probability Mass Function (PMF) of the expected number of e^-h^+ pairs is $p_{eh}(i)$, the PDF of the total NTL energy is given by:

$$f_{\text{NTL}}(E) = \sum_{i=0}^{\infty} p_{eh}(i) F_{\text{type}}^{(n)}(E). \quad (3.19)$$

In electron interactions, the PMF of the number of e^-h^+ pairs is given by the ionization model and is dependent on the deposited energy. Making a transition to normal units of energy (eV) and applying a detector resolution σ as a Gaussian function $G(E | \sigma)$, we get the detector response model that translates the deposited energy spectrum dR/dE_{dep} to the measured total phonon energy spectrum dR/dE :

$$\frac{dR}{dE}(E) = \sum_{i=0}^{\infty} \left(\int_0^{\infty} p_{\text{eh}}(i | E_{\text{dep}}) F_{\text{type}}^{(i)}\left(\frac{E - E_{\text{dep}}}{eV_{\text{bias}}}\right) \frac{dR}{dE_{\text{dep}}}(E_{\text{dep}}) dE_{\text{dep}} \right) * G(E | \sigma). \quad (3.20)$$

Here e is the elementary charge and V_{bias} is the bias voltage applied to the crystal. The eV_{bias} term performs the conversion from eV units to the units of “neh”. The fact that the deposited energy E_{dep} is also measured by the detector in addition to the energy of NTL phonons is taken into account in Equation 3.20 by convolving the PDF of the NTL energy $F_{\text{type}}^{(i)}(E)$ with a Dirac delta function $\delta(E - E_{\text{dep}})$. As a result, the argument of $F_{\text{type}}^{(i)}$ is the shifted energy $E - E_{\text{dep}}$, rather than just E that would be used in the case of the NTL-only energy.

3.1.4 Discussion

Due to the improved CTII modeling, the expected detector response to bulk and surface events is different. This fact has a very important implication: by studying the shapes of measured energy spectra, we should better understand the source of the backgrounds in our detectors. Moreover, the difference between the expected spectral shapes of DM events and background events can be used to an advantage in likelihood-based DM searches. We demonstrate it below on a simple but illustrative example: comparison between the expected spectral shape of DP events with mass $m_{\text{DM}} = 2 \text{ eV}/c^2$ and of surface charge leakage events, which is a significant source of background in the first e^-h^+ -pair peak.

We consider DP absorption on electrons in the bulk of the detector, with the PDF of deposited energy described by a Dirac delta function $\delta(E_{\text{dep}} - m_{\text{DM}})$. For demonstrative purposes, we are only interested in the spectral shapes rather than in the expected rates, so we use this delta function in place of dR/dE_{dep} in Equation 3.20. According to the ionization model described in Ref. [104], events with 2 eV energy always produce one e^-h^+ pair, so the term $p_{\text{eh}}(i | E_{\text{dep}})$ becomes a Kronecker delta function δ_{i1} . The case of leakage events is similar: we neglect the possibility of simultaneous leakage of multiple charges and use δ_{i1} for the PMF of produced pairs and consider the deposited energy to be 0, so $dR/dE_{\text{dep}} = \delta(E_{\text{dep}})$. The main difference is that for surface leakage events we use f_{surf} instead of f_{bulk} for the PDF of NTL energy. In both cases we assume a 100 V bias when converting units of NTL energy to eV. The assumed CTII probabilities are 12% for CT and 1% for II of any type of charge, the typical values in HVeV detectors [84].

The resulting expected spectra of DP and charge leakage events are shown in Figure 3.3 (left). Below the peak at 100 eV, corresponding to events with full NTL amplification, the shapes are strikingly different. This is different from the case of the simple CTII model, described in Ref. [123] and used in previous HVeV analyses [83, 84] (see the right plot in Figure 3.3), in which the spectra are almost indistinguishable.

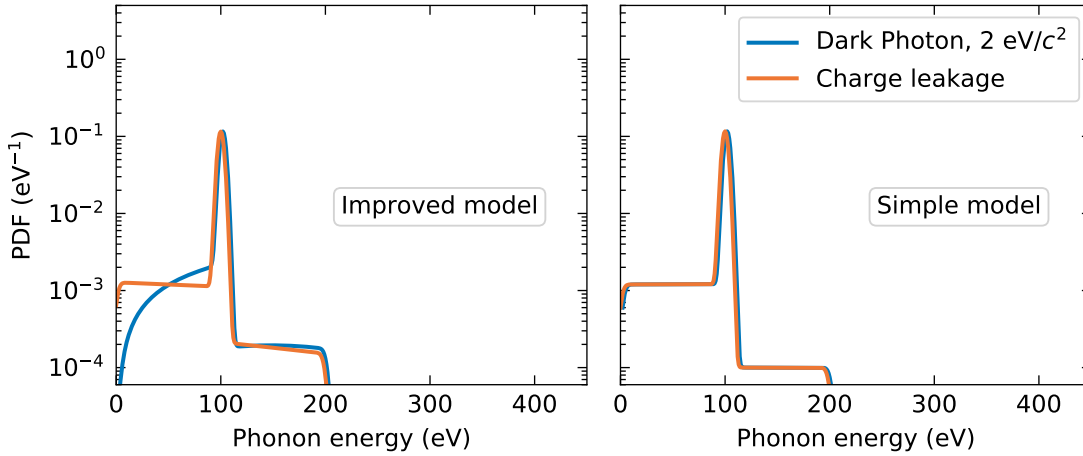


Figure 3.3: Probability Density Functions (PDFs) of the total phonon energy in Dark Photon (DP) absorption events with the DP mass $2 \text{ eV}/c^2$ (blue) and in surface charge leakage events (orange) as predicted by the improved Charge Trapping and Impact Ionization (CTII) model described in this chapter (left) and by the simple CTII model from Ref. [123] (right). The following parameters are used: Charge Trapping probability for electrons and holes is 12%, probability of Impact Ionization of every type is 1%, energy resolution is 3 eV.

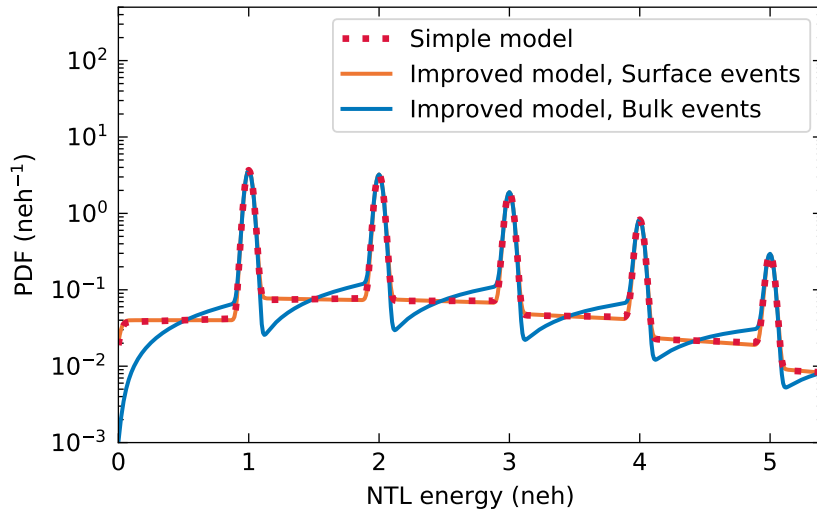


Figure 3.4: Neganov–Trofimov–Luke (NTL) energy spectra for events with an arbitrary chosen distributions of created $e^- h^+$ pairs, 12% Charge Trapping probability, 1% Impact Ionization probability of every type and 0.03 neh resolution. The spectra are produced with the simple CTII model from Ref. [123] (dashed line) and the improved model described in this chapter, considering that the events happen either on the surface (orange) or in the bulk (blue). 1 neh energy unit corresponds to the NTL energy produced by 1 fully amplified $e^- h^+$ pair.

In Figure 3.4 we consider a generalized case with some arbitrary distribution of created e^-h^+ pairs. For simplicity, we neglect the deposited energy and only show the NTL energy in units of fully amplified e^-h^+ pairs, “neh”. Spectra for surface and bulk events are shown, modeled with the improved exponential model and with the simple model from Ref. [123]. The simple model does not make a distinction between surface and bulk events; therefore, only one curve is shown that represents both the surface and the bulk events. Interestingly, the simple model gives a spectrum, very similar to the spectrum of the surface events in the improved model. This observation explains why the simple model was successfully used to fit surface calibration events in previous HVeV analyses [84, 124]. Moreover, we confirmed that fitting the simple and improved models to the calibration data (laser surface events) yields almost identical probabilities of CTII effects, so we conclude that the CTII probabilities obtained with the simple model in previous analyses are valid. In the case of bulk events, the two models predict different shapes. We do not have data with a known source of bulk events that could validate (or refute) our improved model, but since this model is better physically motivated, we use it to model DM signals in the HVeV Run 3 analysis, described in Chapter 5. This is different from the previous HVeV analyses in which the simple model was used for the DM signal modeling [83, 84].

Chapter 4

0VeV: Light Dark Matter Nuclear Recoil Search

This chapter presents the first of the two DM search analyses described in this dissertation. It utilizes the data taken with an HVeV NFC detector during HVeV Run 2 with no voltage bias applied across the crystal to set an exclusion limit on the strength of Spin-Independent (SI) DM nuclear interactions. Since the letters “HV” stand for “High Voltage” in the HVeV acronym, to highlight the fact that the data analyzed in this study were collected without the high voltage, we refer to this analysis as “0VeV”. The data are referred to as 0V data.

After a brief introduction in Section 4.1, we describe the experimental setup in Section 4.2, the data processing which including triggering and energy reconstruction in Section 4.3, the energy calibration in Section 4.4, and the data selection criteria in Section 4.5. Section 4.6 describes how the detector response effects are applied to the DM signal model. Lastly, in Section 4.7 we present the resulting exclusion limit on the SI DM-nucleon scattering cross section, and discuss this result in Section 4.8.

4.1 Introduction

As discussed in Chapter 1, LDM is a well-motivated DM candidate largely inaccessible by liquid noble gas experiments. Cryogenic semiconductor detectors with low energy threshold is a promising technology for LDM searches. HVeV detectors are designed specifically with the goal of achieving sensitivity to a single ionized charge, with the energy amplified by the NTL effect. The amplification is achieved by applying a high voltage bias across the detector. In this mode, HVeV detectors are sensitive to DM-electron interaction of energies as low as the band gap energy of the target material, Si. This allowed HVeV detectors to be used in searches for LDM with masses down to $500 \text{ keV}/c^2$ via electron recoils, as well as for DPs and ALPs with masses down to $\sim 1.2 \text{ eV}/c^2$ via electron absorption [83, 84].

Searches for DM-nucleon interactions, on the other hand, do not benefit from amplifica-

tion of ionization signal due to the small value and the large uncertainty of the nuclear recoil ionization yield. Probing low DM masses with nuclear recoils requires measuring phonon signals with a low energy threshold. A very good resolution of (2.65 ± 0.02) eV achieved by the HVeV NFC detector makes it competitive in searches for LDM-nucleon recoils when operated in the 0V mode.

During HVeV Run 2, besides the data in the HV mode analyzed in Ref. [84], 12 hours of data in the 0V mode were acquired with the HVeV NFC detector. In the analysis presented here, we take advantage of its energy resolution to set an exclusion limit on the SI DM-nucleon scattering cross section with DM masses below ~ 100 MeV/ c^2 by applying a sub-10 eV energy threshold to the 0V data.

4.2 Experimental Setup

HVeV Run 2 took place in a surface laboratory at Northwestern University, Illinois, in spring 2019. An HVeV NFC detector was clamped between two PCBs in a light-tight copper box, as shown in Figure 4.1. The copper box was enclosed in a superconducting Niobium magnetic shield and placed in an Adiabatic Demagnetization Refrigerator (ADR). The ADR was operated in daily temperature cycles, providing each day 10–12 hours of stable temperature using Ferric Ammonium Alum (FAA) and Gadolinium Gallium Garnet (GGG) paramagnetic salts. The FAA stage of the ADR was thermally coupled to the detector box, cooling it down to 48–52 mK [114, 127]. Figure 4.2 shows the setup inside the ADR, with the detector box open and without the magnetic shield.

Two calibration mechanism were implemented in the Run 2 setup: optical photons and X-rays. A laser with a wavelength of 635 nm served as a source of optical photons with the energy of 1.95 eV. An optical fiber was used to transmit photons from the laser onto the QET-instrumented face of the detector. ^{57}Co and ^{55}Fe were used as the sources of X-rays [114, 127].

The QET channels of the detector were read out with SQUIDs and digitized with an Analog-to-Digital Converter (ADC) board with a continuous 1.515 MHz sampling. No triggering was applied at the data collection stage. The entire data stream was continuously written to a hard drive for subsequent offline data processing. We refer to the sum of the currents of the two QET channels as the raw trace in this analysis. Unsummed currents from individual channels are not used at any stage of the 0VeV analysis.

For the calibration data collected with the laser, the laser was fired in pulses. The intensity of the pulses was adjusted to produce up to four $e^- h^+$ pairs in the detector per laser pulse. The so-called Transistor–Transistor Logic (TTL) signal which controls the laser was recorded and used to locate the laser pulses in the detector data stream. Detector pulses in coincidence with the pulses in the TTL signal are referred to as TTL-triggered events and are associated with the laser photons hitting the detector.

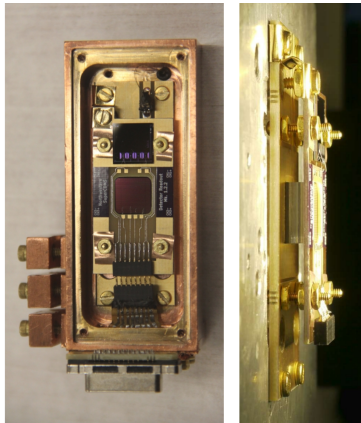


Figure 4.1: HVeV Run 2 detector setup. (Left) Copper box with the lid open with the detector clamped between two Printed Circuit Boards (PCBs) placed inside, front view. (Right) Lateral view of the detector and the PCBs.

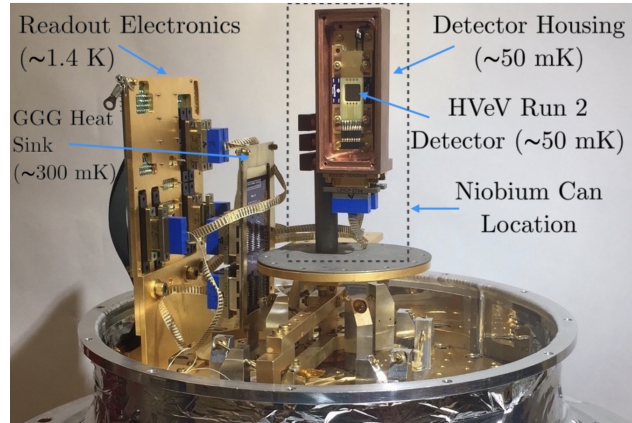


Figure 4.2: HVeV Run 2 setup inside the Adiabatic Demagnetization Refrigerator. The Gadolinium Gallium Garnet (GGG) stage provide the temperature of ~ 300 mK, while the Ferric Ammonium Alum (FAA) stage coupled to the detector cools the detector to ~ 50 mK. The detector housing is shown open. The magnetic shield and the calibration setup are not shown.

In addition to the QET and TTL signals, the ADC board recorded the temperature measured with a Resistance Temperature Detector (RTD) installed at the FAA stage of the ADR.

The main detector mode in Run 2 was the HV mode: 96 hours of data with 60 V and 100 V biases were collected during the run. These data were analyzed in Ref. [84] to set exclusion limits on the strength of DM-electron interactions. In this chapter, however, we focus on the data collected with no voltage applied across the crystal. 12 hours of such data were acquired during the run. To distinguish these data from the calibration data, we refer to it as the science data. In addition, the following calibration data were acquired: daily laser data with 60 V and 100 V biases, one day of ^{57}Co data with 60 V bias, two days of ^{57}Co data in 0V mode, and short series of ^{55}Fe data with 40 V, 50 V and 60 V biases.

4.3 Data Processing

In searches for DM via nuclear recoils, the lowest accessible DM mass is directly linked to the energy threshold of the experiment. In contrast, in searches for DM-electron interaction that benefit from the NTL amplification, the lowest accessible DM mass is defined by the band gap energy of the target material, while the the energy threshold only needs to be lower than the NTL energy produced by one $e^- h^+$ pair. Because of this, in the previous HVeV analyses that were conducted with the HV data [83, 84], the energy threshold was not optimized.

For the 0VeV analysis described in this chapter, we develop a triggering algorithm based

on the Optimum Filter (OF) in order to minimize the rate of noise triggers with the triggering threshold pushed to the lowest possible value.

4.3.1 Optimum Filter

Under the assumption of stationary noise, OF provides the best energy estimator for pulses of known constant shape [128]. The idea of the OF energy estimator is to fit a pulse template S to a signal trace V in frequency domain, with the template amplitude A being the only free parameter. The trace and the template are taken to be of the same length. Using the noise Power Spectral Density (PSD) J as the expected variance of noise frequency components, we write the χ^2 goodness of fit as

$$\chi^2 = \frac{\Delta t}{n} \sum_{k=0}^{n-1} \frac{|V_k - AS_k|^2}{J_k}, \quad (4.1)$$

where Δt is the sampling period, k is the index of the frequency component and n is the number of frequency components, equal to the length of the trace and the template. The term before the sum makes χ^2 to be independent of the sampling period and the trace length [128]. Solving the minimization problem for χ^2 , we get the best-fit amplitude:

$$A = \frac{\operatorname{Re} \left[\sum_{k=0}^{n-1} \frac{S_k^* V_k}{J_k} \right]}{\sum_{k=0}^{n-1} \frac{S_k^* S_k}{J_k}} = \frac{1}{N} \operatorname{Re} \left[\sum_{k=0}^{n-1} \Phi_k V_k \right], \quad (4.2)$$

where we defined the OF kernel in frequency domain as

$$\Phi_k = \frac{S_k^*}{J_k}, \quad (4.3)$$

and the filter normalization as

$$N = \sum_{k=0}^{n-1} \Phi_k S_k. \quad (4.4)$$

Equation 4.2 gives the fit amplitude used as the pulse energy estimator for the case where the trace has the same length as the template. To define the OF for a trace of arbitrary length, we convert Equation 4.2 into the time domain, by substituting the multiplication of frequency components by a convolution of their time-domain counterparts:

$$a = \frac{1}{N} (\phi * v), \quad (4.5)$$

where v is the trace in the time domain, ϕ is the OF kernel in the time domain produced with the inverse discrete Fourier transform of Φ , and a is the filtered trace. We perform the convolution without zero-padding of the trace, so the time samples of the filtered trace a_i are equivalent to the OF amplitudes A , calculated on the $[v_i; v_{i+n-1}]$ intervals of the trace.

This means that by filtering a raw trace v with the OF as shown in Equation 4.5, we obtain the best-fit amplitude values of the pulse template with all the possible discrete time shifts of the template with respect to the trace.

4.3.2 Triggering and Processing

Figure 4.3 illustrates the OF kernel calculation procedure used in the current analysis. In general, two components are required: the pulse template and the noise PSD.

The pulse shape in an HVeV detector is mostly defined by the QET electrothermal feedback, with the pulse rise time determined by the phonon collection time being negligibly small. Since the electrothermal feedback does not depend on the crystal bias, the pulse shapes in the 0V and HV modes are expected to be the same. This allows us to use the laser data collected in the HV mode to derive pulse template to be used for the 0V data. The pulse template is thus defined as the averaged TTL-triggered laser pulse. The length of the template defines the length of the OF kernel which needs to be balanced between preserving the low-frequency information (the longer the kernel, the better) and reducing the probability of pile-up (the shorter, the better). We tested several values of the template length ranging from 512 to 100000 time samples, and chose the value of 16384 time samples (10.8 ms) as the value which yields the lowest noise trigger rate with the highest trigger efficiency. The resulting pulse template, zoomed in on the pulse, is shown in Figure 4.3 (upper right).

The noise PSD is calculated using so-called “noise traces”. The noise traces are obtained by taking random snippets, 16384 time samples in length, from the raw trace of the 0V science data. The noise PSD is then calculated as a periodogram of the noise traces, with the noise traces containing pulses rejected as outliers in the distributions of the mean values, standard deviations, slopes and skewnesses. The noise PSD is calculated for every hour of data, to account for possible noise instability. An example of the noise PSD is shown in Figure 4.3 (upper left).

Using the pulse template and the noise PSD, the OF kernel is calculated with Equation 4.3, applying Fourier transforms where necessary. The OF kernel in time domain is shown in Figure 4.3 (upper middle). The raw traces are then filtered with the OF kernel using Equation 4.5.

After filtering raw traces with the OF, we apply a threshold trigger, with the threshold corresponding to 9.2 eV. With the energy resolution $\sigma = 2.65$ eV, measured by calculating the standard deviation of the filtered noise traces, the threshold corresponds to 3.47σ . Setting the threshold at such a low level is a trade-off: we gain sensitivity to lower recoil energies, and thus to lower DM masses, at the cost of a higher rate of noise triggers.

After each upward crossing of the filtered trace and the threshold, a window of 8192 time samples is defined, in which the point where the filtered trace reaches its maximum is found and called the trigger point. The value of the filtered trace at this point corresponds to the

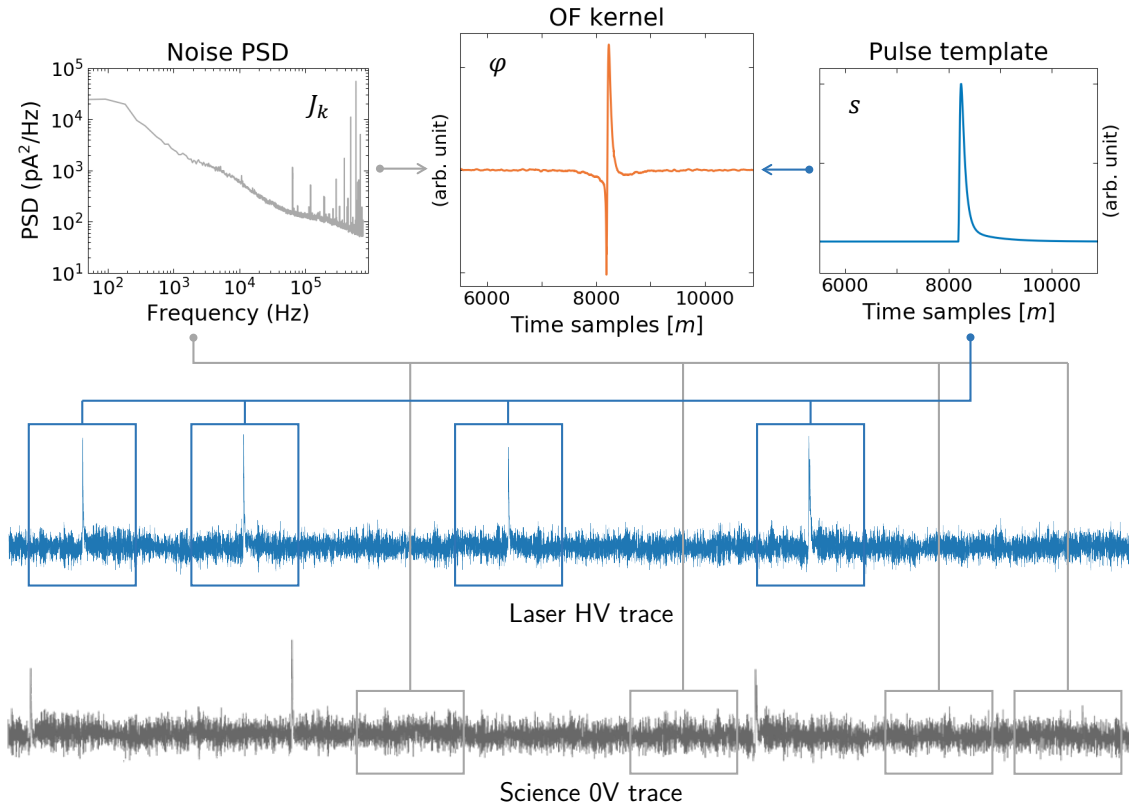


Figure 4.3: A diagram of the Optimum Filter (OF) kernel calculation procedure. The noise Power Spectral Density (PSD) is calculated from snippets of science 0V traces with no pulses. The pulse template is calculated from the pulses in the laser HV data. The kernel is calculated as shown in Equation 4.3. The kernel and the template are shown in time domain, zoomed in on the pulse, while the noise PSD is shown in frequency domain. Fourier transform is used to change between time and frequency domains.

OF amplitude — the best-fit amplitude of the template, fitted to the trace. An interval of 8192 time samples after (and including) the trigger point is blocked from further triggering and is referred to as the tail of event. An equally long interval before the trigger point defines what is called the baseline of event, see Figure 4.4. The average value of the raw trace in this interval is referred to as the mean baseline and is used for event selection (see Section 4.5). Together, the baseline and the tail form an event's trace, for which the OF fit χ^2 values are calculated in both the time and frequency domains.

4.4 Energy Calibration

With a fixed local energy density of the DM halo, the expected abundance of DM particles is inversely proportional to the DM mass. Consequently, the higher the probed DM mass is, the more detector exposure is required to reach the same sensitivity compared to lower

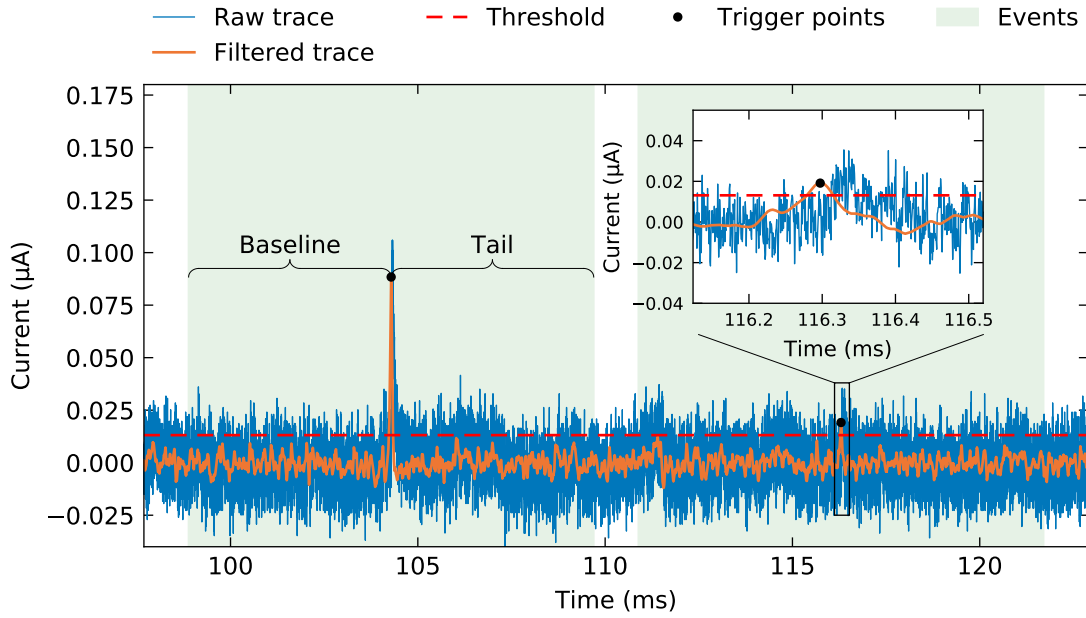


Figure 4.4: Illustration of the Optimum Filter (OF) triggering algorithm. A raw trace (blue) is filtered with the OF kernel to produce the filtered trace (orange). Energy threshold is shown as the dashed red line. Locations of maximum values of the filtered trace after each threshold crossing (black circles) define events (green shaded areas). The inset shows a zoomed in piece of the trace with a small pulse in it, successfully triggered by the described algorithm. The small time offset between the raw and the filtered trace corresponds to the template rise time.

masses. With very low detector exposure, this analysis is only competitive in probing low DM masses, limited from below by the triggering threshold. With that in mind, we do not aim to detect high nuclear recoil energies and define the energy Region of Interest (ROI) of this analysis to be 9.2–250 eV.

To calibrate the OF energy estimator to the phonon energy in the selected ROI, we rely on the laser data collected with a 60 V bias across the crystal. We locate the laser pulses in the data stream using the TTL signal and apply the OF energy reconstruction to them. The energy of the laser photons is $E_\gamma = 1.95$ eV. According to the ionization model described in Section 2.1.1, photons of such energy always create exactly one $e^- h^+$ pair in the crystal. However, multiple photons hit the crystal simultaneously in laser events. The total phonon energy E_n generated in a laser event with n photons is then given by Equation 2.10 multiplied by n with the number of $e^- h^+$ pairs per photon set to 1 and the deposited energy set to the photon energy E_γ :

$$E_n = n(eV_{\text{bias}} + E_\gamma), \quad (4.6)$$

where e is the electron charge and V_{bias} is the bias voltage.

Equation 4.6 is valid for events with full NTL amplification which create quantized peaks in the measured energy spectrum. The bulk CTII effects described in Section 3.1 do not affect the position of the quantized $e^- h^+$ -pair peaks, but only change the energy distribution between the peaks. There are effects, however, that shift the peaks from their expected locations. One such effect is the surface trapping in which in addition to n photons generating the full NTL amplification there is a number of photons in coincidence that create $e^- h^+$ pairs trapped on the hit surface. Another possible effect is the absorption of photons directly in the QETs rather than in the crystal. Such photons create no NTL amplification, but add their energy to the total energy measured in an event. These two effects have two common properties: (a) each such photon generates energy far smaller than the energy of quantized $e^- h^+$ -pair peaks, and (b) the number of such photons is independent of the number of photons n , producing fully amplified $e^- h^+$ pairs. This allows us to model these effects as constant shifts of the quantized peaks, independent of the peak number. The position of the n -th quantized peak in the spectrum is then described by

$$E_n = n(eV_{\text{bias}} + E_\gamma) + \Delta E, \quad (4.7)$$

with ΔE denoting the mean energy that the described effects generate per event.

Due to the TES saturation effect described in Section 2.2.2, the relation between the phonon energy and the amplitude of measured pulses is not perfectly linear. To account for this, we introduce a quadratic correction to the linear relation, which describes the saturation effect sufficiently well in the chosen energy ROI. The relation is then given by

$$E_n = aA_n + bA_n^2, \quad (4.8)$$

where A_n represents the position of the n -th peak in the OF amplitude spectrum, and a and b are the calibration parameters.

To determine the locations of the $e^- h^+$ -pair peaks in the OF amplitude spectrum of the laser data, we fit each peak with a Gaussian function with flat “sidebands”. The sidebands are to account for events between the peaks, caused by the bulk CTII effects. Accurate modeling of the shape of the distribution between the peaks is not required, as it has only a negligible effect on the position of the peaks. The fits and the spectrum are shown in Figure 4.5 (left).

We then determine the value of the shift ΔE as follows:

$$\frac{E_1 - E_0}{E_0} = \frac{eV_{\text{bias}} + E_\gamma}{\Delta E} \approx \frac{A_1 - A_0}{A_0}, \quad (4.9)$$

$$\Delta E = A_0 \frac{eV_{\text{bias}} + E_\gamma}{A_1 - A_0}, \quad (4.10)$$

where we neglect the calibration quadratic correction.

The calibration parameters are found by fitting Equations 4.7–4.8 to the peak positions A_n of the OF amplitude spectrum, as shown in Figure 4.5 (right).

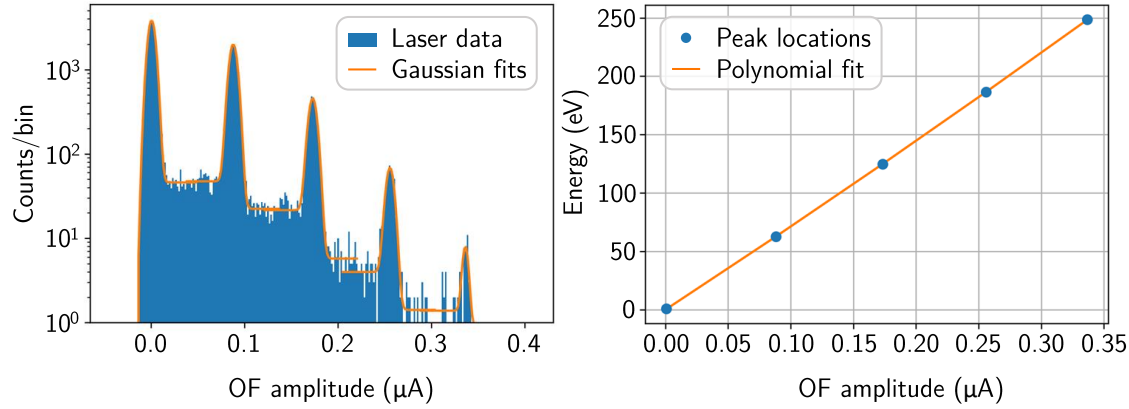


Figure 4.5: HVeV Run 2 energy calibration with laser data. (Left) The spectrum of Optimum Filter (OF) amplitudes of pulses in the laser data acquired with the 60 V crystal bias. The e^-h^+ -pair peaks are fitted with Gaussian functions with flat sidebands. (Right) Locations of the e^-h^+ -pair peaks fitted to their expected energy values given by Equation 4.7 with a quadratic relation given by Equation 4.8. Courtesy of Runze Ren.

We apply the calibration obtained with the HV laser data to the 0V data, assuming that the phonon collection efficiency is the same in the two modes. However, high-energy calibrations with ^{57}Co and ^{55}Fe sources showed an 11% discrepancy between the calibrations in the 0V and HV modes (for more detail, see Ref. [110]). We account for this observation by assigning a systematic uncertainty to the calibration, defined as a multiplicative factor of $1^{+0.11}_{-0.00}$.

4.5 Data Selection

In this section we describe the selection criteria that we apply to the 0V data. The criteria are divided into two categories: the live-time selection criteria remove intervals of detector's live time, in which either the detector response is expected to be abnormal or the background rate is expected to be higher than usual; the data-quality criteria, on the other hand, reject individual events that are unlikely to be caused by DM interactions. For the latter, we calculate the selection efficiency, that is the fraction of DM interactions that would pass the applied selection.

4.5.1 Live-Time Selection Criteria

Temperature Selection

As discussed in Section 2.2.2, the TES working point is defined by the TES bias and the temperature of the thermal bath. At different temperatures, the working point and thus the detector response are different. The detector temperature was not stable throughout the run, because the ADR was operated in cycles. Moreover, high-energy events, such as cosmic-ray muon hits, temporarily heat up the detector, changing the TES working point.

The target temperature on the day when the 0V data were collected was set to 52 mK. To achieve stable detector response, we remove time intervals with temperatures significantly deviating from the target temperature. We apply the selection in two steps:

- the data are divided into 30-second-long intervals, in which the thermometer readout is averaged, and a 3σ selection around the 52 mK peak is applied;
- the same procedure is repeated with 0.1-second-long intervals.

The remaining temperature fluctuations do not exceed 30 μK and have a negligible effect on the detector response.

Mean Baseline Selection

The baseline value of the TES current, that is the current in the absence of pulses, is a better measurement of the TES working point. In addition to the temperature live-time selection, we develop and apply a live-time selection based on the mean baseline of raw traces.

We measure the mean baseline in traces taken from 0.1-second-long intervals of the raw data stream, fit its distribution with a Gaussian, and remove the intervals with the mean baseline deviating from the Gaussian mean by more than 2.5σ , where σ is the width of the Gaussian fit. The overall average baseline is subtracted from all the baseline measurements prior to this procedure.

Figure 4.6 shows a two-dimensional distribution of events' temperature (left) and mean baseline (right) before and after applying both the temperature and the mean baseline live-time selection criteria to the 0V data. The step in the mean baseline after ~ 3 hours from the start of the 0V data acquisition is caused by a spontaneous change of the SQUID working point, which does not affect the detector response. The mean baseline selection procedure outline above is performed separately for times before and after this step.

Power-Line Noise Rejection

As expected, the very low threshold used in this analysis introduces a large number of noise triggers. Their distribution in time is observed to be non-uniform. This can be seen in

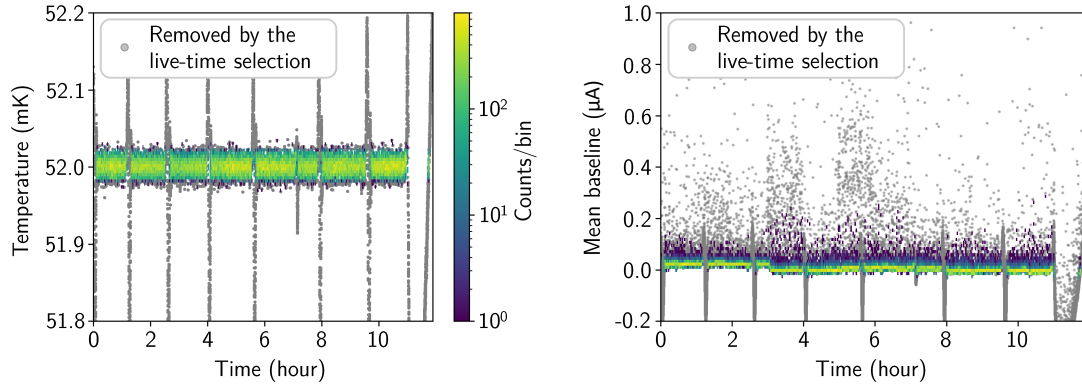


Figure 4.6: Effect of the temperature (left) and the mean baseline (right) live-time selection on the OV data, shown on the event-by-event basis. Preserved events are shown as color-coded heat maps. Removed events are shown as scatter plots with gray markers. Most events with deviating temperatures and baselines are observed in time intervals removed by the corresponding live-time selection. Courtesy of Runze Ren.

the distribution of time intervals between adjacent events shown in Figure 4.7. Distinct peaks are seen at intervals corresponding to 60 Hz frequency lines, as well as less pronounced wider peaks corresponding to 120 Hz frequencies. We identify these features as signatures of power-line-induced noise.

In an ideal scenario, events caused by some specific type of noise would have a different shape, compared to normal pulses. This would allow us to construct a template for the noise events and then use the difference between the χ^2 values of the fits with the noise template and the normal template to identify and reject noise events of this type. However, the observed periodic noise events appeared to have pulse shapes, consistent with the normal template. Therefore, instead of applying the template matching classification, we rely on a live-time rejection, described below.

For each event, we calculate its phase with respect to 120 Hz frequency mode as

$$\varphi_k = 2\pi \frac{t_k}{T} \bmod 2\pi, \quad (4.11)$$

where t_k is the trigger time, $T=1/120\text{s}$ is the selected period, and k is the event index. Events separated by integer numbers of periods T have the same phase. However, due to the varying power-line phase relative to the data acquisition clock, clusters of events with a time-dependent phase were observed, as seen in Figure 4.8. To fit these clusters, we rely on the so-called circular statistics [129]. To each event we assign a complex number z_k with its absolute value equal to unity and its phase equal to the event phase:

$$z_k = e^{i\varphi_k}. \quad (4.12)$$

Then we calculate the mean z -value of events in 3-second-long bins:

$$\langle z \rangle = \frac{1}{N} \sum_{k=1}^N z_k, \quad (4.13)$$

where N is the number of events in each bin. This allows us to calculate the mean phase $\langle \varphi \rangle$, as well as its standard deviation σ_φ in each bin, as defined in Ref. [129]:

$$\langle \varphi \rangle = \arg \langle z \rangle, \quad (4.14)$$

$$\sigma_\varphi = \sqrt{-2 \ln |\langle z \rangle|}. \quad (4.15)$$

We then split the data into one-minute-long intervals, and in each of them fit the time dependence of the mean phase with a fifth-degree polynomial. We use the resulting fit curves to remove $\pm\pi/2$ phase bands around them from the live time. The degree of the polynomial and the width of the band were optimized to reliably cover the clusters of the noise triggers. With such a selection, we reject 50% of the live time, reducing the trigger rate by a factor of 3. The remaining exposure after applying all the live-time selection criteria amounts to 4.77 hours multiplied by the detector mass of 0.932 gram, or 0.185 gram-days.

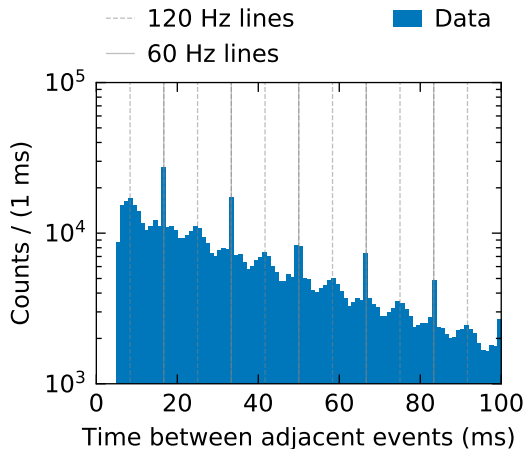


Figure 4.7: Histogram of time intervals between adjacent events in the 0V data, after applying the mean baseline and the temperature live-time selection, as well as the data-quality selection described in Section 4.5.2. Vertical lines show integers of periods corresponding to 120 and 60 Hz. Time correlated events appear as peaks in the histogram.

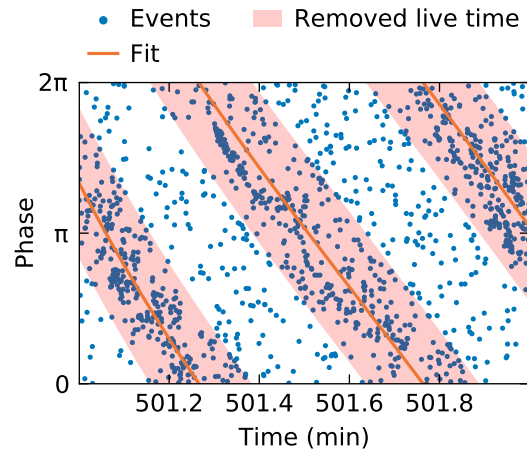


Figure 4.8: One minute of the 0V data in the phase *versus* time plane, illustrating the periodic noise rejection algorithm. Clusters of events, corresponding to power-line-induced noise, are fitted with a fifth-degree polynomial (orange) and live-time intervals around the fit curve are rejected (red).

4.5.2 Data-quality Selection Criteria

In the 0V data, we observed two distinct populations of events with pulse shapes that deviate from the laser pulse template: pulses with prolonged tails and equidistant square pulses. Examples of both classes of abnormal events are shown in Figure 4.9. As shown in Ref. [130], the long-tail pulses are likely caused by bursts of low-energy events (of the order of 4–5 eV) occurring very close to each other in time with an exponentially decreasing rate. The square pulses are caused by the Radio Frequency (RF) noise, picked up by the detector readout. Both of these types of events are unlikely to be caused by DM interactions, therefore we remove them from the data using the OF goodness of fit measures — the χ^2 values, calculated in frequency and time domains.

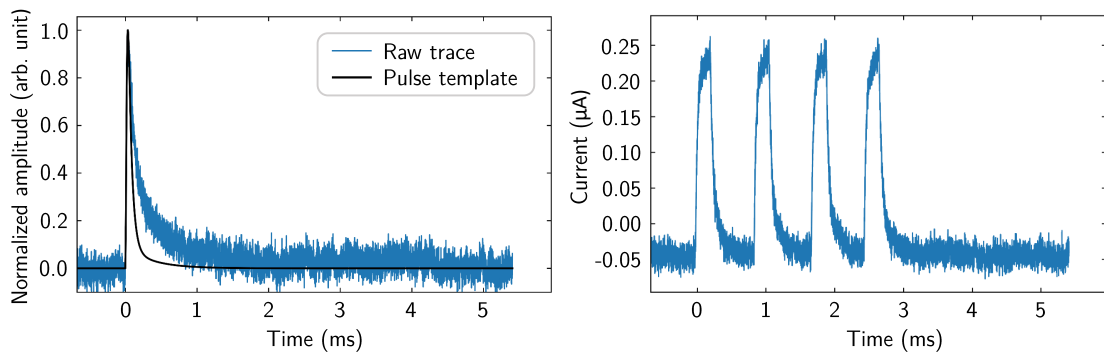


Figure 4.9: Examples of pulses in the 0V data, which are not consistent with the pulse template derived from the laser data. (Left) A long-tail pulse (blue) compared to the pulse template (black). (Right) Packets of Radio Frequency noise.

We use the laser data taken in the HV mode to develop the χ^2 selection criteria. The procedure is identical for the frequency- and time-domain χ^2 criteria. First, we select the energy regions around individual $e^- h^+$ -pair peaks in the χ^2 versus energy plane. Then, following the steps of the HVeV Run 2 HV analysis [84], we fit Gaussian functions to the tips of the distributions of χ^2 values in these energy regions and find such χ^2 values that are 3 standard deviations σ higher than the Gaussian means. After finding the 3σ points, we fit them with a flat linear function, as shown in Figure 4.10. The fit lines define the energy-independent χ^2 selection criteria: events with χ^2 values higher than the fit lines are rejected.

To calculate the selection efficiency, that is the fraction of the DM events that would pass the selection, we use the TTL-triggered laser events as a proxy for DM events. We calculate the fraction of laser events passing both the time- and frequency-domain χ^2 selections in different energy bins and fit the passage fraction with an energy-independent line, as shown in Figure 4.11. To take into account the possible energy dependence, we assign a symmetric systematic uncertainty to the fit result, defined by the difference between the fit value and

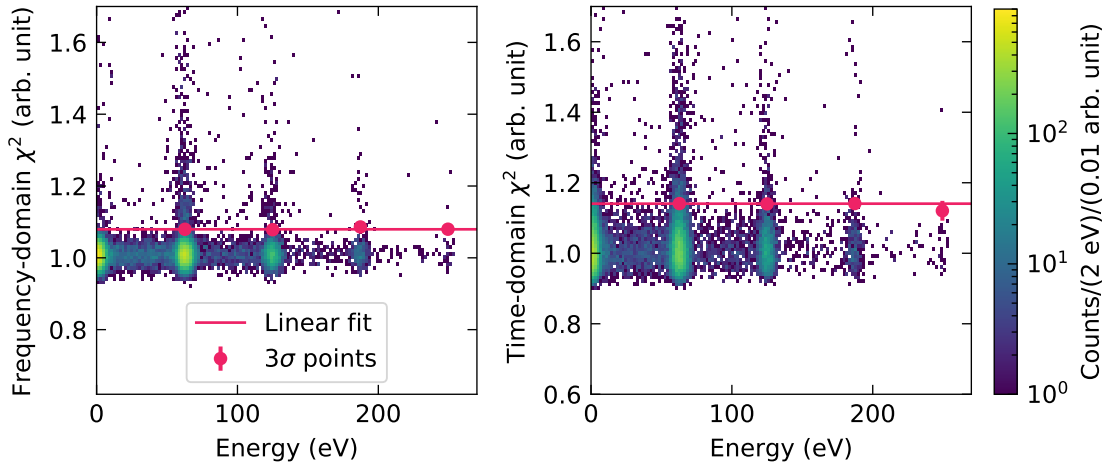


Figure 4.10: Two-dimensional distributions of Optimum Filter fit χ^2 values calculated in frequency (left) and time (right) domains as functions of energy for pulses in the laser data with the 60 V bias. The 3σ points defined in text are shown with pink circles. The energy-independent fits to the 3σ points are shown as pink lines. Events above the fit lines are rejected by the χ^2 selection criteria.

the laser data passage fraction in the first energy bin. The resulting efficiency is $(92 \pm 5)\%$.

4.5.3 Final Energy Spectrum

Figure 4.12 shows the energy spectra of the 0V data before and after applying the data-quality selection criteria. The features below 130 eV removed by the χ^2 selection are caused by the RF pulses. The events removed at higher energies are mostly long-tail events.

Two distinct features are observed in the spectrum with the live-time and data-quality selection applied. Below ~ 15 eV, the spectrum is heavily dominated by noise triggers, as expected from the energy resolution value. The origin of events in the exponentially decreasing spectrum above ~ 15 eV is, however, unknown. As discussed in Section 1.3.1, this feature is observed in other LDM-search experiments and is referred to as the Low Energy Excess (LEE).

4.6 Dark Matter Signal Model

For the expected DM spectrum, we use the SI DM-nucleon recoil signal model discussed in Section 1.2.2, with the differential rate given by Equation 1.2 and the DM halo parameters taken from Refs. [131–133], namely, the asymptotic value of the Maxwellian velocity distribution $v_0 = 220$ km/s, the galactic escape velocity $v_{\text{esc}} = 544$ km/s, the local DM mass density $\rho_{\text{DM}} = 0.3$ GeV/ $(c^2 \cdot \text{cm}^3)$, and the average Earth velocity with respect to the DM halo $v_E = 232$ km/s.

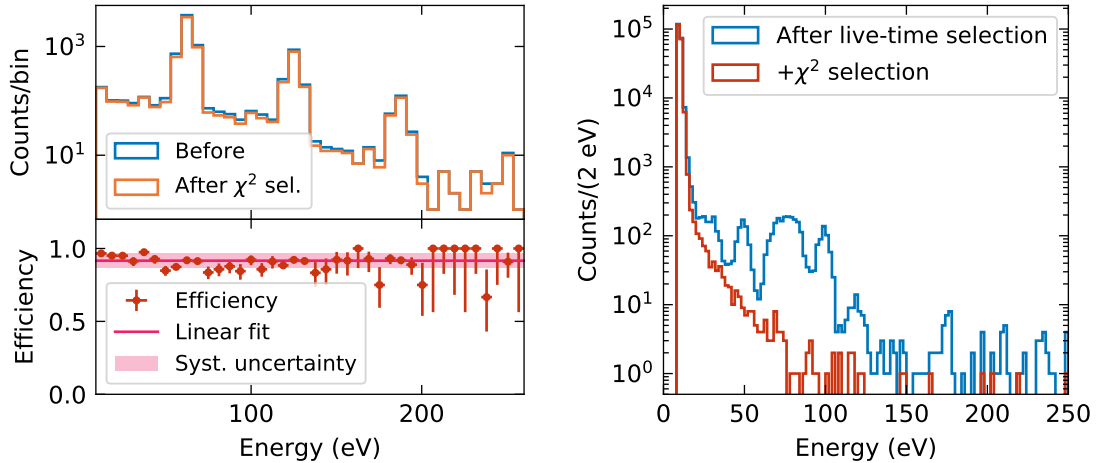


Figure 4.11: Energy distributions of laser events before and after applying both the frequency- and time-domain χ^2 selection criteria. The subplot below shows their ratio in energy bins (red circles), fitted with an energy-independent line (pink), defining the χ^2 selection efficiency. The systematic uncertainty band with the width defined by the difference between the fit and the passage fraction in the first energy bin is shown in pink.

Figure 4.12: 0V science data energy spectrum after applying only the live-time selection (blue) and both the live-time and the χ^2 data-quality selection (red). Events removed by the χ^2 selection are long-tail pulses and Radio Frequency noise.

Detector response effects modify the theoretical signal model energy distribution. In the simplest scenario, the energy distribution is convolved with a Gaussian function to simulate the effect of the detector energy resolution. In our case, however, we observed non-Gaussian energy reconstruction effects near the threshold, in the region heavily affected by noise triggers. We model these effects empirically, by injecting pulses of known energy into noise traces and measuring their reconstructed energy using the processing algorithm applied to the science data. The injected pulses are the laser pulse templates, scaled to different energies in the range from 0 to 260 eV with a 0.5 eV step. We refer to this energy as the true energy E_0 . The pulse-injected traces are processed with the OF triggering and energy reconstruction algorithm, with the triggering threshold set to the value used for the science data. Thus, we obtain a histogram of the reconstructed energies E' for each value in the grid of true energies. Figure 4.13 shows these histograms for three different values of the true energy. The histograms, which are normalized by the number of injected pulses, represent the probabilities $P(E'|E_0)$ of measuring an energy E' when an event with true energy E_0 occurs. We smooth the histograms with a Savitzky-Golay filter and use a bivariate spline interpolation over E' and E_0 to produce smooth $P(E'|E_0)$ functions.

The tails of the $P(E'|E_0)$ probability functions extend the reach of the experiment to

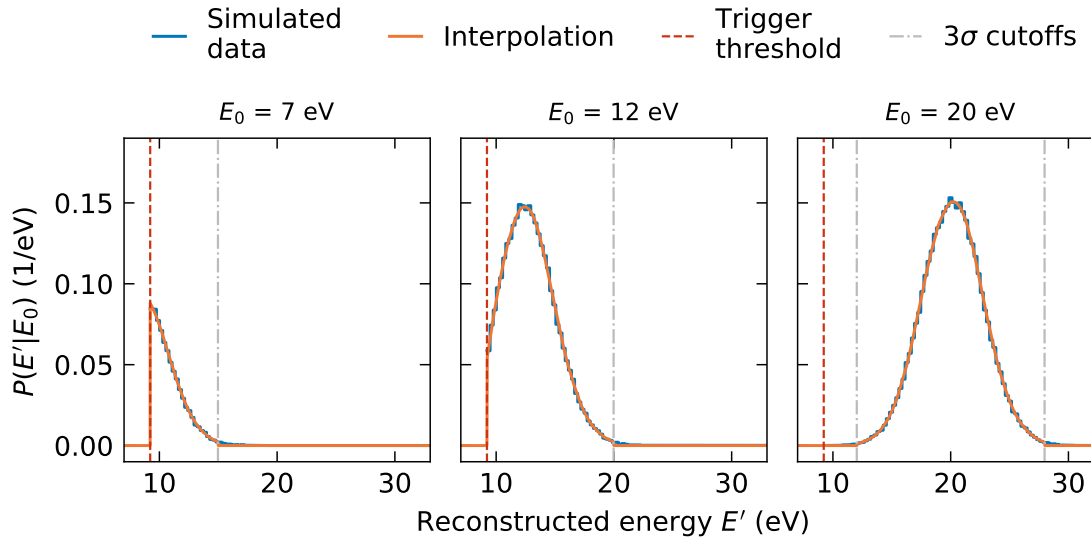


Figure 4.13: Examples of distributions of reconstructed energies E' (blue) with cubic spline interpolations (orange), obtained with injected pulses with different true energies E_0 : 7 eV (left), 12 eV (middle) and 20 eV (right). The histograms are normalized in such a way that the y-axis shows the probability $P(E'|E_0)$ of measuring energy E' when a pulse of true energy E_0 is injected. The trigger threshold is shown as the dashed red lines. The 3σ cutoffs of the distributions are shown as dash-dotted gray lines.

subthreshold values of true energies. For example, an event with true energy $E_0 = 7\text{ eV}$ has a nonzero probability of being reconstructed as an event with reconstructed energy $E' > E_{\text{th}}$, where $E_{\text{th}} = 9.2\text{ eV}$ is the energy threshold of the experiment (see Figure 4.13, left). Technically, if the tails of the $P(E'|E_0)$ functions are long enough, the experiment could be sensitive to arbitrary low energies. We do not have enough statistics to properly model the tails of the $P(E'|E_0)$ functions, so to be conservative, we limit them to the $E' \in (E_0 - 3\sigma(E_0); E_0 + 3\sigma(E_0))$ range, where $\sigma(E_0)$ are the widths of the Gaussian fits to the $P(E'|E_0)$ functions.

To find the expected differential rate of DM events as a function of reconstructed energy, we convolve the differential rate in true energy dR/dE_0 , given by Equation 1.2, with the detector response PDF $P(E'|E_0)$ and multiply it by the trigger and selection efficiencies:

$$\begin{aligned} \frac{dR}{dE'}(E'|m_{\text{DM}}) = & \Theta(E' - E_{\text{th}})\varepsilon(E') \times \\ & \int_{E_0=0\text{eV}}^{\infty} \left[\Theta(E' - E_0 + 3\sigma(E_0)) \Theta(E_0 + 3\sigma(E_0) - E') P(E'|E_0) \frac{dR}{dE_0}(E_0|m_{\text{DM}}) \right] dE_0, \end{aligned} \quad (4.16)$$

where m_{DM} is the DM mass, $\Theta(E' - E_{\text{th}})$ is a Heaviside step function describing the trigger efficiency, $\varepsilon(E')$ is the selection efficiency and $\Theta(E_0 + 3\sigma(E_0) - E')$, $\Theta(E_0 + 3\sigma(E_0) - E')$ are Heaviside step functions describing the 3σ cutoffs of $P(E'|E_0)$. We describe the trigger efficiency with a step function, because the trigger threshold is applied to the same energy estimator as the one used for the energy reconstruction, the OF amplitude. The selection efficiency $\varepsilon(E')$ can in principle have an energy dependence, but in the current analysis we use an energy-independent efficiency model, as described in Section 4.5.2.

Figure 4.14 shows the expected DM differential rates as functions of the true and reconstructed energies of three different DM masses with the SI DM-nucleon scattering cross section $\sigma_n^{\text{SI}} = 10^{-41} \text{ cm}^2$. It is interesting to note that although the entire recoil energy spectrum of DM particles with mass $m_{\text{DM}}=117 \text{ MeV}/c^2$ lies below the energy threshold, we still expect to observe events above the threshold due to the detector noise smearing, included in the detector response function.

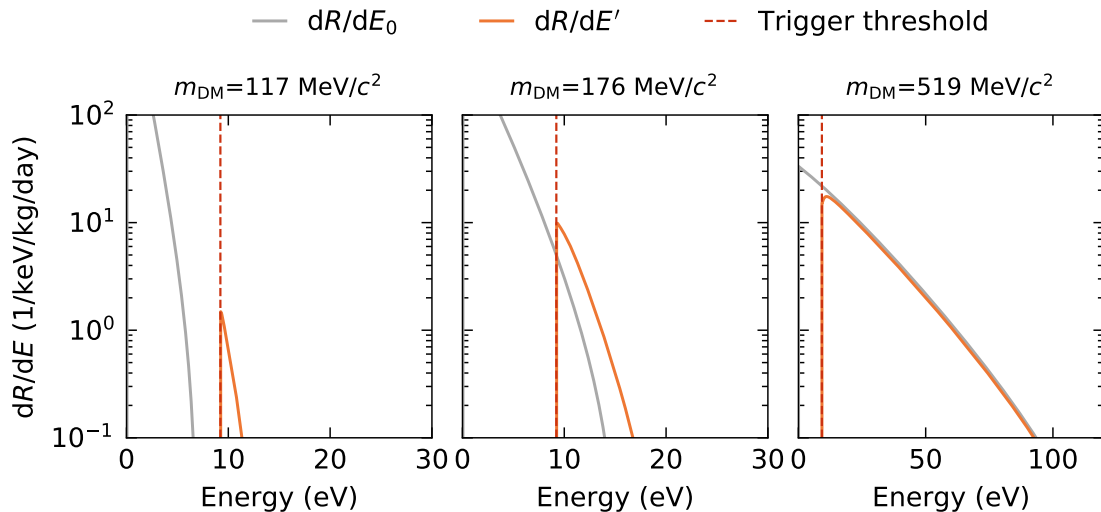


Figure 4.14: Differential rates of Dark Matter (DM) nuclear recoils as functions of true energy (gray) and reconstructed energy (orange) for three different DM masses: $117 \text{ MeV}/c^2$ (left), $176 \text{ MeV}/c^2$ (middle) and $519 \text{ MeV}/c^2$ (right). The trigger threshold is shown as the dashed red lines. At low DM masses, the signal model is boosted above the threshold by the detector resolution. The scattering cross section σ_n^{SI} is set to 10^{-41} cm^2 .

4.7 Dark Matter-Nucleon Scattering Cross Section Limit

Without a background model, we cannot perform a DM search with a discovery potential. However, with the measured energy spectrum shown in Section 4.5.3 and the DM signal model modified by the detector response effects, as described in Section 4.6, we are able to

set an exclusion limit on the SI DM-nucleon scattering cross section. In Section 4.7.1 we find the upper limit of the cross section without considering the Earth shielding effect. In Section 4.7.2 we take into account the shielding effect, which transforms the upper limit into an exclusion region, limited from below and above.

4.7.1 Upper Limit on the Dark Matter-Nucleon Scattering Cross Section

Without assumptions about the experimental background, we use a signal-only hypothesis to find how the observed energy spectrum limits the possible cross-section range with a certain Confidence Level (CL). A method well suited for finding an upper limit of the signal strength in the presence of an unknown background is the Optimum Interval (OI) method [99, 100]. The OI method is a generalization of the maximum gap method [134], which relies on constructing a CDF of the size of the so-called “maximum gap”, defined as the maximum value of the expected number of events in energy regions between adjacent events in the observed energy spectrum. The OI makes a transition from gaps between adjacent events in the spectrum to energy intervals containing a fixed number of observed events n . A CDF of the maximum interval for small values of n is derived in Ref. [99], while Ref. [100] extends the methods to large numbers of observed events. In general, the OI method finds an energy interval which contains especially few events compared to the expected number of events from the signal model and provides an upper limit on the signal strength with a desired CL.

We apply the OI method, as implemented in Ref. [135], to find a 90% CL upper limit on the SI DM-nucleon scattering cross section based on the 0VeV experimental spectrum and the signal model described in Section 4.6. Figure 4.15 shows the measured energy spectrum overlaid by the signal models for four different DM masses. The signal models are scaled to the cross section values, corresponding to the 90% CL upper limit, calculated by the OI. The optimum energy regions, found by the OI method, and shown as the bands of the corresponding colors. The figure shows that for lower DM masses the optimum intervals are near the threshold, so the cross-section limit for such masses is directly affected by the noise triggers. The limit at higher DM masses is significantly less affected by noise triggers, as the OI selects energy regions further away from the threshold.

Figure 4.16 shows the resulting 90% CL upper limit on the SI DM-nucleon cross section, compared to limits obtained in other experiments. For the systematic uncertainty shown on the plot as the light red area, we consider only the uncertainty on the energy calibration, as other uncertainties were found to be largely subdominant. The nominal calibration defines the nominal limit, which coincides with the lower edge of the limit uncertainty band, while the calibration with the scaling factor of 1.11, as discussed in Section 4.4, is used to define the upper edge of the limit uncertainty band. Note that this uncertainty does not have a statistical interpretation, so it is not taken into account in the CL of the limit.

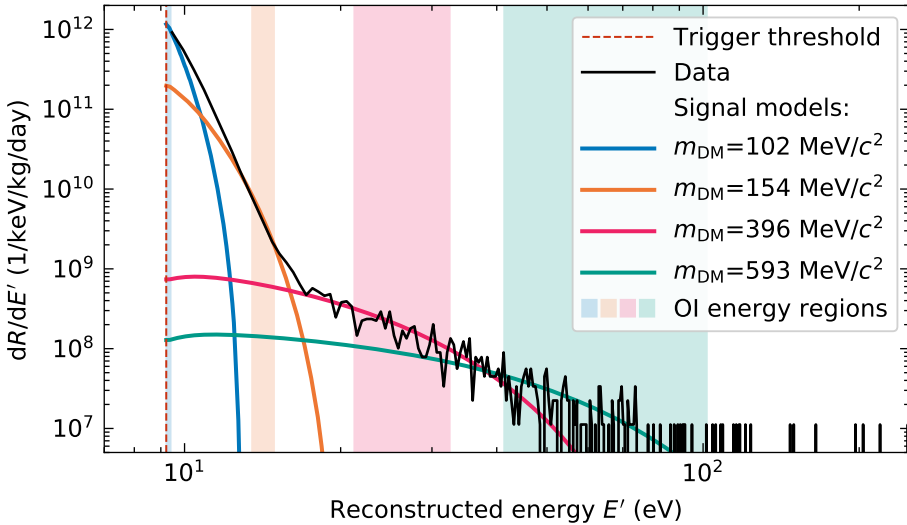


Figure 4.15: Measured energy spectrum (black line) overlaid by the Dark Matter (DM) signal models for four different DM masses (colored lines) with the signal strength calculated by the Optimum Interval (OI) method as the 90% confidence level upper limit. The colored bands show energy regions, selected by the OI algorithm as the optimum energy intervals. The energy threshold is shown as a dashed red line.

4.7.2 Earth Shielding Effect

In the signal model used in this analysis, we assume that the DM velocities correspond to the DM halo velocity distribution at the location of the Earth, without taking into account how interactions of the DM with the atmosphere and crust of the Earth change it. If the cross section of such interactions is small (smaller than 10^{-36} cm^2 , as we show later in this section), the shielding effect of the Earth is negligible. However, at higher cross section values, the DM interactions in the Earth's crust and atmosphere become frequent enough to significantly alter the velocity distribution of DM particles reaching an earthbound experiment or even to block the DM halo wind entirely [140–142]. Several methods have been suggested in recent years to calculate the Earth shielding effect [143–145]. We rely on the method described in Ref. [143] and implemented in the `verne` package [146].

The method uses the standard nuclear-stopping formalism [147] under the assumptions of straight-line trajectories and continuous energy loss. In general, these assumptions are only valid for very heavy particles, $> 10^5 \text{ GeV}/c^2$. However, comparisons with more precise Monte Carlo (MC) approaches showed that this simplified method yields reasonable results even at masses as low as $100 \text{ MeV}/c^2$ [148].

The distances that the particles of the DM halo traverse in the Earth's atmosphere and crust before reaching the detector depend on the angle γ between the vector pointed to the center of the Earth and the vector of the direction of the DM wind, caused by the motion of

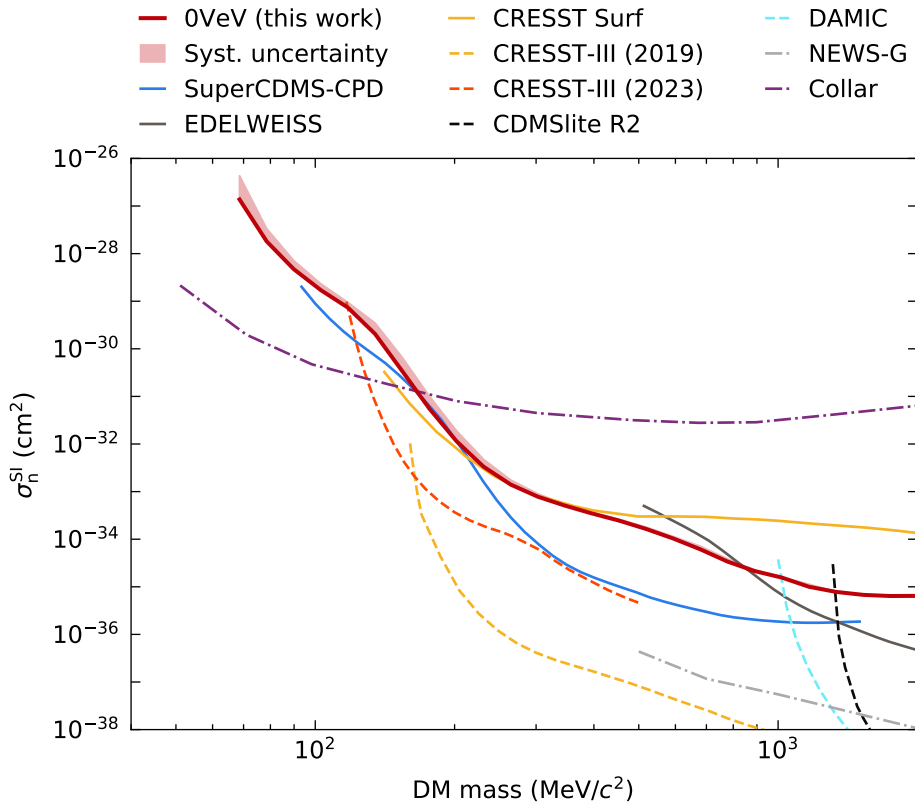


Figure 4.16: 90% confidence level upper limit on the Spin-Independent (SI) Dark Matter (DM)-nucleon scattering cross section (red line) with the systematic uncertainty (light red band). The results of other surface experiments with solid-state detectors are shown as solid lines: SuperCDMS-CPD [79] (blue), EDELWEISS [76] (dark gray) and CRESST [136] (gold). Results of underground experiments with solid-state detectors are shown as dashed lines: CRESST-III (2019) [77] (gold), CRESST-III (2023) [78] (red-orange), CDMSlite [96] (dark gray) and DAMIC [137] (cyan). Other experimental constraints are shown as dash-dotted lines: NEWS-G [138] (light gray) and Collar [139] (purple).

the Earth with respect to the DM halo. The geometry of the Earth rotation around its axis and its revolution around the Sun is implemented within the `verne` package which allows to calculate the time dependence of the angle γ within a given time interval at a given location on the Earth. The result of these calculations for the location of the 0VeV experiment at the date and time at which the 0VeV data were taken is shown in Figure 4.17. $\gamma = 180$ deg corresponds to the vertical direction from above in the detector frame, while $\gamma = 0$ deg corresponds to the vertical direction from below, in which case the DM particles would have to cross the entire Earth before reaching the detector.

With the calculated average DM wind direction, the `verne` package calculates the energy loss of the DM particles crossing the atmosphere and crust (when applicable) and produces the time- and cross-section-dependent DM velocity distributions at the detector location.

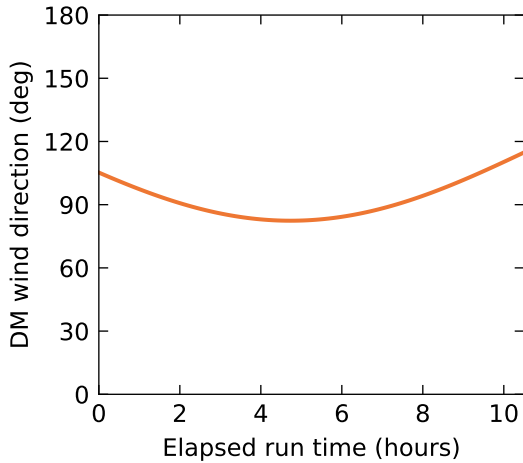


Figure 4.17: Mean Dark Matter (DM) wind direction in the detector frame during the 0VeV run. 180 degrees correspond to the vertical direction from above, that is without crossing the Earth’s crust, while 0 degrees correspond to the vertical direction from below, crossing the entire Earth.

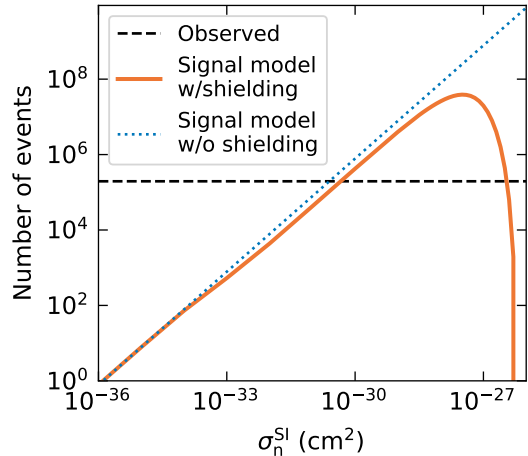


Figure 4.18: Expected number of Dark Matter (DM) nuclear recoils in the 9.2–250 eV energy ROI for DM with 200 MeV/c² mass with (orange line) and without (dotted blue line) the Earth shielding effect. The dashed black line shows the observed number of events in the same energy region, corrected to obtain 90% CL.

These modified velocity distributions are then used in the SI nuclear scattering model [37] instead of the Maxwell-Boltzmann velocity distribution of the Standard Halo Model (SHM) to produce the recoil rates in the detector as a function of time, energy and cross section. Integrating over the run time of the experiment and over the energy ROI, and taking into account the data-quality selection efficiency and the live-time selection live-time loss, the package yields the dependence of the expected number of events on the DM-nuclear cross section in the given energy ROI in the given experiment for a given DM mass.

The result of this calculation for the 0VeV experiment for the DM mass of 200 MeV/c² is shown in Figure 4.18 as an orange line. The expected number of events in the same energy ROI (9.2–250 eV) without the Earth shielding effect is shown as a dotted blue line for comparison. Without shielding, the expected number of events grows linearly with the cross section. However, with the shielding effect, the linearity breaks above $\sim 10^{-33}$ cm², reaching the full shielding at $\sim 10^{-26}$ cm². The expected number of events starts to drop rapidly, and at some cross section value it becomes smaller than the observed number of events (increased to provide 90% CL assuming Poisson statistics; shown as a dashed black line). This cross section value defines the upper boundary of the cross section exclusion region. Values above it are not excluded by the given experiment. Note that unlike the case without shielding, where it is always guaranteed that the number of observed events corresponds to the number of expected events at exactly one cross-section value, in the case with shielding,

it is possible for the number of observed events to be larger than the number of expected events at every cross-section value. In such a case, no cross-section values are experimentally excluded.

For comparison with other experimental results in the same DM parameter space [76, 79, 136] we do not correct the lower boundary of the exclusion region for the shielding effect and use the OI method as described in Section 4.7.1. Note that the OI method relies on the linear scaling of the signal model with the signal strength, so it cannot be applied to a signal model with the shielding effect. For that reason, we calculate the upper boundary of the exclusion region with the `verne` package as described above, using the entire 0VeV energy ROI. At masses below 92 MeV/ c^2 the measured number of events is higher than the expected number of events at all possible cross section values, so no parameter space could be excluded. The resulting exclusion region is shown in Figure 4.19.

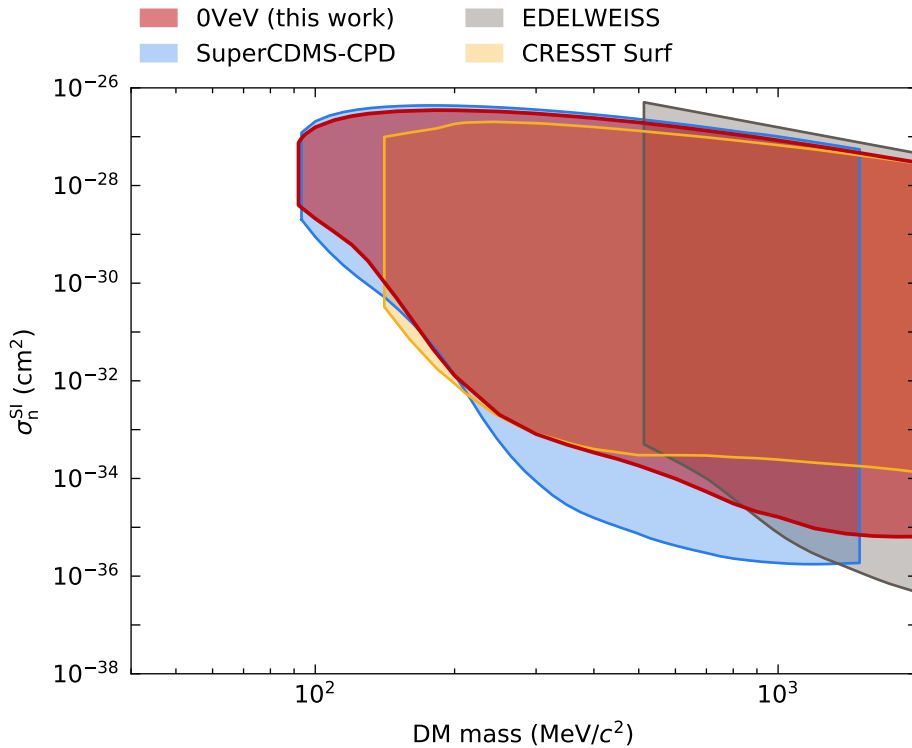


Figure 4.19: 90% confidence level exclusion region of the Spin-Independent (SI) Dark Matter (DM)-nucleon scattering cross section (red). The lower boundary of the exclusion region is calculated with the Optimum Interval method, without the Earth shielding effect. The upper boundary is calculated with the `verne` code in the entire energy Region of Interest of the experiment, taking into account the shielding effect. Other shown exclusion regions with the Earth shielding effect taken into account are from SuperCDMS-CPD [79] (blue), EDELWEISS [76] (dark gray) and the CRESST surface run [136, 149] (gold).

4.8 Discussion

In this analysis, we set the energy threshold at such a low level that the measured energy spectrum is completely dominated by noise triggers near the threshold. This was done in attempt to push the detector sensitivity to lower DM masses, compared to what would be accessible if the threshold was set above the noise-dominated region. In principle, this allowed us to set a limit on the SI DM-nucleon scattering cross section for DM masses as low as $\sim 70 \text{ MeV}/c^2$. However, when the Earth shielding effect is taken into account, the sensitivity to masses below $92 \text{ MeV}/c^2$ is lost due to the maximum expected DM rate in the corresponding energy region being lower than the rate of noise triggers in the detector. In general, the noise triggers are the limiting factor for achieving a better sensitivity to DM masses below $\sim 130 \text{ MeV}/c^2$. In order to improve the sensitivity in this region, a detector with a better resolution is required.

The sensitivity to DM masses below $1 \text{ GeV}/c^2$ is limited by the observed LEE in the recoil energy spectrum below $\sim 100 \text{ eV}$. Similar excesses of events are observed in other experiments, conducted with solid state detectors [90]. Therefore, understanding and mitigating the LEE is the most important task for cryogenic crystalline detector programs. We discuss the progress made in this regard in Chapter 6.

Chapter 5

HVeV Run 3. Dark Matter Absorption and Electron Recoil Search

The 0VeV analysis presented in the previous chapter may be considered a detour from the original HVeV program. As the name suggests, HVeV detectors were designed with the HV mode in mind. In the analysis presented in this chapter, we return to the originally intended operation mode of the HVeV detectors and analyze the data collected in a new HVeV Run, the HVeV Run 3.

Run 3 is the first underground HVeV run and the first run with multiple HVeV detectors operated at the same time within the same housing. In this analysis, we take advantage of the close proximity of multiple HVeV detectors to apply an anti-coincidence event selection in order to veto bursts of external backgrounds. Using data collected in the HV mode, we set exclusion limits on the DM-electron scattering cross section, as well as on the DP kinetic mixing and ALP axio-electric coupling.

This chapter is organized as follows: Section 5.1 introduces and motivates the analysis, Section 5.2 describes the experimental setup and the data processing, Section 5.3 describes the analysis steps applied to the experimental data, including data selection and energy calibration, Section 5.4 outlines the DM signal models and the detector response effects. Finally, Section 5.5 presents the resulting exclusion limits which are discussed in Section 5.6.

5.1 Introduction

Figure 5.1 shows exclusion limits on the DM-electron scattering cross section for the case of a heavy mediator, obtained in the HVeV Run 1 and Run 2 as well as in other direct DM search experiments. Despite a five-fold improvement of the detector resolution and more than a two-fold improvement of the exposure, the Run 2 exclusion limit did not surpass the

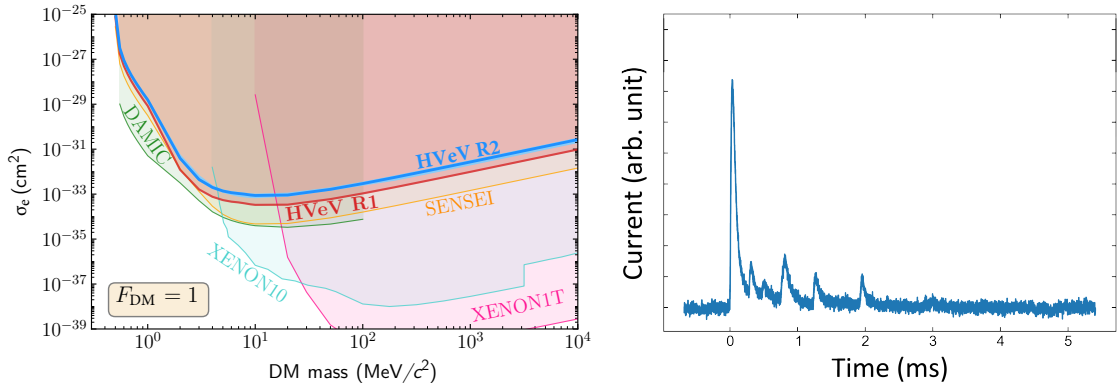


Figure 5.1: The most stringent 90% confidence level exclusion limits on the Dark Matter (DM)-electron scattering cross section for the case of a heavy mediator (form factor $F_{\text{DM}} = 1$) at the time of the HVeV Run 2 publication [84]. The shown limits are from SuperCDMS HVeV Run 1 [83] (red) and Run 2 [84] (blue), DAMIC [82] (green), SENSEI [103] (orange), XENON10 [150, 151] (teal), and XENON1T [85] (pink). Adapted from Ref. [84].

Figure 5.2: Example of a burst event in the HVeV Run 2. Shown is the combined current from the HVeV phonon channels as a function of time.

exclusion limit from Run 1. The reason for this is the excess of background events, the LEE. One especially prominent type of background observed in these runs is what we call burst events — bursts of low-energy events, characterized by strong time correlations. An example of a burst event in Run 2 is shown in Figure 5.2. In HVeV Run 3 we attempt to reduce this background or to mitigate its effect on the DM sensitivity.

Both HVeV Run 1 and Run 2 were conducted in a surface facility with no shielding. Run 3, on the other hand, is conducted underground with ~ 100 m of rock overburden and a ~ 20 cm thick lead shield. Moreover, unlike Run 1 and Run 2 in which only one HVeV detector was used, there are four HVeV detectors operated in the same housing in Run 3. If the source of the burst events is external, that is if they are not caused by detector effects, they should be seen in coincidence in detectors operated in a direct proximity of each other.

The idea of Run 3 is to see whether shielding from cosmic rays and ambient radiation, as well as an application of an anti-coincidence event selection could improve the DM sensitivity of HVeV detectors. Using the data acquired in the nominal HVeV operation mode, the HV mode, we set exclusion limits on the electron-coupled DM, aiming to reach unexplored parameter space of the DM-electron recoils, the DP absorption and the ALP absorption.

5.2 Experimental Setup, Data Acquisition and Data Processing

5.2.1 Experimental Setup

HVeV Run 3 took place between December 2020 and February 2021 at NEXUS, Fermilab. The facility provides 107 m of rock overburden [152], which reduces the cosmic muon flux by approximately one order of magnitude [153]. In addition, one layer of lead bricks was used to shield the detectors from the natural radiation background in the cavern.

A dilution refrigerator was installed within the shield. Unlike the ADR utilized in the previous runs, the dilution refrigerator provides a stable temperature without daily cycles. A light-tight copper housing for the detectors was thermally coupled to the cryostat mixing chamber kept at a stable temperature of 10.5 mK throughout the run. Four HVeV detectors were mounted in pairs on two copper holders. Each detector was clamped between two PCBs facing the neighboring detectors, as shown in Figure 5.3.

The four detectors deployed in this run are introduced in Section 2.3.3. One of the four detectors was not operational. Two of the remaining detectors were produced from the same silicon wafer as the HVeV Run 2 detector and differ from each other by their QET configuration masks. We refer to these detectors by their QET mask labels: NFC and NFH. The third operational detector is a copy of the HVeV Run 1 detector — it was produced from the same wafer as the Run 1 detector and has the same QET mask. We refer to this detector as R1.

Each detector has two channels, which are read out with SQUIDs. A SuperCDMS Detector Control and Readout Card (DCRC) was used to operate the detectors, digitize their signals and perform data acquisition, as described in Section 5.2.2.

With the fourth detector not being operational, the NFC detector was the only one with other operational detectors on both sides. This is crucial for the anti-coincidence event selection, applied to suppress external backgrounds as described in Section 5.3.1. Therefore, expecting a better background suppression in the NFC detector and knowing that the previous HVeV DM searches were background limited, rather than exposure limited, we use only the NFC detector for the DM search. The NFH and R1 detectors are used only as veto detectors. In the remainder of this chapter, if not specifically mentioned, the NFC detector is implied on plots and in text.

As in the previous runs, a 1.95 eV laser was used as a source of calibration events. Photons from the laser were transmitted into the detector housing through a polished optical fiber, inserted into the bottom of the housing between the detector holders. In such a setup, it is not guaranteed that the photons will hit any of the detector faces. Instead, they are likely to scatter off of the housing walls and holders, and may eventually hit any of the crystal surfaces, including the sidewalls. This is different from previous runs, in which the fiber was pointed directly onto a detector's top or bottom face.

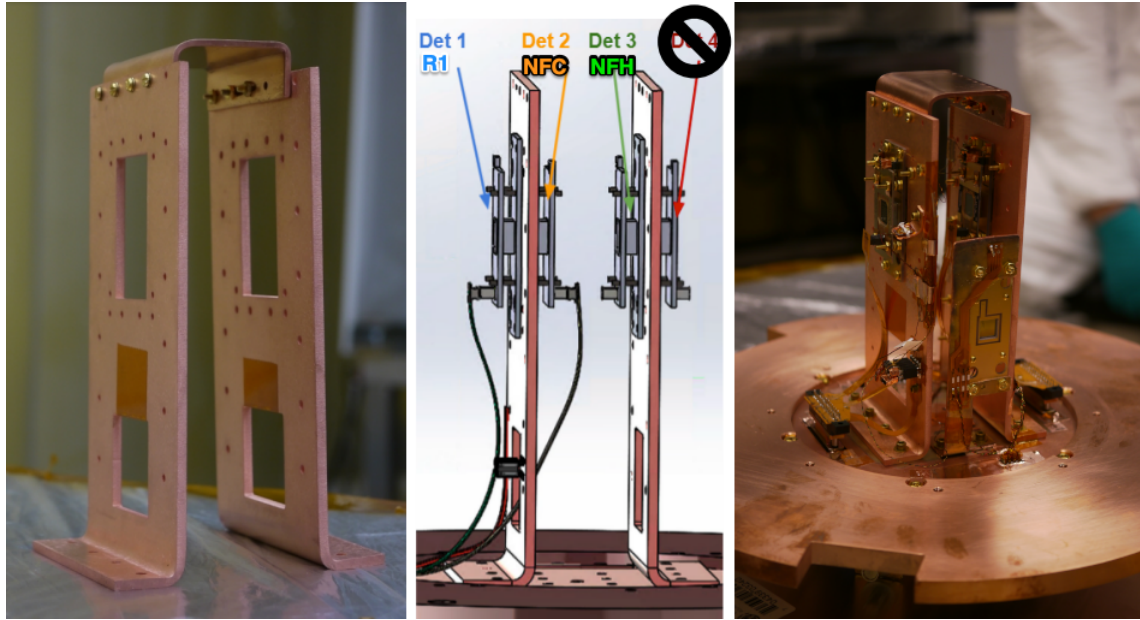


Figure 5.3: (Left) Copper detector holders with a connecting bracket on top for stiffness. Large rectangular holes in the holders provide a line of sight between detectors that are to be mounted on different sides of the holders. (Middle) Computer rendering of the detector setup. Four HVeV detectors are shown attached in pairs to the holders. The bracket connecting the holders is not shown. (Right) Assembled experiment payload. The Printed Circuit Board in the foreground is for conducting tests that are not discussed within this dissertation.

We collected calibration data, referred to as laser data, with the laser fired in 500 ns short pulses. The exact time of the laser pulses was recorded by the DCRC using the TTL signal. Detector pulses in coincidence with the pulses in the TTL signal are referred to as TTL-triggered events and are associated with the laser photons.

28 continuous days of science data were collected throughout Run 3. Laser data were collected throughout the run, with three main calibration data sets collected at the end of the run, which differ by laser intensity and pulse frequency.

5.2.2 Data Acquisition

In previous HVeV runs, we utilized custom Data Acquisition (DAQ) systems to continuously sample and save on disk the entire time series of the detector channels' current. This approach allowed us to run and optimize different trigger algorithms for different studies offline. In Run 3, however, we used a SuperCDMS DCRC board running SuperCDMS MIDAS DAQ, developed for the main SuperCDMS detectors, HV and iZIP, and thus not designed for continuous data sampling. The limited DCRC throughput (~ 4 MB/s) did not allow us to collect the entire data stream from the four detectors, each with two channels. Instead we utilized the DCRC's random triggering mode in which live-time intervals of configurable

constant length are alternated with dead-time intervals whose lengths are drawn randomly from a configurable uniform distribution (see Figure 5.4). The live-time intervals in one channel coincide with the live-time intervals in all other detectors and channels. We set their length to 0.5 s and refer to them as MIDAS traces. The lengths of the dead-time intervals were set to be distributed between 0 and 1 s, resulting in a collection of 50% of live time. The sampling frequency is 625 kHz.

As in the previous run, traces from the inner and outer channels are summed together in each detector.

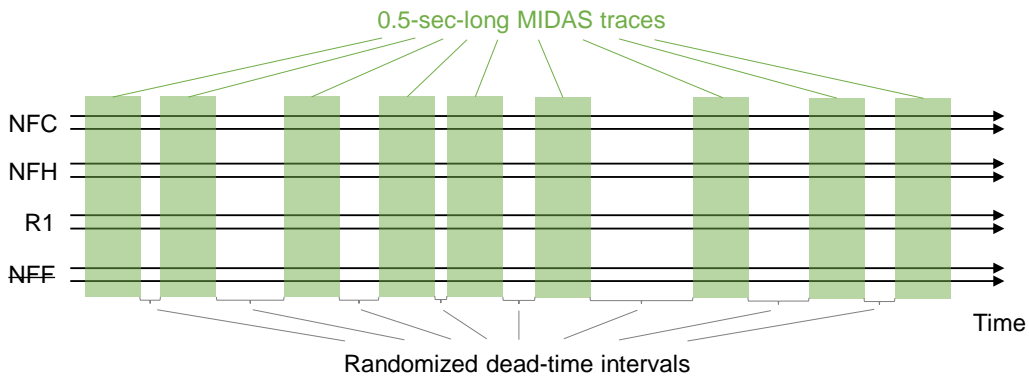


Figure 5.4: Sketch of the MIDAS random triggering algorithm used in HVeV Run 3. Green bands show 0.5-second-long MIDAS traces with 8 channels, two per each detector. Dead-time intervals between the MIDAS traces are randomized.

5.2.3 Pulse Template

We use laser data collected throughout the run to reconstruct pulse templates for each detector. The template comes from the average of the signals in a window of 8192 time samples (± 6.55 ms) centered around the TTL triggers. Traces with unusually large slopes are removed from the selection. High-frequency noise, remaining after the averaging, is suppressed with a fifth-order forward-backward Butterworth filter with the cutoff frequency set to 60 kHz for the NFC and NFH detectors and to 20 kHz for the R1 detector. The difference between the cutoff frequencies is motivated by the higher level of noise in the R1 detector. The resulting templates for each of the detectors are shown in Figure 5.5.

5.2.4 Triggering

We look for events in MIDAS traces by passing them through a trigger algorithm offline. To facilitate studying of burst events, the trigger algorithm should satisfy two conditions: it should a) introduce as few false triggers as possible and b) issue separate triggers for closely lying pulses. In previous HVeV analyses, we applied different filters to the traces

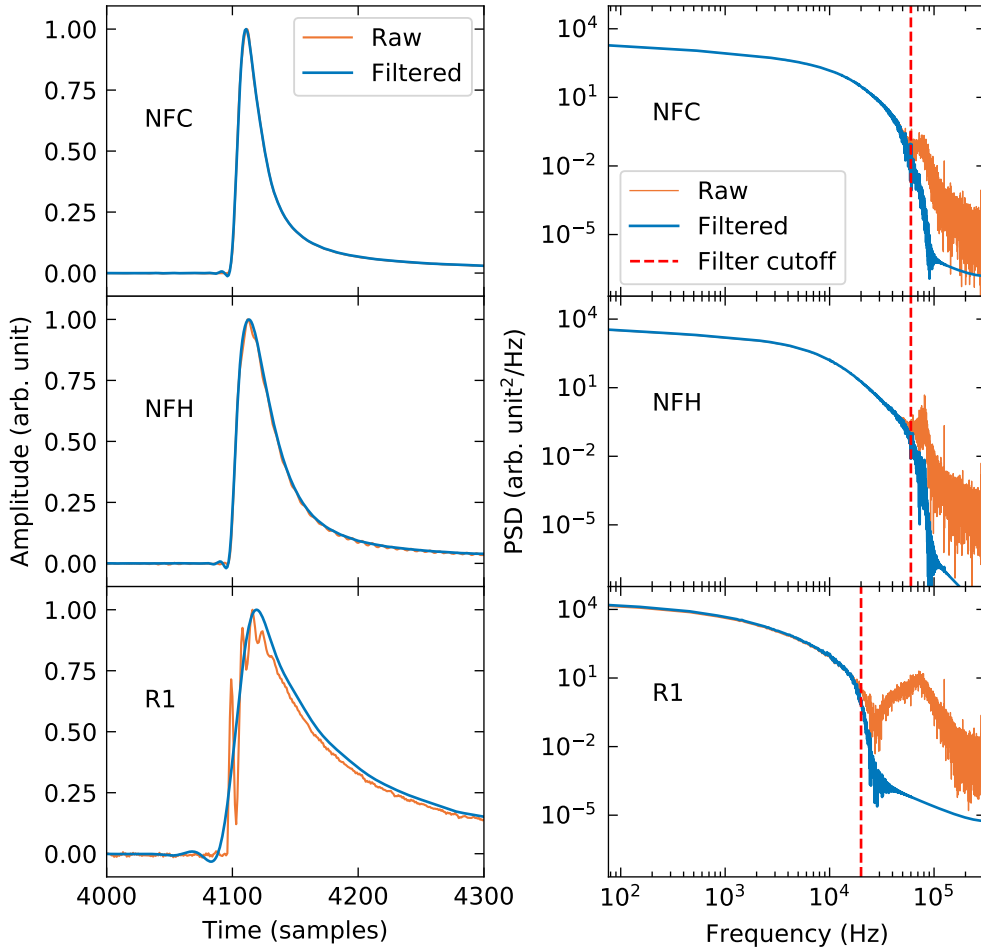


Figure 5.5: Pulse templates constructed with the laser data for each detector in time (left) and frequency (right) domains with (blue) and without (orange) low-pass filter. The filter frequency cutoff is shown as a dashed vertical line.

before threshold triggering. In the analysis of high voltage HVeV Run 2 data, a Matched Filter (MF) was used: traces were cross-correlated with a pulse template [84]. In the 0VeV analysis, we used OF, as described in Chapter 4. However, neither of these techniques performs well with closely lying pulses. Traces filtered with OF or MF tend to stay above the threshold for an extended period of time after each pulse. This problem is solved by using a filter with a short kernel with a negative dip in it. In this way, the filtered traces go down below the threshold immediately after each pulse. We use a Gaussian Derivative Filter (GDF) — convolution of traces with a first derivative of a Gaussian function. It not only forces the

filtered traces to dip below the threshold after each pulse, but is also not prone to introduce false triggers, unlike the OF which sometimes causes “ripples” around high-energy pulses, causing multiple triggers.

We optimize the parameters of the GDF kernel to achieve the best triggering efficiency while keeping the noise rate low. The kernel used for the GDF is a derivative of a Gaussian function, truncated at $\pm 3\sigma$, where σ is the width of the Gaussian set to 16 time samples (25.6 μ s). With such settings, the GDF trigger allowed us to resolve pulses separated by as little as 75 time samples (120 μ s). An example of pile-up event is shown in Figure 5.6: for each pulse in the raw trace, there is a corresponding threshold crossing in the trace filtered with the GDF. The trace filtered with an MF, however, does not fall under the threshold fast enough, causing only one trigger point for two pulses of close proximity.

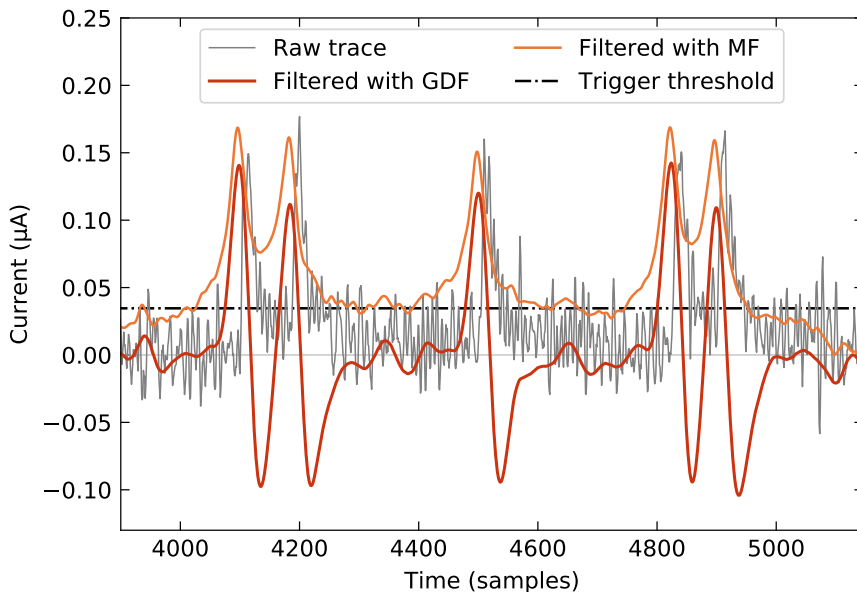


Figure 5.6: A comparison of the Gaussian Derivative Filter (GDF) and Matched Filter (MF) triggering applied to a pile-up event. The raw trace (gray) is filtered with the GDF (red) or MF (orange). Triggering threshold is shown as a dash-dotted line. The trace filtered with GDF falls below the threshold immediately after each pulse, allowing to trigger on each pulse individually. The trace filtered with MF stays above the threshold for longer times, missing closely lying pulses.

After filtering MIDAS traces with GDF, we apply a simple threshold trigger to find pulses. In the NFC and NFH detectors we set the thresholds to approximately correspond to 25 eV of phonon energy. With this choice we intend to minimize the fraction of noise triggers, while still triggering on most of the sub-eh-peak events caused by partial NTL amplification. The R1 detector showed a significantly higher noise intensity; therefore, we increased the threshold in this detector to correspond to ~ 50 eV.

We calculate the efficiency of the trigger algorithm in bins of reconstructed phonon

energy by applying it to the laser data and counting the fraction of TTL-triggered laser events that are also triggered by the GDF trigger. Figure 5.7 shows trigger efficiency curves for each detector. The energy reconstruction and calibration used to produce these curves are described later in this chapter. The R1 detector was not calibrated, therefore, its trigger efficiency curve is shown in uncalibrated units (see Section 5.2.5). The selection criteria, applied to the laser data, are discussed in Section 5.3.2 and Section 5.3.3. The trigger efficiency curves are well fitted with error functions, with their widths arising from the energy resolutions of the detectors and their amplitudes being very close to unity, meaning that the efficiencies are almost 100% at energies sufficiently higher than the trigger thresholds.

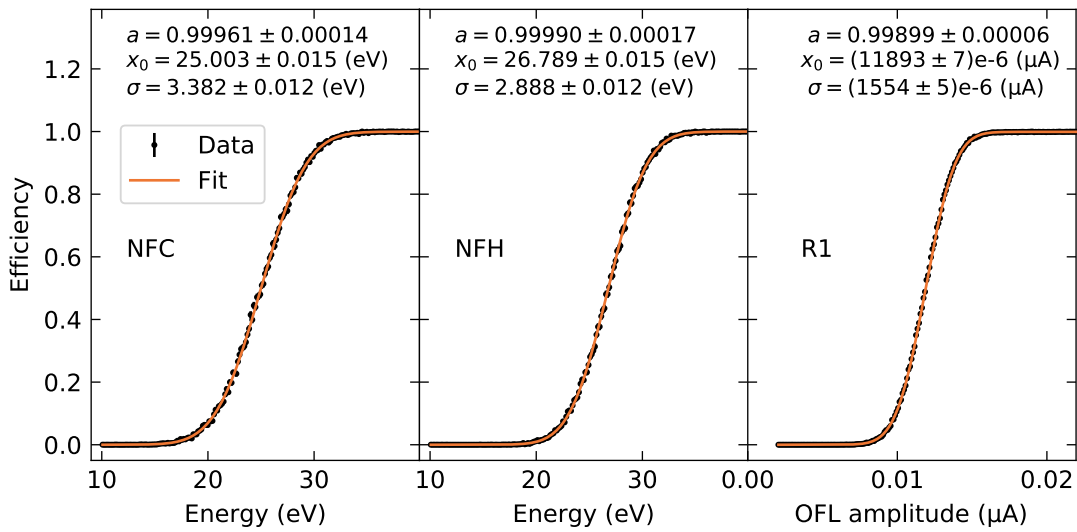


Figure 5.7: Trigger efficiency for NFC, NFH and R1 detectors calculated with TTL-triggered laser data and fitted with error functions with amplitude a , location x_0 and width σ . The R1 detector is not calibrated, therefore the x-axis is shown in Optimum Filter energy estimator units (OFL).

Ideally, we want the trigger time points to be aligned with the exact times of the energy depositions causing these triggers. However, the points at which the filtered traces cross the threshold do not exactly correspond to these times. We perform the following steps to correct this misalignment. First, for each trigger we define a time window that starts where the filtered trace crosses the threshold in the upward direction and ends where it crosses it again in the downward direction (see Figure 5.8). The trigger location is then initially defined as the location of the maximum of the filtered trace within this window. However, this location is still not perfectly aligned with the energy deposition time. To measure the remaining offset, we apply the GDF to the pulse template of each detector, find the location of its maximum, and measure its offsets from the template centers, which correspond to the energy deposition time by construction (see Section 5.2.3). This offset, individually determined for each detector, is subtracted from every trigger location to define

the corrected trigger locations, shown in Figure 5.8 as a red dash-dotted line. In principle, the offset can depend on the pulse amplitude; however, we observed that in the energy ROI of this analysis the energy dependence is negligibly small. As Figure 5.8 shows, the final trigger location is very well aligned with the start of the pulse.

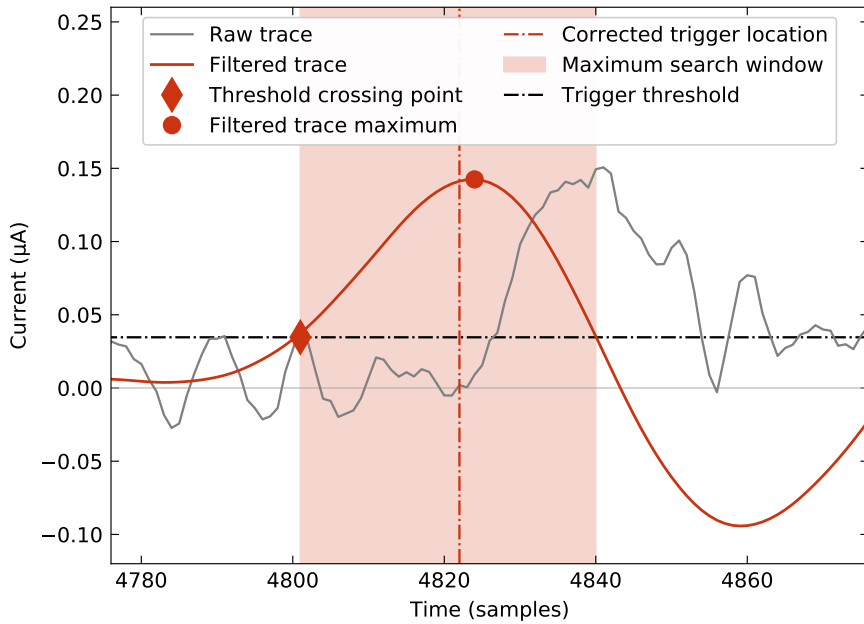


Figure 5.8: An illustration of the trigger alignment algorithm. Raw trace (gray) is filtered with the Gaussian Derivative Filter (GDF) (red). The intersection of the filtered trace with the trigger threshold (dash-dotted black line) is shown as a diamond marker. The maximum of the filtered trace is shown as a round marker. The final corrected trigger location is shown as a vertical dash-dotted line.

For further processing, we cut out trace intervals that span ± 4096 time samples around each trigger. Margins around trigger locations are necessary for the OF energy reconstruction. This forces us to reject triggers occurring on the edges of MIDAS traces, which effectively results in a loss of live time. The fraction of lost live time is calculated as the ratio between the pulse template length (8192 samples) and the MIDAS traces length (0.5 seconds or 312500 samples), which is approximately equal to 2.6%.

In addition to the GDF triggers, we randomly select 5 uniformly distributed time points in each MIDAS trace. The only restriction that is applied to the otherwise purely random distribution is that the triggers are not allowed to be closer than 4096 time samples to the MIDAS trace edges. We use these triggers for various studies throughout the Run 3 analysis, such as the mean baseline (Section 5.3.1) and the baseline energy resolution (Section 5.4.2) studies.

5.2.5 Energy Reconstruction and Reduced Quantities

Each trigger, be it a TTL trigger, a GDF trigger or a random trigger, defines an “event”, spanning a window of ± 4096 time samples around it. These events are processed in the same way independently of their trigger type.

The essential part of the processing is the reconstruction of the pulse energy, performed with the OF. The pulse templates, required for the OF, are defined in Section 5.2.3. The other necessary component of the OF is the noise PSD. We calculate noise PSDs in each detector by selecting intervals of raw MIDAS traces with no pulses in them. The PSDs are calculated for every minute of data, as some of the noise frequency lines were changing on a minute scale. Processing of events from a particular minute of data uses the noise PSD calculated for this minute. Figure 5.9 shows a random selection of noise PSDs from different detectors.

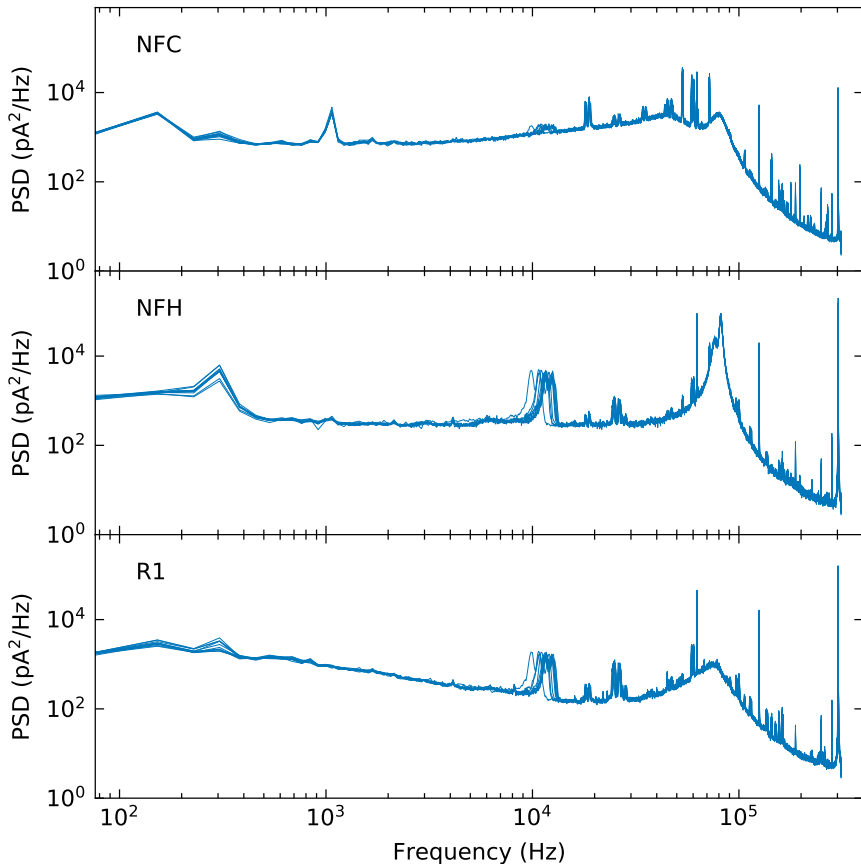


Figure 5.9: A selection of noise Power Spectral Densities (PSDs) in NFC, NFH and R1 detectors, calculated in random one minute intervals. An unstable 10 kHz noise line is observed in NFH and R1 detectors.

We use three different OF variations for different purposes:

- OF with no time shift (OF0): a template is fitted to an event at the trigger point, without a time shift. This OF variant is used to analyze TTL-triggered laser events, since their trigger locations exactly correspond to the energy deposition times.
- OF with a limited time shift (OFL): the pulse template is allowed to shift in a ± 15 time samples ($\pm 24 \mu\text{s}$) window with respect to the trigger point, searching for the best OF fit χ^2 value. This is necessary to correct the residual trigger misalignment caused by noise. Since the traces in the processing stage are of the same length as the template, the template wraps around the trace edges when the time shift is performed.
- OF with pile-up (OFP): simultaneously fits two identical templates to the trace, with independent amplitudes and time shifts. The time shifts are limited to ± 250 time samples. This OF variant is implemented as shown in Ref. [128] and used to better identify and reject pile-up events by means of comparing the two-template fit χ^2 to the one-template fit χ^2 (see $\Delta\chi^2$ selection criterion in Section 5.3.3).

Pulse amplitudes, time offsets and frequency-domain fit χ^2 values, calculated with these OF variants, are saved as Reduced Quantities (RQs) and summarized in Table 5.1. Note that when the OF fits are performed, the full frequency range is used for the χ^2 optimization. However, the `chi2` RQs are calculated to include only the frequencies below 30 kHz. This removes the effect of high frequencies on the selection criteria developed with the RQs, as the high frequencies do not contain information related to pulses.

The other RQs used in the analysis include the trigger location within the MIDAS traces `trig_loc`, the global time of the trigger `timestamp`, the MIDAS filename index `filename_idx` and the mean baseline `meanbase` — the mean value of the trace baseline, filtered with a Butterworth filter (same as the one applied to the pulse template). The baseline is defined as the first 4086 samples of the trace. The 10 samples margin to the trigger location is to ensure that the pulse onset is not within the baseline.

5.3 Measured Energy Spectrum

This section describes the steps we take to produce an energy spectrum of “good” events observed in the experiment, that is the events that could be DM events, observed in times when the rate of background events is the lowest. These steps include: science data live-time selection, intended to remove time intervals with poor detector performance or high background rates (Section 5.3.1); laser data live-time selection that mimics the science data selection criteria (Section 5.3.2); data-quality selection, applied to both science and laser data to remove poorly reconstructed pulses, as well as the calculation of the selection

Table 5.1: List of RQs used in the HVeV Run 3 analysis

RQ	Description
OF0	Pulse amplitude, reconstructed with OF0
OF0_chi2	OF0 fit frequency-domain χ^2 , limited to frequencies lower than 30 kHz
OFL	Pulse amplitude, reconstructed with OFL
OFL_time	Template shift in OFL fit
OFL_chi2	OFL fit frequency-domain χ^2 , limited to frequencies lower than 30 kHz
OFP_chi2	OFP fit frequency-domain χ^2 , limited to frequencies lower than 30 kHz
filename_idx	Index of MIDAS filename. Used for splitting the data into fractions (e.g. 10% and 90% in Section 5.5.3)
trig_loc	Trigger location within the MIDAS trace, measured in time samples
timestamp	Global trigger location time stamp in seconds
meanbase	Mean value of the first 4086 time samples of the trace, filtered with Butterworth filter
temperature	Mixing chamber temperature

efficiency (Section 5.3.3); and lastly, the energy calibration (Section 5.3.4). Section 5.3.5 shows the spectrum used in the HVeV Run 3 DM search.

5.3.1 Science Data Live-time Selection Criteria

Intersecting MIDAS traces

Although by design the MIDAS DAQ random trigger feature is supposed to create dead-time intervals between adjacent MIDAS traces, we observed that a very small fraction of MIDAS traces intersect with each other. This causes double counting of events in them, therefore we identify such traces using the global time RQ and remove them from both the science and the laser data. The amount of live time removed due to this effect is only 0.006%. This selection is always applied to the data, as without it the live-time calculation and the event count calculation are not correct.

Mean Baseline Selection

When a high-energy event, such as a cosmic-ray muon event, occurs in a detector, the detector's temperature temporarily increases, changing the TES working point. Therefore, it is in our interest to exclude time periods with fluctuating detector temperature from the experiment's live time.

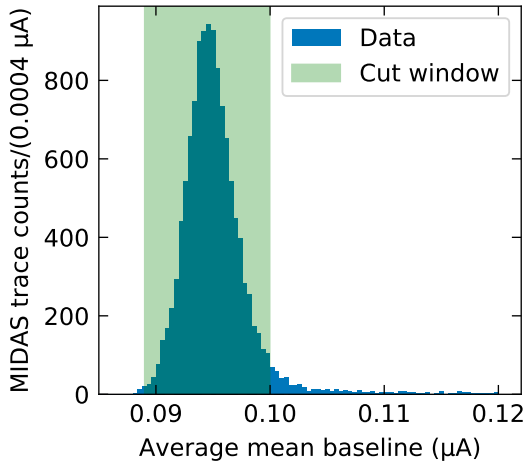


Figure 5.10: Distribution of mean baseline of MIDAS traces in one of the science data sets. A band of ± 3 standard deviations from the average value is shown in green. MIDAS traces outside of the window are removed from the live time of the experiment.

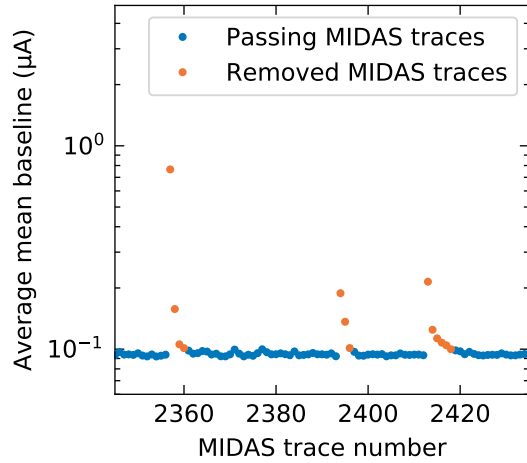


Figure 5.11: Mean baselines of MIDAS traces as a function of time. 3 large energy depositions are visible. The traces shown in orange are removed from the live time of the experiment. Traces shown in blue pass the selection.

The TES current baseline is an excellent proxy for the detector temperature, so we use it to identify the periods of deviating temperature. We estimate the baseline of each MIDAS trace by averaging the mean baseline RQ of the random triggers taken from this trace. Then we build distributions of average MIDAS trace baselines on a series-by-series basis, fit them with a Gaussian function, and remove traces from the live time that have the baseline deviating from the series mean by more than 3 standard deviations, as illustrated in Figure 5.10. This removes 6.0% of the science data live time. Figure 5.11 shows examples of time intervals with temporarily increased temperatures, successfully removed by the described selection.

Temperature Selection

Although the mean baseline selection removes short temperature fluctuations, it does not help if the detector temperature differs from day to day. In principle, this should not happen since the temperature was stabilized with a feedback control system using a thermometer installed on the cryostat mixing chamber. However, during the run the temperature control software failed twice, causing the temperature to rise to a higher level. We identify the series in which this problem occurred using the temperature logs and remove them from the live time. The loss of live time due to this selection is 4.4%.

Anti-coincidence Selection

We expect to register DM events as a Poisson process — they should be random and independent from one another. Moreover, due to a low expected DM interaction cross section, coincidence of DM events in several detectors is very unlikely. This allows us to remove a) burst events and b) coincident events from the DM search data. We achieve both of these goals by applying a selection criterion based on the events' Δt values — the time to the closest event in the same detector (removes bursts) or in the other detectors (removes coincidences). Figure 5.12 shows the distributions of the Δt values for events in the NFC detector. Different colors correspond to the choice of reference detector: if NFC itself is used as a reference detector, then the Δt is calculated between adjacent events in NFC; if another detector is used as a reference, then for each event in NFC the Δt is calculated as a time interval to the closest event in the specified reference detector. For independent events that come from a Poisson process, such distributions take the form of an exponentially decaying function. However, in the experimental data we see distinct peaks at 0, indicating the presence of correlated events.

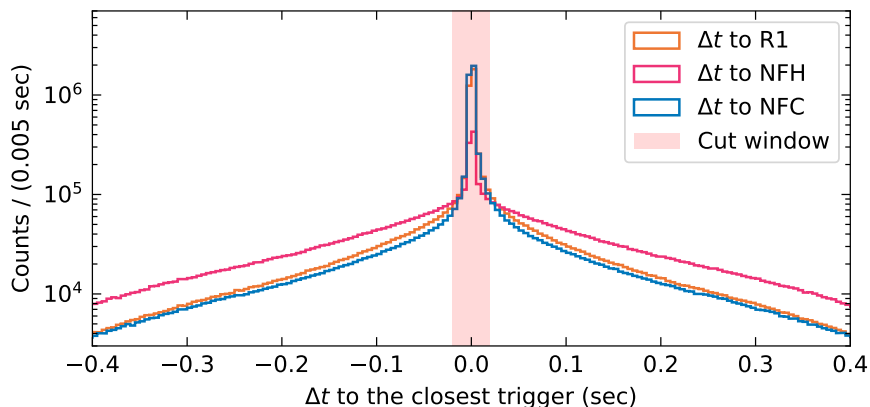


Figure 5.12: Distributions of time intervals between triggers in NFC and the closest triggers in the detector, specified in the legend. Positive (negative) values mean that the event in the NFC detector arrived after (before) the closest event in the other considered detector. Blue histogram shows event interarrival time in the NFC detector. Strong time correlations are observed as sharp peaks at zero. ± 20 ms window, excluded by the live-time selection, is shown in red.

Based on these distributions, we remove 20-ms-long intervals from the live time of all detectors before and after every event in any of the three detectors. This selection can be best understood with illustrations shown in Figure 5.13. An event at time t in a detector creates two dead-time intervals in this detector: $(t - 20\text{ ms}; t)$ and $(t; t + 20\text{ ms})$, as well as one dead-time interval in each of the other detectors: $(t - 20\text{ ms}; t + 20\text{ ms})$. In case of pile-up or coincident events, if the triggers are closer than 20 ms to each other, they both end

up being removed: each of them is in the dead-time windows of one another. We confirm with an MC simulation that removing both pulses in case of pile-up does not bias the rate measurement of random independent events. The width of the cut-out windows is optimized to reduce the rate of events, while preserving as much live time as possible. When applied separately from other live-time selection criteria, the selection described here removes 22.9% of the total live time of the science data.

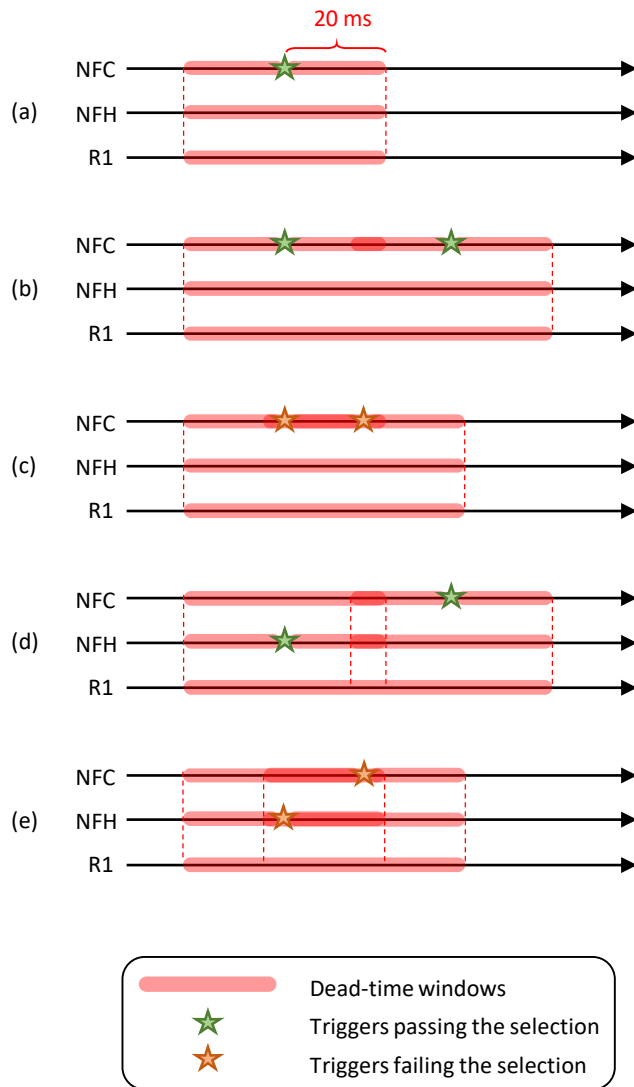


Figure 5.13: Illustration of the anti-coincidence live-time selection: (a) a single event, causing dead-time windows around it, as well as corresponding dead-time windows in other detectors; (b) two events in the same detector, both passing the live-time selection because the time interval between them is larger than 20 ms; (c) two close events in the same detectors failing the selection, since they are in the dead-time windows of one another; (d–e) same as (b–c), but the events are in two different detectors.

Science Data OFL Amplitude Spectrum after Live-time Selection

Figure 5.14 shows the rates in the NFC detector as a function of OFL amplitude after consecutively applied live-time selection criteria, with live-time reduction taken into account. Peaks corresponding to one, two and three $e^- h^+$ pairs are seen at around $0.14 \mu\text{A}$, $0.28 \mu\text{A}$ and $0.42 \mu\text{A}$, respectively. Peaks below the first $e^- h^+$ -pair peak are believed to be produced by charge leakage from the crystal sidewalls [127].

The mean baseline and temperature selection have almost no effect on the event rate. We apply them rather to remove events that could potentially have slightly misreconstructed energy due to an elevated baseline or due to a different temperature. The anti-coincidence selection reduces the event rate by a factor of 2 in the first $e^- h^+$ -pair peak, by an order of magnitude in the second $e^- h^+$ -pair peak, and by nearly two orders of magnitude at higher energies. The stronger reduction of the rate at higher energies is explained by the fact that most of the removed coincident events are burst events. Individual pulses in bursts overlap with each other and are thus misreconstructed as pulses of higher energy.

5.3.2 Laser Data Selection Criteria

Since we use TTL-triggered laser data for various checks and calculations pertinent to the science data, we want to apply the same selection criteria to the laser data as we apply to the science data. For various reasons, however, in some cases the exact match between the criteria cannot be achieved. We summarize the selection criteria applied to the laser data in this section.

First, we apply the mean baseline selection as done for the science data using random triggers. The temperature selection is not applied as it has no impact on the live time of laser data. This is due to the temperature stability during laser calibrations.

The first selection criterion that is different from the science data case is the anti-coincidence selection. Due to the fact that the laser was shining into the detector housing rather than on individual detectors, removing coincident events would remove almost all of the laser events. For that reason, we only apply a burst selection criterion to the laser data, that is an anti-coincidence of events in the same detector. In the science data, $\pm 20 \text{ ms}$ windows are removed around each trigger. However, the high frequency of the laser pulses (up to 200 Hz) does not allow us to remove such large windows from the laser data live time: the windows would intersect, thus removing all of the live time. Moreover, each laser pulse has two triggers associated with it: a TTL trigger and a GDF trigger. If we applied the anti-coincidence live-time selection in the same way as in the science data, the TTL and GDF triggers would remove one another, effectively removing all the laser pulses. For these reasons, we modify the selection criterion as follows: In each detector, we discard TTL triggers that have a GDF trigger in a $\pm 7 \text{ ms}$ window around it, excluding a $\pm 20 \mu\text{s}$ window in the middle. GDF triggers are allowed in the $\pm 20 \mu\text{s}$ windows around TTL triggers, as we

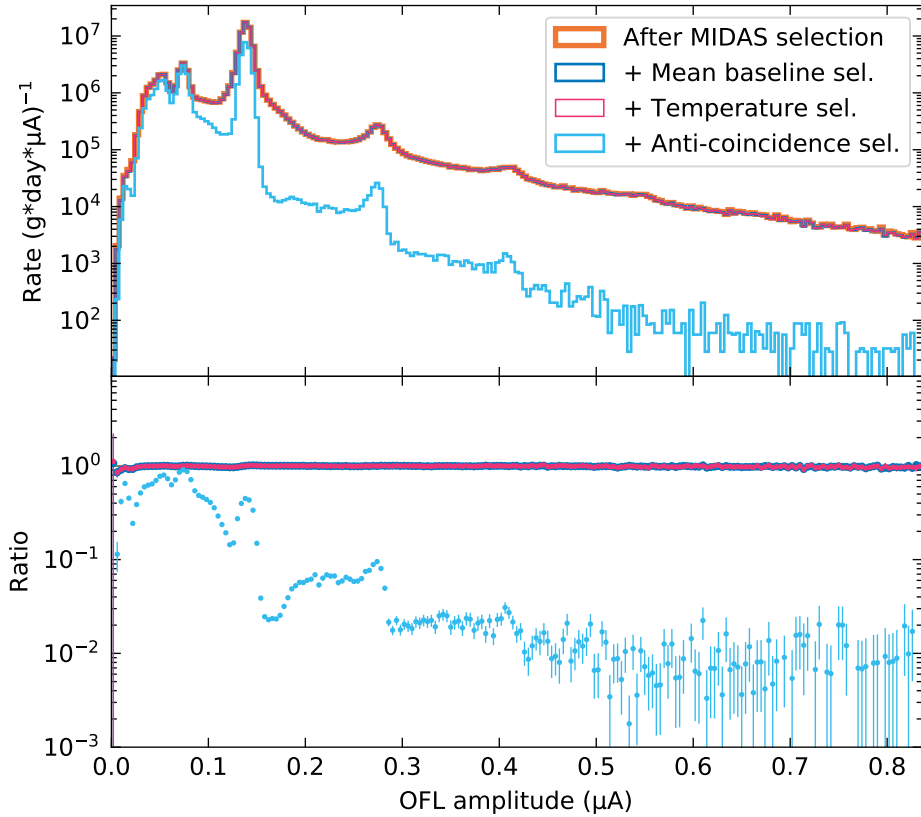


Figure 5.14: Event rates in NFC detector as a function of OFL energy estimator in the HVeV Run 3 science data with consecutively applied live-time selection criteria. Below: same rates divided by the rates after applying only the MIDAS intersecting trace selection. The anti-coincidence selection is the only selection that significantly affects the rate, reducing it by up to two orders of magnitude.

expect each laser pulse with the energy above the threshold to produce a GDF trigger.

The selection described above cleans up TTL-triggered data from burst events and pile-ups with pulses with energies higher than the triggering threshold. However, there are many laser pulses with subthreshold energies with no fully-amplified $e^- h^+$ pairs. When the time intervals between adjacent TTL triggers are shorter than half of the analysis trace length (which is the case for some of the laser series), a considerable fraction of TTL triggered events contain pile-ups of adjacent laser pulses. The pile-ups with subthreshold events survive the Δt selection described above and have slightly elevated OF fit χ^2 values, which is undesirable for the χ^2 selection studies (see Section 5.3.3). To better clean up laser data from such pile-up events, we apply the following additional criterion: the OF0 amplitudes of TTL-triggered events, adjacent to the TTL-triggered event under consideration, must be lower than 5 times the baseline resolution of the detector.

Figure 5.15 shows the OFL amplitude spectrum of the longest TTL-triggered laser data

set after consecutively applied selection criteria described in this section. Up to the fourth e^-h^+ -pair peaks are clearly visible in the spectrum, with the fifth having a very limited number of events. This limits the energy range in which a reliable calibration can be obtained, so we define the energy ROI of the Run 3 analysis to be within the first four e^-h^+ -pair peaks. More precisely, the energy ROI is set to 50–440 eV, which is motivated by the positions and widths of the e^-h^+ -pair peaks in the DM signal models (see Section 5.4.3).

The shape of this spectrum is strikingly different from the shape of the laser data spectrum in HVeV Run 2 (see Figure 4.5): in Run 3, the distribution of events between the peaks is not flat. This is caused by the photons hitting the sidewalls of the detector in Run 3, creating charge carrier that have a high probability to be trapped on the sidewall, thus modifying the shape of the distribution between the peaks.

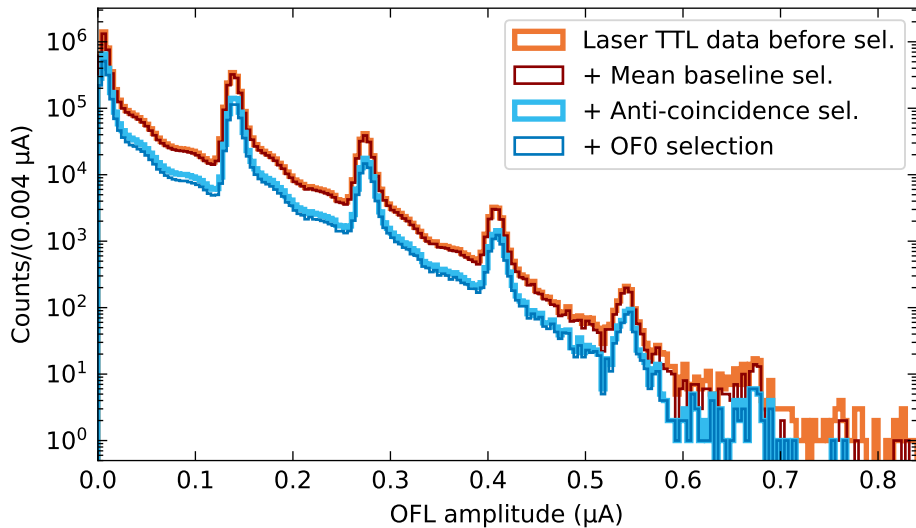


Figure 5.15: Event counts in NFC detector as a function of OFL energy estimator in the longest laser data set with consecutively applied laser data-selection criteria. The anti-coincidence selection has the strongest effect.

5.3.3 Data-Quality Selection Criteria

To develop data-quality selection criteria we use the laser data cleaned up as described in the previous section. We consider such laser events to be a proxy for DM events, so we use them to calculate what fraction of DM events a certain data-quality selection criterion would remove, or what we call the data-quality selection efficiency. After defining the data-quality selection criteria described in this section, we apply them to both the science and the laser data.

OFL χ^2 Selection

The OFL χ^2 value is a measure of goodness of OFL fits, so the higher the OFL χ^2 value is, the less confident we are in the accuracy of the OFL energy estimator. For that reason, we remove events with high χ^2 values and account for their lost fraction by calculating the selection efficiency. We define the maximum allowed OFL χ^2 values in the following way:

- in each of the quantized $e^- h^+$ -pair peaks of the TTL-triggered OFL energy spectrum an empirical CDF of OFL χ^2 values is built and the value at which it reaches a 95% point is determined;
- the found OFL χ^2 values are fitted with a power law,

$$y(E) = aE^n + b, \quad (5.1)$$

where $y(E)$ is the 95% OFL χ^2 value for each peak, E is the OFL amplitude corresponding to the peak, and a , b and n are free fit parameters (see Figure 5.16).

Equation 5.1 defines the maximum allowed OFL χ^2 values at each energy, measured in units of OFL amplitude. By construction, it should retain approximately 95% of the DM events, which we confirm by an energy-independent fit to the fraction of cleaned-up laser data events, preserved after applying this data-quality selection, as shown in Figure 5.17. The fit is performed in the energy ROI of 50–440 eV.

$\Delta\chi^2$ Selection

The main reason for events in the HVeV Run 3 data to have a high OFL χ^2 value is the pile-up of closely lying pulses. Naively, one would assume that such events are removed by the anti-coincidence selection; however, when the pulses are closer to each other than the triggering time resolution, they produce only one trigger, and therefore they are not removed by the anti-coincidence selection. Such a pile-up of pulses is misinterpreted as one pulse with combined energy. For example, a close pile-up of two $1-e^- h^+$ -pair events is reconstructed as one event with energy close to the energy of one $2-e^- h^+$ -pair event. This effect artificially increases the rate of multi- $e^- h^+$ -pair events, thus affecting the reach of the experiment to the DM masses that produce more than 1 $e^- h^+$ pair. Therefore, identification and removal of the pile-up of closely lying pulses is crucial for the Run 3 analysis.

Although the OFL χ^2 selection is capable of removing most pile-up events, a selection based on the difference between the χ^2 values of the two-pulse (OFP) and one-pulse (OFL) fits is better suited for rejecting pile-up of closely lying pulses. We define an RQ to be used for the pile-up rejection as follows:

$$\Delta\chi^2 = \chi_{\text{OFL}}^2 - \chi_{\text{OFP}}^2, \quad (5.2)$$

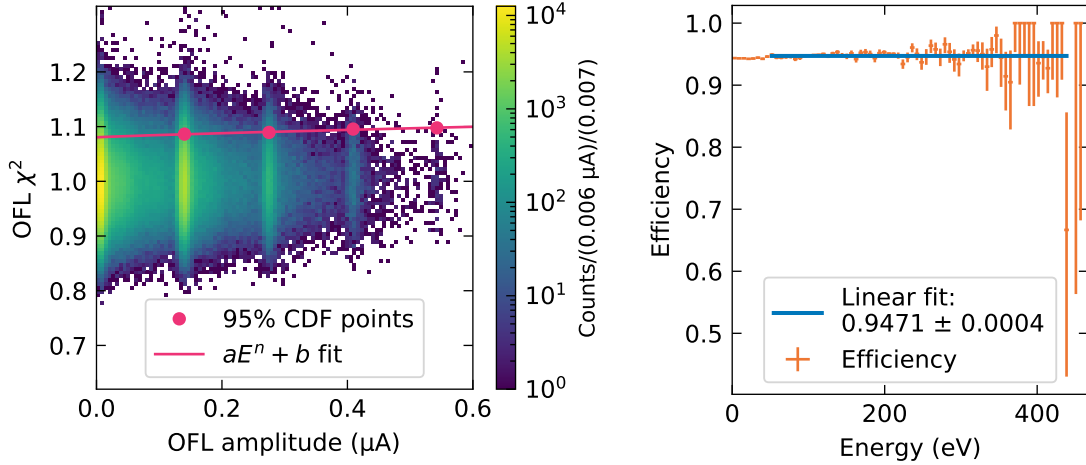


Figure 5.16: OFL χ^2 versus OFL amplitude distribution in laser data, with 95% points in Cumulative Distribution Functions (CDFs) of events within $e^- h^+$ -pair peaks (round markers), fitted with Equation 5.1. Courtesy of Corey Bathurst.

Figure 5.17: Efficiency of the χ^2 selection in energy bins with an energy-independent fit in the energy Region of Interest of 50–440 eV. Courtesy of Corey Bathurst.

where χ^2_{OFL} and χ^2_{OFP} are the OFL and OFP fit χ^2 values respectively. We follow the same steps as in the OFL χ^2 case to define the maximum allowed values of $\Delta\chi^2$, which retains 95% of the laser events, used as a proxy for the DM events (see Figures 5.18–5.19).

Using a simulation with artificially injected closely-lying pulses, we determine that the selection based on the OFL χ^2 has a 50% efficiency at removing pile-up events with pulses separated by 13 time samples (20.8 μ s), while the $\Delta\chi^2$ selection efficiency drops to 50% when the pulses are separated by as little as 7 time samples (11.2 μ s, see Figure 5.20). Taking into account the very steep rise in the distribution of event interarrival times near 0 (Figure 5.12), an almost two-times better time resolution of the pile-up rejection algorithm is a significant improvement.

Combined Data-quality Selection Efficiency

Figure 5.21 shows the combined efficiency of the data-quality selection criteria described in this section. It is calculated as an energy-independent fit to the fraction of cleaned-up laser events (as described in Section 5.3.2), preserved after applying the data-quality selection criteria. The combined efficiency is $(90.05 \pm 0.05)\%$.

OFL Spectra after Data-quality Selection

Figure 5.22 shows event rates observed in the NFC detector after consecutively applied live-time and data-quality selection criteria, taking into account live-time reduction and data-

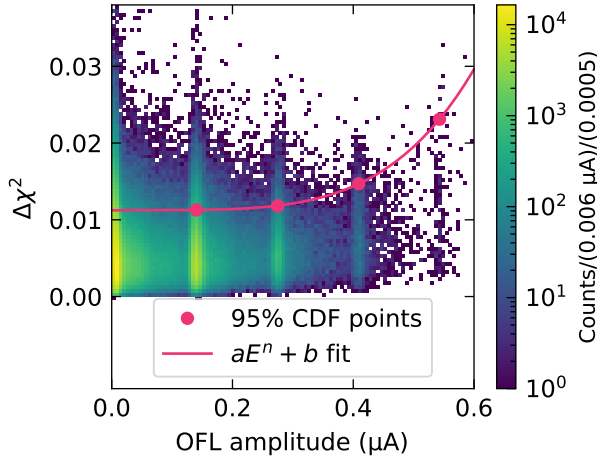


Figure 5.18: $\Delta\chi^2$ versus OFL amplitude distribution in laser data, with 95% points in Cumulative Distribution Functions (CDFs) of events within $e^- h^+$ -pair peaks (round markers), fitted with Equation 5.1. $\Delta\chi^2$ is defined in Equation 5.2. Courtesy of Corey Bathurst.

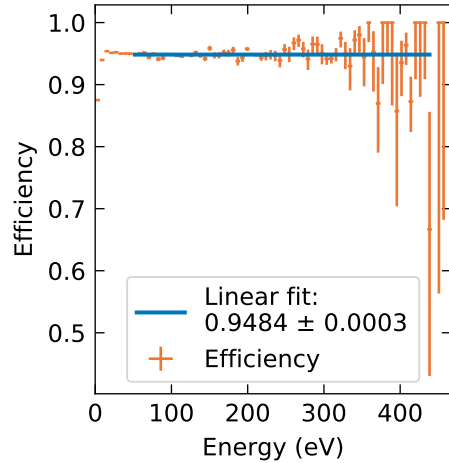


Figure 5.19: Efficiency of the $\Delta\chi^2$ selection in energy bins with an energy-independent fit in the energy Region of Interest of 50–440 eV. Courtesy of Corey Bathurst.

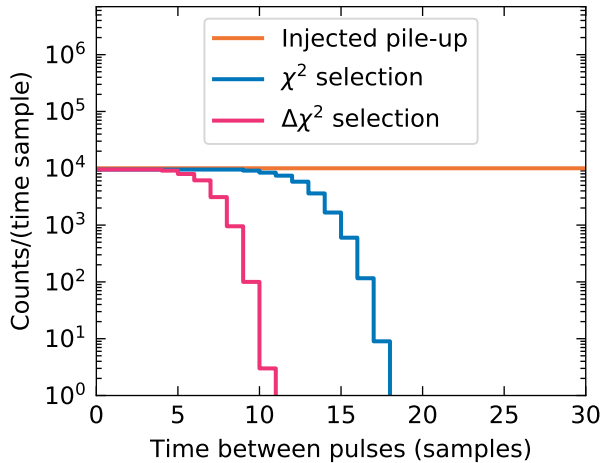


Figure 5.20: χ^2 and $\Delta\chi^2$ selection performance test. Distributions of pulse separation time is shown. Pulses in pile-up with uniformly distributed pulse separation time are injected into random noise traces (orange), then the χ^2 (blue) or $\Delta\chi^2$ (pink) selections are applied. Courtesy of Corey Bathurst.

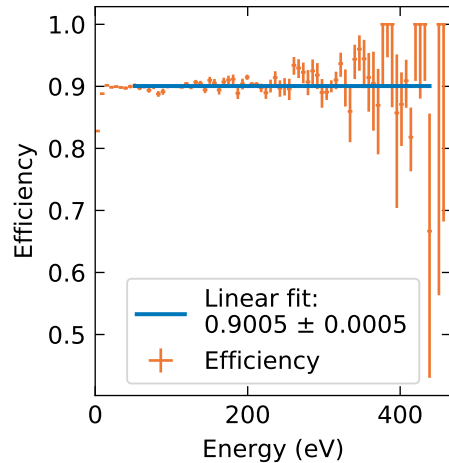


Figure 5.21: Combined efficiency of the data-quality selection, calculated using laser data with an energy-independent fit in the energy Region of Interest of 50–440 eV. Courtesy of Corey Bathurst.

quality selection efficiency. The χ^2 and $\Delta\chi^2$ selection mostly removes events in the regions between the $e^- h^+$ -pair peaks, suggesting that these regions have a contribution from pile-up events, misreconstructed as one-pulse events. After all the selection criteria applied, the first three $e^- h^+$ -pair peaks are clearly visible in the spectrum, with a flat background at higher energies.

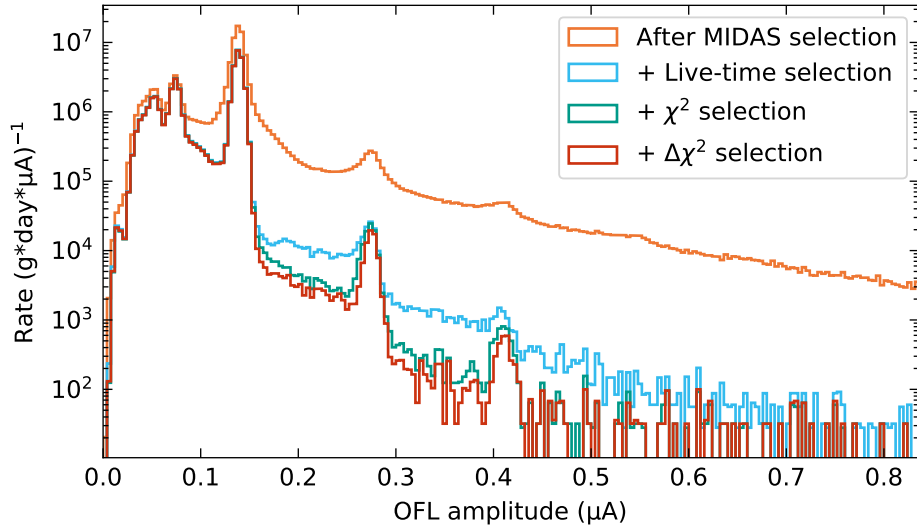


Figure 5.22: Event rates in NFC detector in the HVeV Run 3 science data with consecutively applied live-time and data-quality selection criteria.

Figure 5.23 shows the OFL amplitude spectrum of the longest TTL-triggered laser data set after consecutively applied laser-specific and common to both the laser and the science data data-quality selection criteria. The χ^2 and $\Delta\chi^2$ selection does not remove a significant fraction of laser events, since unlike the science data the laser data are not dominated by the burst events.

5.3.4 Energy Calibration

We use the TTL-triggered laser data with the selection criteria described in Sections 5.3.2 and 5.3.3 to calibrate the OFL energy estimator to the phonon energy. As in the previous run, we rely on the locations of the quantized peaks in the laser data, defined by Equation 4.7 in Section 4.4. In this equation, the ΔE term describing the shift of the peaks from their expected positions is introduced. We named direct absorption of photons in the QETs and trapping on the crystal face as the possible reasons for this shift in the previous run. In the current run, due to a different configuration of the laser setup, there is an additional effect to consider, namely the trapping on the sidewalls. As in the case of effects named in the previous run, the amount of energy generated by charge carriers trapped on the sidewalls is independent from the number of $e^- h^+$ pairs producing full NTL amplification. Moreover,

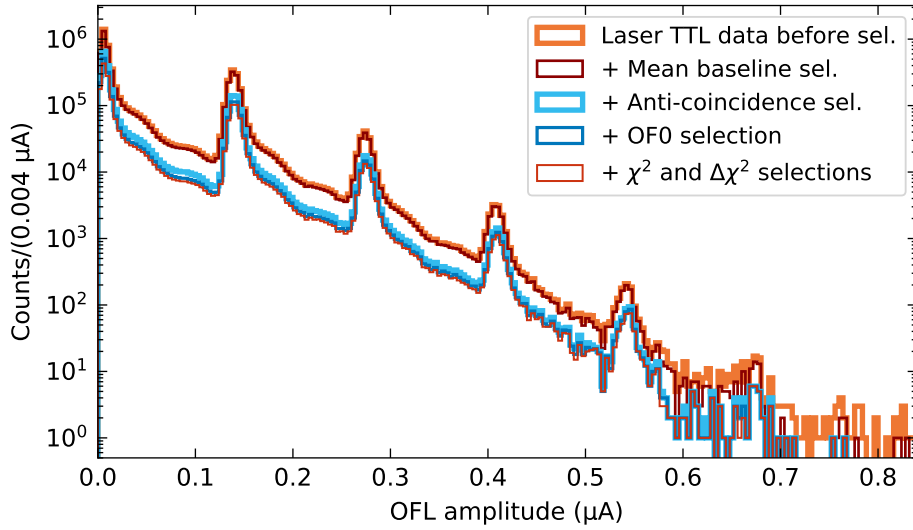


Figure 5.23: Event counts in NFC detector in the longest TTL-triggered laser data set with consecutively applied selection criteria.

the distortion of the peak shapes in the spectrum caused by the sidewall trapping effect is also independent from the peak number. Due to these reasons, we assume that the sidewall trapping effect is taken into account by the ΔE term.

To find locations of the $e^- h^+$ -pair peaks in the OFL amplitude spectrum of the laser data, we rely on Gaussian fits. Since the aforementioned additional effects are independent from the peak number, we assume that the non-Gaussianity introduced by the additional effects shifts the Gaussian fit results by the same value in each peak and is therefore taken into account by the offset ΔE . To minimize the effect of non-Gaussianity, the fits are performed in narrow regions, enclosing only the top 50% tips of the peaks.

In the previous run, to account for the saturation effect a second-degree polynomial without the free term was used as the calibration function, see Equation 4.8. In the current run we observed that the second degree polynomial does not accurately fit the peak positions, therefore we use a third-degree polynomial as the calibration relation between the OFL amplitude A_{OFL} and the phonon energy E :

$$E = aA_{\text{OFL}} + bA_{\text{OFL}}^2 + cA_{\text{OFL}}^3, \quad (5.3)$$

where a , b and c are calibration parameters.

One last effect to take into account before fitting OFL peak locations to the third-degree polynomial is what we call the OFL noise latching effect. When fitting a low-energy pulse, OFL tends to overestimate the pulse amplitude by shifting the template in the allowed time window to find the highest noise fluctuation. The OF0 energy estimator does not have this effect, since there is no allowed template shift in this OF variant. For pulses above 50 eV,

that is within our energy ROI, this effect is insignificant: $A_{\text{OFL}}/A_{\text{OF0}} \leq 1.0006$. At lower energies, at the 0-th e^-h^+ -pair peak in particular, this effect is more pronounced. To avoid adding this effect into the calibration, we calculate where the OFL 0-th peak would be located ($A_{\text{OFL},0}$) if it were not affected by the noise latching effect. For that we use the locations of the peaks in the OF0 spectrum:

$$A_{\text{OFL},0} \stackrel{\text{def}}{=} A_{\text{OF0},0} \frac{A_{\text{OFL},1}}{A_{\text{OF0},1}}, \quad (5.4)$$

where $A_{\text{OF0},0}$ and $A_{\text{OF0},1}$ are the locations of the zeroth and first e^-h^+ -pair peaks in the OF0 amplitude spectrum, and $A_{\text{OFL},1}$ is the location of the first e^-h^+ -pair peak in the OFL amplitude spectrum.

We find the ΔE term in the same way as in the previous analysis, using the OF0 energy estimator to mitigate the noise latching effect and neglecting the calibration non-linearity:

$$\Delta E = A_{\text{OF0},0} \frac{eV_{\text{bias}} + E_\gamma}{A_{\text{OF0},1} - A_{\text{OF0},0}}. \quad (5.5)$$

We then fit $A_{\text{OFL},n}$ values, with $A_{\text{OFL},0}$ defined in Equation 5.4 and the rest of them being locations of the OFL e^-h^+ -pair peaks, to the energies as defined by Equations 4.7 using the polynomial in Equation 5.3. We use three different laser data sets with different laser intensities, which causes them to have different offsets ΔE , calculated individually for each data set. The polynomial fit is performed simultaneously to the $A_{\text{OFL},n}$ values from all three data sets. Figure 5.24 shows the fit results with the fit statistical uncertainty shown by the green band.

It is possible that the calibration parameters vary from day to day. One of the effects that can cause it is the bias voltage instability caused, for example, by the charge build-up on the crystal faces. We include the daily variation of the calibration as a systematic uncertainty, shown in Figure 5.24 by the orange band. Its magnitude is propagated from the day-to-day instability of the position of the one- e^-h^+ -pair peak in the science data, as shown in Figure 5.25: each data point on the day-to-day first peak position plot is used to generate an ensemble of toy experiments with the peak positions generated from a Gaussian distribution around that point; the toy experiments from each point are then combined to create an empirical model for the peak position distribution, and a band covering 68% of the data in the model is used as a systematic uncertainty. The total calibration uncertainty is calculated by combining in quadrature the statistical uncertainty of the fit and the systematic uncertainty from the day-to-day variations. The uncertainties introduced by the non-Gaussianity of the e^-h^+ -pair peak, the noise latching effect and the ΔE calculation procedures were estimated to be subdominant.

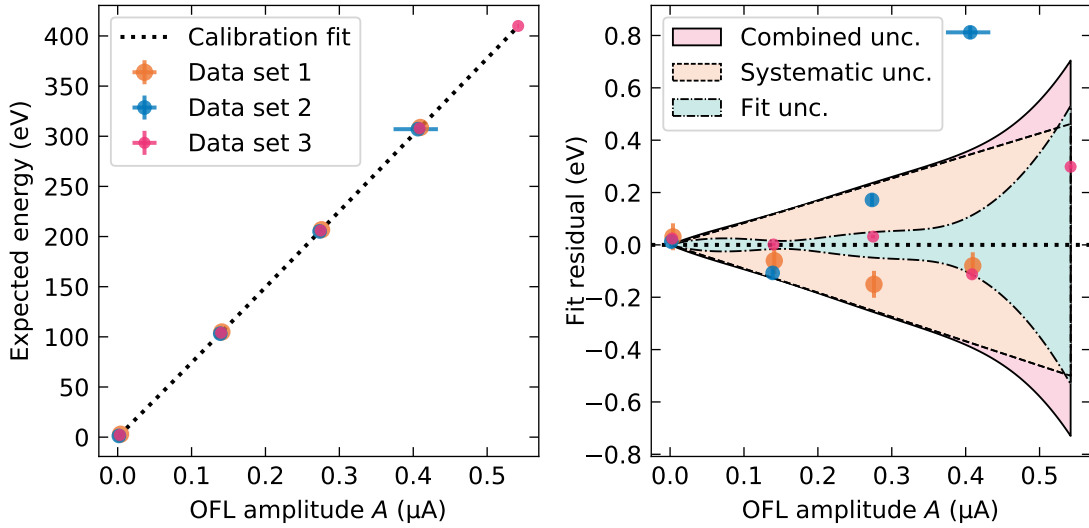


Figure 5.24: (Left) positions of the e^-h^+ -pair peaks in the OFL spectra of 3 laser data sets (x-axis) and their corresponding expected energy values (y-axis), fitted with a third-degree polynomial (Equation 5.3). X-axis uncertainties are statistical uncertainties of the peak position fits. Y-axis uncertainties are statistical uncertainties of the peak offsets ΔE . (Right) fit residuals for the 3 data sets (round markers with uncertainties as before), statistical uncertainty of the polynomial fit (green area), systematic uncertainty derived from the day-to-day gain variation (orange area) and the combined calibration uncertainty (pink area). Courtesy of Taylor Aralis.

5.3.5 Energy Spectrum Used in the Limit Setting

With defined data selection criteria and developed energy calibration, we obtain an experimentally observed energy spectrum that we use to set the DM limits. As discussed in Section 5.5.3, we split the data into two parts: 90% of randomly selected data is used for the limit setting, while the remaining 10% is used for making unbiased decisions about the limit-setting regions. Figure 5.26 shows event counts as a function of energy for both parts of the science data. These spectra are not divided by the data-quality selection efficiency. Instead, the efficiency is taken into account in the next section as a part of the detector response to DM signals. The exposure of the 10% and 90% of the science data is 0.852 g-days and 7.63 g-days, respectively.

5.4 Dark Matter Signal Models

With the measured energy spectrum cleaned up and calibrated, we move to the DM signal models — the energy spectra expected to be caused by DM interactions in the detector under the assumption that the entire DM halo of our galaxy consists of a considered DM candidate. In this section, we reiterate the DM candidates considered in this analysis, providing references

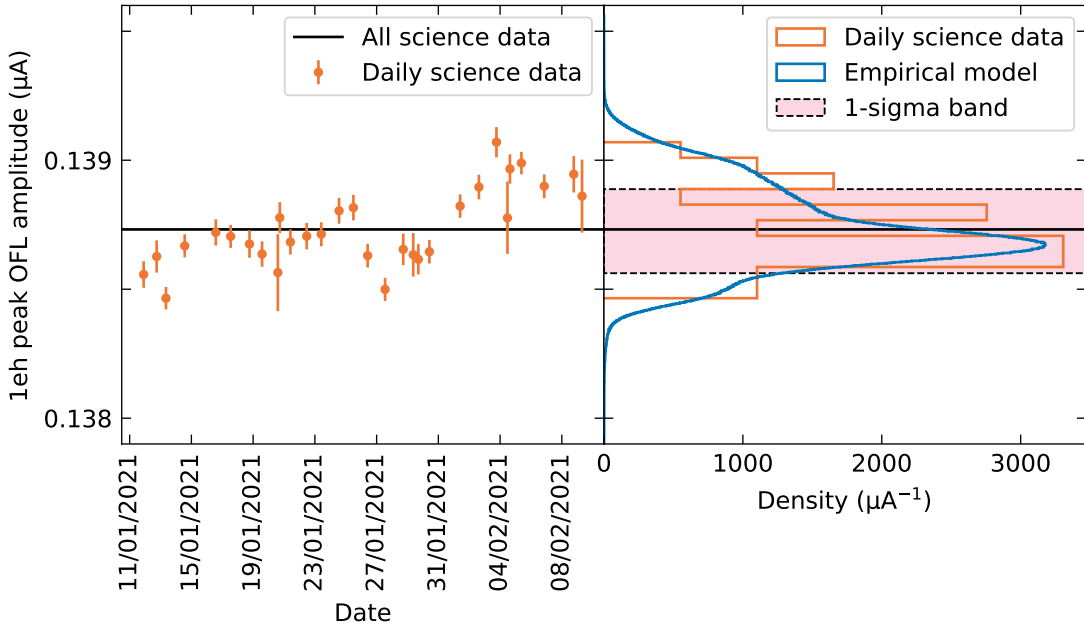


Figure 5.25: (Left) Positions of the first $e^- h^+$ -pair peak in each of the science data sets with statistical fit uncertainties (round markers) and the position of the first $e^- h^+$ -pair peak in all the science data combined (gray horizontal line). (Right) Distribution of the positions of the first $e^- h^+$ -pair peaks in science data sets (orange), its empirical model (blue) and a band, enclosing 68% of the model distribution (pink). Courtesy of Taylor Aralis.

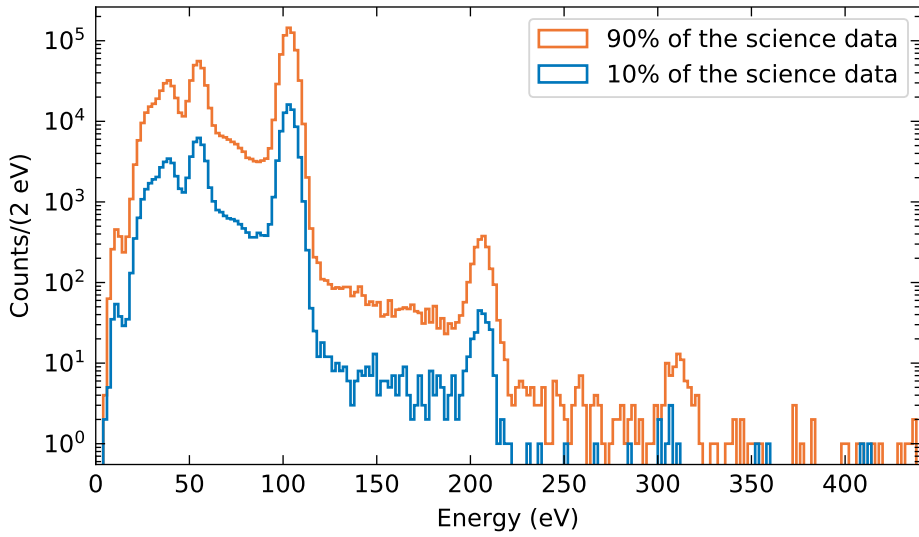


Figure 5.26: Event counts in 90% and 10% of the science data after the live-time and data-quality selections as functions of calibrated energy. Not corrected by the data-quality selection or trigger efficiency.

to their predicted interaction rates, and apply the detector response effects to their energy spectra.

5.4.1 Theoretical Interaction Energy Spectra

The first signal model that we consider in this analysis is the LDM-electron recoil. The differential rate is given in Section 1.2.2 by Equation 1.8. Two DM form factors are considered, as shown in Equation 1.11: $F_{\text{DM}} = 1$ corresponding to the heavy mediator case, and $F_{\text{DM}} \propto 1/q^2$ corresponding to the ultra-light mediator case. The crystal form factor is calculated with the QEDark model [42, 44]. Following an agreement between SENSEI, DAMIC and SuperCDMS collaborations, we use the DM halo parameters recommended in Ref. [40]: the asymptotic value of the Maxwellian velocity distribution $v_0 = 238 \text{ km/s}$, the galactic escape velocity $v_{\text{esc}} = 544 \text{ km/s}$, the local DM mass density $\rho_{\text{DM}} = 0.3 \text{ GeV}/(c^2 \cdot \text{cm}^3)$, and the average Earth velocity with respect to the DM halo $v_E = 253.7 \text{ km/s}$.

The next signal model is the DP absorption. The interaction rate is given by Equation 1.12 in Section 1.2.3, with the energy spectrum represented by a delta function at the energy equal to the DP mass. Energy-dependent real and imaginary parts of the photoelectric absorption σ_1 and σ_2 are taken from Ref. [105].

The last model considered in this analysis is the ALP absorption, with the rate given by Equation 1.14 in Section 1.2.4. The spectrum is again a delta function at the energy equal to the ALP mass.

5.4.2 Detector Response Model

We utilize the detector response model derived in Section 3.1.3 and given by Equation 3.20. We repeat it here for convenience, specifying the type of events as bulk events:

$$\frac{dR}{dE}(E) = \sum_{i=0}^{\infty} \left(\int_0^{\infty} p_{\text{eh}}(i | E_{\text{dep}}) F_{\text{bulk}}^{(i)} \left(\frac{E - E_{\text{dep}}}{eV_{\text{bias}}} \right) \frac{dR}{dE_{\text{dep}}}(E_{\text{dep}}) dE_{\text{dep}} \right) * G(E | \sigma). \quad (5.6)$$

Here, dR/dE is the differential rate of energy that is expected to be measured by the detector if the differential rate of energy deposited in the bulk of the detector is given by dR/dE_{dep} . The dR/dE_{dep} are as explained in Section 5.4.1. V_{bias} is the voltage applied across the crystal, e is the elementary charge. We discuss the rest of the components of this equation in the following paragraphs.

The ionization model is represented by the $p_{\text{eh}}(i | E_{\text{dep}})$ term, defined as the probability to produce $i e^- h^+$ pairs in an event with the deposited energy E_{dep} . We use the ionization model introduced in Ref. [104] and interpolated as described in Section 2.1.1 to obtain the ionization probability functions corresponding to the Si band gap value used in the current analysis, 1.131 eV [105].

$F_{\text{bulk}}^{(i)}$ is the PDF of NTL amplification for bulk events with i e^-h^+ pairs initially produced by the incoming particle. The function is defined by the bulk CTII model, introduced in Chapter 3.

In the previous HVeV runs, we used laser data to measure bulk CTII probabilities. The laser was focused on the center of the top surface of the crystal, producing charge carriers far away from the sidewall. Traversing the crystal in a strong electric field, the charge carriers diffuse in the transverse plane only on the micrometer scale [128], which prevents them from reaching the sidewall of the crystal and makes them a good probe for the bulk CTII effects. In Run 3, however, the laser was pointed to the sidewalls of the detectors. In such configuration, laser hits produce e^-h^+ pairs very close to the crystal sidewall, making it possible for them to get trapped on the sidewall while traversing the crystal in the electric field. This effect prevents us from measuring bulk CTII probabilities with the Run 3 data.

The bulk CTII probabilities are defined by the concentration of impurities in the crystal. Given that the NFC detector used in Run 3 is produced from the same Si wafer as the Run 2 detector, it is reasonable to assume that it contains the same amount of impurities, and therefore its CTII properties are the same. For this reason, we use the CTII probabilities obtained with HVeV Run 2 data: $12.8 \pm 1.5\%$ CT and $1.6^{+1.8}_{-1.6}\%$ II [114]. We did not measure these probabilities for different charge types and assume that they are the same for electrons and holes. Thus, the probabilities for CT of an electron or a hole are $p_{CTe} = p_{CTh} = 0.128 \pm 0.015$. For the II processes, we divide the probability measured in Run 2 by two, to take into account that a charge of a certain type can participate in two different types of the II processes: it can create a charge of the same or of the opposite sign. Therefore, the II probabilities used in Run 3 are defined as $p_{IIee} = p_{IIeh} = p_{IIhe} = p_{IIhh} = 0.008^{+0.009}_{-0.008}$, where indices show the type of the II process, as explained in Chapter 3. We then use Equation 3.2 to convert these probabilities into characteristic lengths of the individual CTII processes and calculate the $F_{\text{bulk}}^{(i)}$ functions with these lengths.

The remaining term in Equation 5.6 is $G(E | \sigma)$ — a Gaussian with the width σ , representing the detector energy resolution. It was observed that the resolution grows with energy. However, we could not obtain a reliable energy-dependent model, therefore we use an energy-independent model with high systematic uncertainty, as discussed below.

Measuring widths of the e^-h^+ -pair peaks in the energy spectrum is a natural choice for measuring energy resolution. However, resolution is not the only contribution to the peak width. Variance of event energies is an additional contribution that makes the peaks wider. Since we do not have a background model in this analysis, we cannot quantify and subtract the variance of energy of background events from the peak widths in science data. In the laser data, on the other hand, there is no variance in deposited energy in events belonging to a certain peak in an idealized scenario: n -th peak corresponds to n e^-h^+ pairs which corresponds to n monoenergetic photons hitting the detector. However, there are other effects that widen the e^-h^+ -pair peaks in the laser data, with the sidewall trapping being

the most pronounced. Quantifying contribution of the sidewall trapping to the peak widths is not trivial. Consequently, we use the peak widths measured in the laser and science data only as the upper limits on the energy resolution.

Figure 5.27 shows the widths of the $e^- h^+$ -pair peaks in the laser and science data, obtained with Gaussian fits. We do not attempt to model the resolution energy dependence using these data. Instead, we rely on a simple energy-independent model with a systematic uncertainty large enough to cover the energy dependence in the energy ROI, that is up to the fourth $e^- h^+$ -pair peak. As the upper boundary of the uncertainty band we use the highest measured peak width — the width of the fourth peak in the laser data, 5.49 eV. As the lower boundary we use the baseline resolution measured with Gaussian fits to the reconstructed energy of randomly triggered events without energy depositions in the detector. We measured a slightly larger value of the baseline resolution in the laser data, which we attribute to the contamination of the randomly triggered events with the low-energy laser events, affected by the sidewall effect. Therefore, we use the baseline resolution measured with the science data, 3.03 eV, as the lower bound of the uncertainty band. For the nominal value of the resolution we use the mean value of the lower and upper bounds of the systematic uncertainty band, 4.26 eV. The high systematic uncertainty assigned to the resolution does not result in a high uncertainty of the DM limit, as we show in Section 5.5.4.

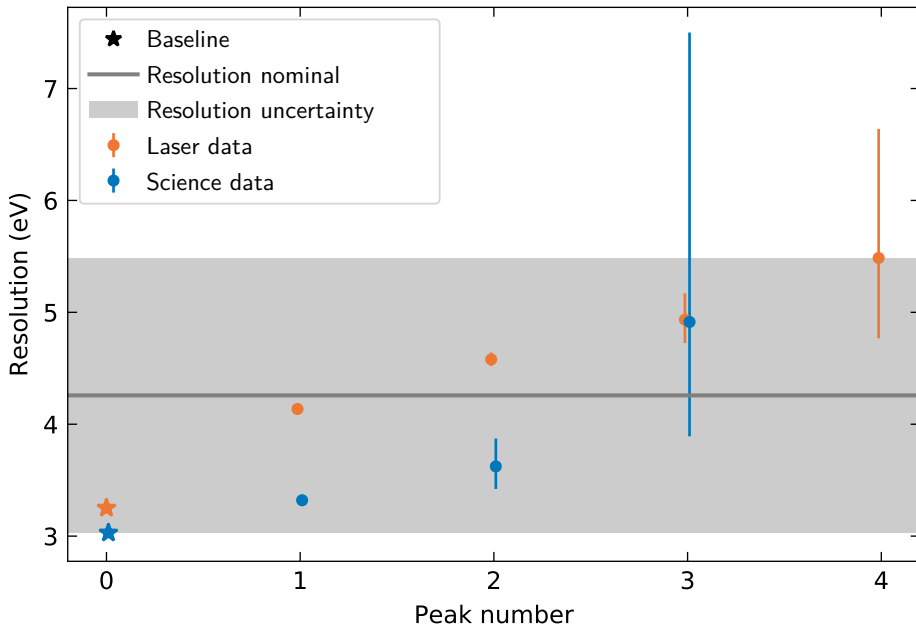


Figure 5.27: Peak widths in laser (orange) and science data (blue) and the energy-independent resolution model (dark gray line) used in the limit setting with its systematic uncertainty (gray band). The baseline resolutions measured with laser and science data are shown with stars.

5.4.3 Expected Dark Matter Counts in the Experiment

We apply the detector response model described in Section 5.4.2 to the theoretical DM interaction differential rates described in Section 5.4.1. Figure 5.28 shows the resulting DM signal models for a range of DM masses considered in the current analysis. The models are DM-electron recoil with heavy and ultra-light mediator, DP absorption and ALP absorption. Each model is shown with a fixed value of the signal strength parameter: electron recoil cross section $\sigma = 10^{-33} \text{ cm}^2$, DP kinetic mixing $\varepsilon = 10^{-12}$ and axio-electric coupling $g_{ae} = 10^{-8}$. In addition to the detector response effects described in Section 5.4.2, the signal models are scaled by the experiment exposure of 7.26 g-days and the energy-independent data-quality selection efficiency from Section 5.3.3. The experimentally measured spectrum derived in Section 5.3 is shown in gray for comparison.

For the DM-electron recoils, as the DM mass increases, the expected DM number density decreases, leading to lower expected DM rates at higher masses. At DM masses below $\sim 1 \text{ MeV}/c^2$, the probability of producing recoil energies sufficient for the ionization of at least one e^-h^+ pair is too low, again leading to a reduction of the expected event rate in the experiment. So the reach of the experiment with respect to the DM masses is limited to the $\sim 1 \text{ MeV}/c^2$ – $10 \text{ GeV}/c^2$ interval.

The absorption models have a hard lower DM mass boundary equal to the Si band gap energy of $1.131 \text{ eV}/c^2$: masses below this energy cannot be probed by the experiment since such particles do not have enough energy to produce ionization in the crystal. As the DM mass goes from $\sim 1 \text{ eV}/c^2$ to $\sim 10 \text{ eV}/c^2$, although the expected DM number density decreases, the expected event rate increases due to the rapidly growing photoelectric cross section in this energy region [105]. The number of produced e^-h^+ pairs grows with the DM mass and at the mass above $\sim 25 \text{ eV}/c^2$ the probability of producing ≤ 4 e^-h^+ pairs becomes too small (see Figure 2.1). With the energy ROI defined to be up to the fourth e^-h^+ -pair peak, the DP and ALP masses above $\sim 25 \text{ eV}/c^2$ are not probed in this analysis.

5.5 Dark Matter Limits

As in the analysis described in Chapter 4, without a background model we cannot perform a DM search with a discovery potential. However, with the measured energy spectrum and the expected DM counts for various DM models at hand, we proceed to setting exclusion limits on the electron recoil cross section, as well as on the DP kinetic mixing and ALP electron coupling.

In the DM nuclear recoil search described in Chapter 4 we applied the OI method which relies on the differences between the shapes of the signal model and the observed spectrum to find an energy region, providing the best constraint on the DM signal model strength. The DM nuclear recoil spectrum is rather smooth and its shape is very stable under the

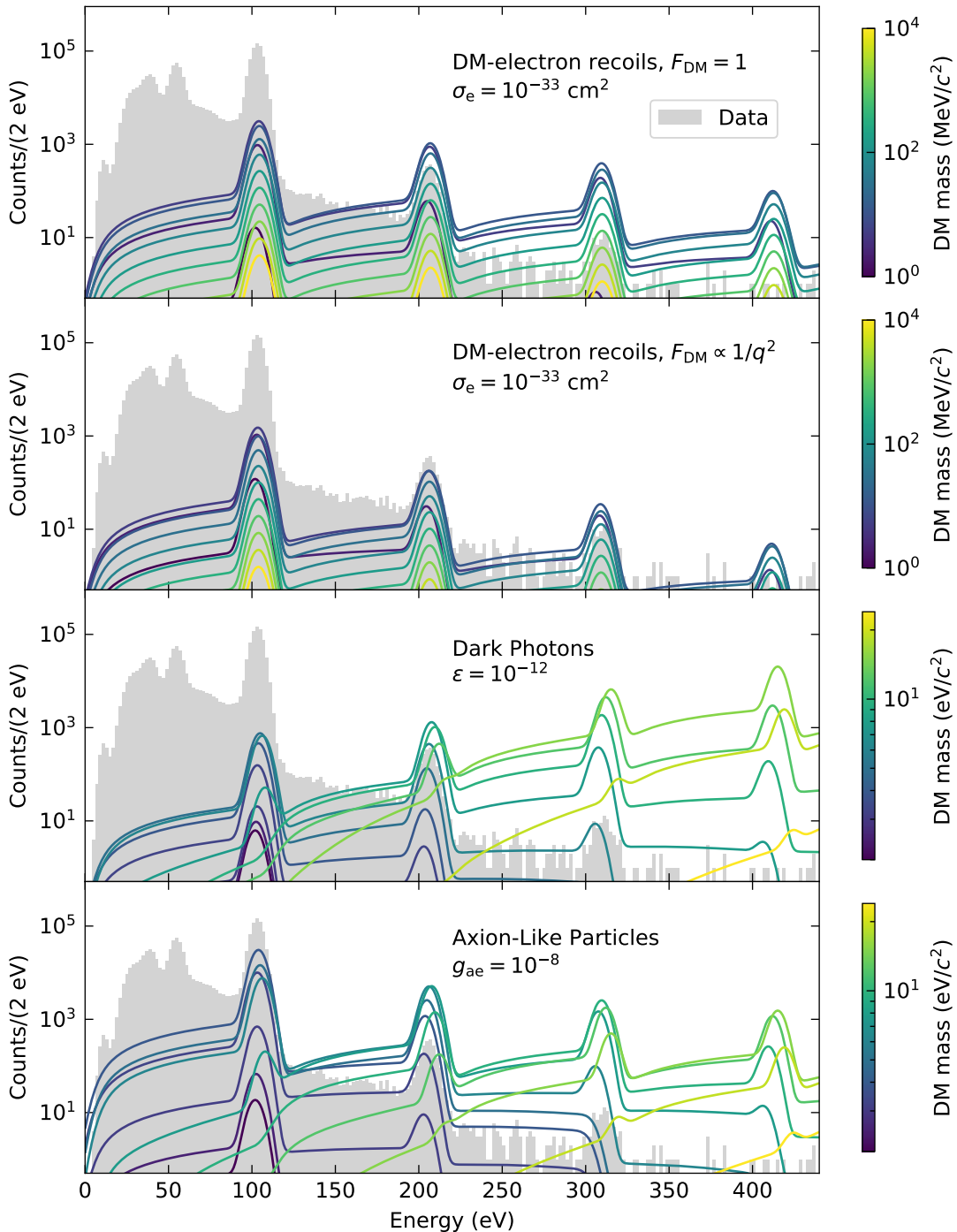


Figure 5.28: Measured energy spectrum (gray) with Dark Matter (DM) signal models for various DM masses with the detector response model applied (colored lines). From top to bottom, the DM models are: DM-electron recoil with form-factor $F_{\text{DM}} = 1$; DM-electron recoil with form-factor $F_{\text{DM}} \propto 1/q^2$; Dark Photon (DP) absorption; Axion-Like Particle (ALP) absorption. The corresponding signal strength values are specified in the figure.

fluctuations of detector response parameters within their systematic uncertainties. The signal models considered in the current chapter, however, have quantized peaks with their widths and positions directly affected by the detector resolution and calibration. A small inaccuracy in the resolution or calibration introduces a non-physical mismatch between the signal model and the observed spectrum shape near the e^-h^+ -pair peaks, which tends to be exploited by the OI method to set an erroneously strong limit [114].

To resolve this issue, we define multiple limit-setting energy regions, each fully enclosing one quantized peak in the signal models. We then calculate exclusion limits in each of these windows using the Poisson counting method described in Section 5.5.1 and combine them into one limit for each DM model and mass as described in Section 5.5.2. Section 5.5.3 describes how the limit-setting windows are defined and which of them are selected for each of the DM model and mass. Section 5.5.4 shows the resulting DM signal strength upper bound limits. Lastly, in Section 5.5.5 we investigate how the shielding effect influences the DM exclusion region.

5.5.1 Poisson Counting Method

For random and independent events, such as DM interactions, the number of observed signal events N in a predefined energy region (E_1, E_2) in an experiment with exposure T follows the Poisson distribution with the mean value $\lambda(s)$ defined by the signal model with the signal strength s :

$$f_N(N | s) = \text{Pois}(N | \lambda(s)), \quad (5.7)$$

$$\lambda(s) = T \int_{E_1}^{E_2} \text{eff}(E) \frac{dR(E | s)}{dE} dE. \quad (5.8)$$

The differential signal model rate, with the detector response effects taken into account and with the signal strength s serving as a parameter, is denoted by $dR(E | s)/dE$. We also take into account the efficiency of the trigger and data selection $\text{eff}(E)$ by folding it into the integral. Note that we use a signal-only hypothesis when defining the distribution of N . If we knew all the background components that contribute to N , we could exclude a range of signal strengths s with some confidence c by obtaining N_{meas} in an experiment. However, without the background model, we can only place a c confidence upper bound on the signal strength s_c . To do this, we find such a value of the signal strength s_c for which the CDF of N , $F_N(N | s_c)$, is equal to $1 - c$ when evaluated at N_{meas} :

$$F_N(N | s) = \sum_{i=0}^N f_N(i | s), \quad (5.9)$$

$$F_N(N_{\text{meas}} | s_c) = 1 - c. \quad (5.10)$$

5.5.2 Combination of Multiple Limits

It is often the case that the limits on the same variable are calculated independently multiple times, for example in multiple detectors, multiple energy regions or in multiple time intervals. Considering that each of such limits independently is a valid limit with the correct coverage, it is tempting to choose the most stringent among them and claim it as the final combined limit. In reality, however, such a combined limit has a lower CL, compared to the individual limits: when taking the most stringent limit, one will always pick a limit with the most advantages statistical fluctuation in it. To take this effect into account, individual limits must be calculated at a CL \hat{c} , higher than the desired confidence c . This section demonstrates how to find \hat{c} .

First, let us define what a c -confidence limit with the correct coverage means. A limit measured in an experiment is itself a random variable, s_c . A limit with confidence c means that the probability that an obtained limit is above the ground truth of the signal strength s is equal to c . Writing it in terms of CDF of s_c , $F_{s_c}(s_c)$, we get:

$$F_{s_c}(s) = 1 - c. \quad (5.11)$$

Turning now to the case of combining n limits calculated with the CL \hat{c} , we define the combined limit as

$$s_{\text{comb}} = \min(s_{\hat{c},1}, s_{\hat{c},2}, \dots, s_{\hat{c},n}). \quad (5.12)$$

The probability of such random variable to be greater than some value x is equal to the multiplication product of probabilities of each individual limits $s_{\hat{c},i}$ to be greater than x . The probability of a random variable to be greater than some value is equal to the complement of its CDF, so we find that

$$1 - F_{s_{\text{comb}}}(s_{\text{comb}}) = (1 - F_{s_{\hat{c}}(s_{\text{comb}})})^n, \quad (5.13)$$

where $F_{s_{\text{comb}}}(s_{\text{comb}})$ is the CDF of s_{comb} . Using Equation 5.11 we find the sought-for expression:

$$\hat{c} = c^{\frac{1}{n}}. \quad (5.14)$$

As can be seen in Equation 5.14, the higher the number of calculated limits is, the higher the confidence of each of them must be in order to achieve the desired CL of the combined limit. The same conclusion is reached in Ref. [154]. To avoid unnecessary inflation of the required CL of individual limits, it is beneficial to consider in the combination procedure only limits that have the potential to be competitive with each other, excluding limits that are *a priori* expected to be weak. In the following section, we describe a procedure used for preselecting potentially competitive limits.

5.5.3 Selection of Energy Regions

A good choice of energy regions to be used for DM limit setting satisfies the following requirements: it has the maximum ratio of expected number of events to the measured number of events, and it has the lowest uncertainty on these numbers. Windows around the quantized peaks in the signal models satisfy both of these requirements: most of the signal model events are within these peaks, and when defining the windows to correspond to the real energies (in contrast to defining them in measured calibrated energy), the effect of the calibration uncertainty is completely eliminated from the signal model. The effect of the resolution uncertainty on the expected number of events is minimized by choosing the windows width to correspond to the resolution: the higher the assumed resolution is, the wider the signal model peaks are, but with the limit-setting window width also defined by the resolution, its variance has only a second-order effect on the expected event counts within these windows. The second-order effect comes from including more events with partial NTL amplification, when the windows become larger.

With this logic in mind, for each of the DM signal model and DM mass we choose the limit-setting windows to be $\pm 3\sigma$ around each of the first four $e^- h^+$ -pair peaks, with σ being the resolution applied to the signal model. Since the peak positions change with the DM mass, the exact positions of the windows are also different for each mass. We define the limit-setting windows only around the peaks that are present in each of the signal model, e.g. at the lowest considered DM masses only the first two peaks are visible in the signal models, so we use only two limit-setting windows for these masses. We do not consider peaks above the fourth one, because the calibration was obtained only up to this peak, with very little calibration data collected for higher energies.

The spectra for each of the signal models and each DM mass have a different ratio of expected events in different peaks. This means that for some cases, normally for low-mass DM, the best limit can be obtained in the first peak, while for other cases, such as DM with higher masses — in the higher peaks. To minimize the number of peaks considered (n in Equation 5.14) we determine which peaks have the potential to provide the best limit for each of the DM mass without calculating them on the data used for the final limit setting. To do this we split the science data into two parts: 10% of the data are used for the peak

preselection, while the remaining 90% are used for the final limit setting. These spectra are shown in Figure 5.26 in Section 5.3.5.

In the idealized scenario, we could determine which peak gives the best result by calculating the limit in each of the peaks with 10% of the data and taking the strongest among them. However, due to statistical fluctuations of the number of observed events, the “best peak” can change when switching from 10% to the remaining 90% of the data. To take this effect into account we calculate the limits with the 10% of the data assuming that the measured event counts are either a 1σ over- or a 1σ under-fluctuation, with σ being the standard deviation of the Poisson distribution. We then calculate DM limits for each of the DM model and mass in each of the first four $e^- h^+$ -pair peaks with over- and under-fluctuation assumptions. For each DM mass and model a peak is selected for the final limit-setting if its limit with the over-fluctuation assumption is stronger than the limits in all the other peaks with the under-fluctuation assumption. Said differently, a peak is selected if it has the potential to provide the best limit with the allowed 1σ fluctuations of the observed counts in each of the peaks. Figure 5.29 shows the limits calculated for each model in each peak with the 10% of the data, as well as the results of the described peak preselection procedure for the DM mass points, considered in the limit setting. Note that in the DM-electron recoil case with $F_{\text{DM}} \propto 1/q^2$ none of the considered DM masses happened to be in regions where more than one peak has the potential to provide the strongest limit. This is different from the $F_{\text{DM}} = 1$ case and the DM absorption cases, in which one or more mass points are in transition regions, where two peaks have the potential to give the strongest limit. Moreover, in the $F_{\text{DM}} = 1$ DM-electron recoil case at masses above $\sim 10 \text{ MeV}/c^2$ the limits calculated in the third and fourth $e^- h^+$ -pair peaks are so close to each other that their 1σ fluctuation bands intersect, and therefore both peaks are selected as potentially best peaks.

When switching from 10% data to the remaining 90% of the data, the peak that gives the strongest limit can change even without statistical fluctuations of the event counts: the number of events in the signal model changes linearly with the exposure, but the measured number of events corrected by the 90% CL grows slower due to the nonlinear behavior of the Poisson distribution variance. To account for this effect we repeat the peak selection procedure described above with the same 10% of the data, but with scaling the exposure, the observed counts and their standard deviations by a factor of 9 to emulate the transition from 10% to 90% of the data. The result of this procedure is shown in Figure 5.30. The selected peaks are very close to those obtained without the $\times 9$ scaling, but not identical.

For the final peak selection, we take a union of the two selections described above for each of the DM model and mass, that is a peak is selected if it is selected in either of the two described procedures. The result of the combination is shown in Figure 5.31.

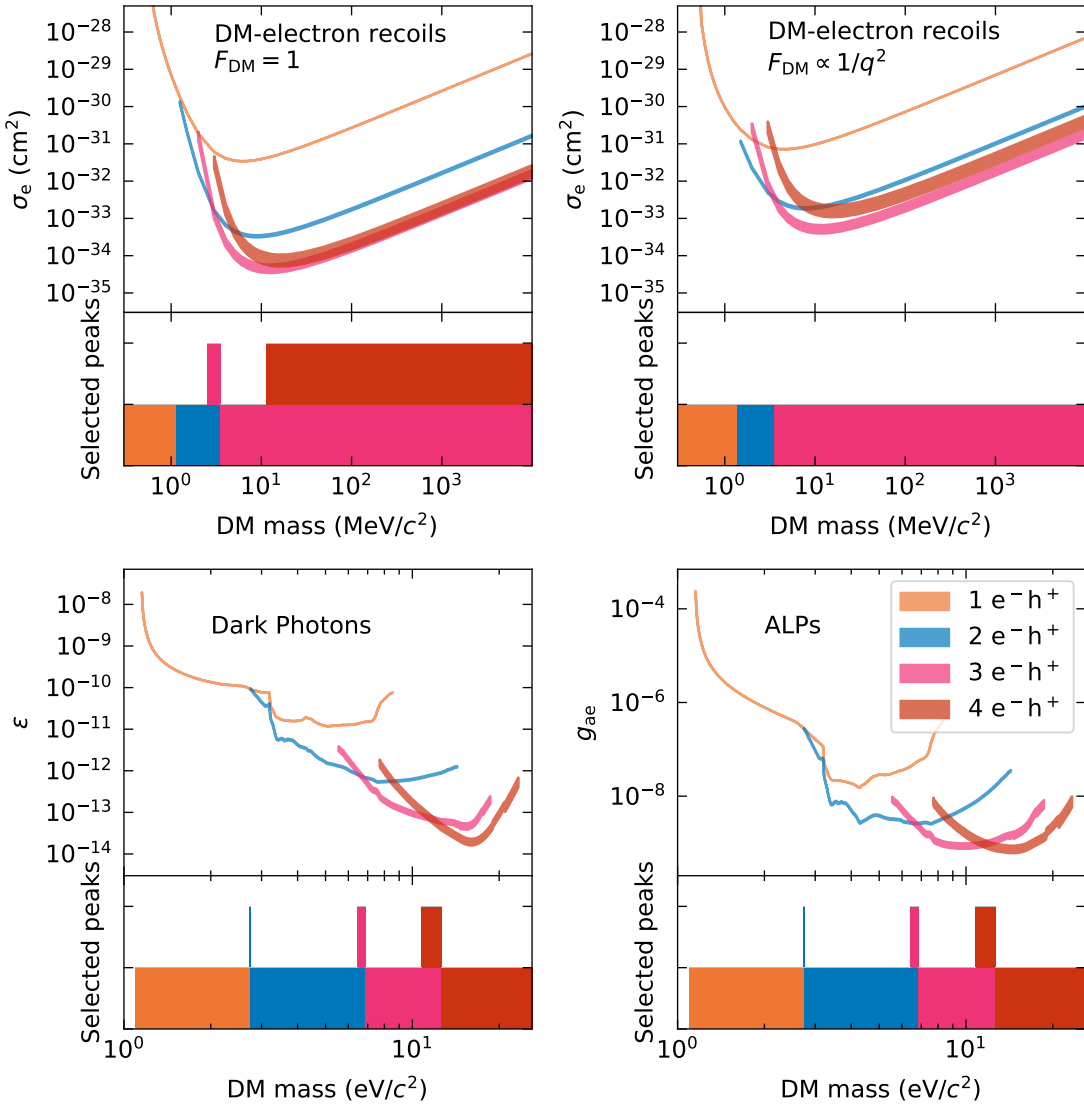


Figure 5.29: 90% confidence level Dark Matter (DM) limits calculated for DM-electron recoil with form-factors $F_{\text{DM}} = 1$ (upper left) and $F_{\text{DM}} \propto 1/q^2$ (upper right), Dark Photon (DP) absorption (lower left) and Axion-Like Particle (ALP) absorption (lower right) using 10% of the HVeV Run 3 data in each of the $e^- h^+$ -pair peaks assuming 1σ over- and under-fluctuation of the observed event counts (colored bands). Plots below the limits show the selected peaks for each DM mass. Courtesy of Taylor Aralis.

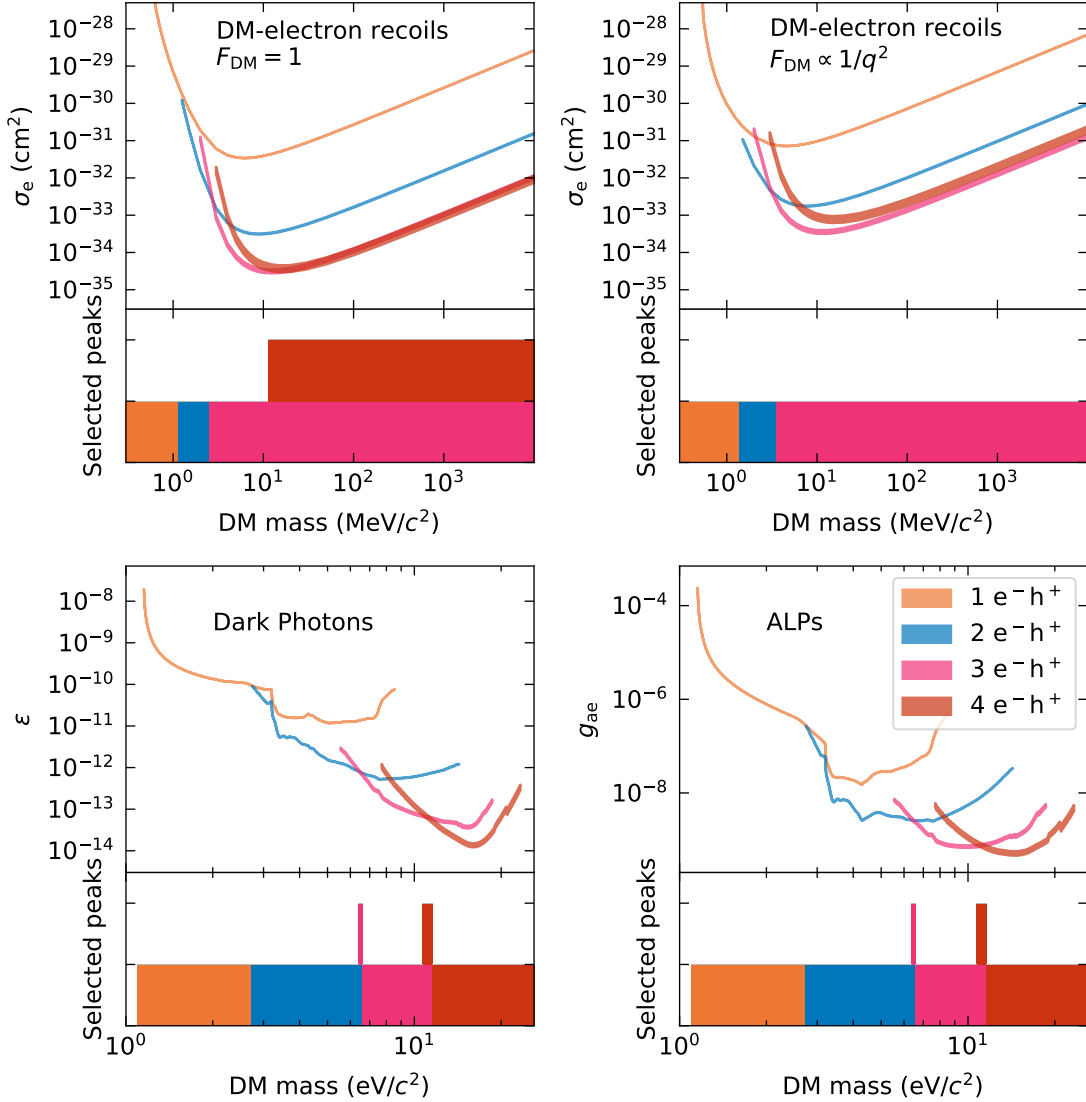


Figure 5.30: 90% confidence level Dark Matter (DM) limits calculated for DM-electron recoil with form-factors $F_{\text{DM}} = 1$ (upper left) and $F_{\text{DM}} \propto 1/q^2$ (upper right), Dark Photon absorption (lower left) and Axion-Like Particle absorption (lower right) using 10% of the HVeV Run 3 data in each of the $e^- h^+$ -pair peaks assuming 1σ over- and under-fluctuation of the observed event counts and scaling the exposure, the counts and their standard deviations by a factor of 9 (colored bands). Plots below the limits show the selected peaks for each DM mass. Courtesy of Taylor Aralis.

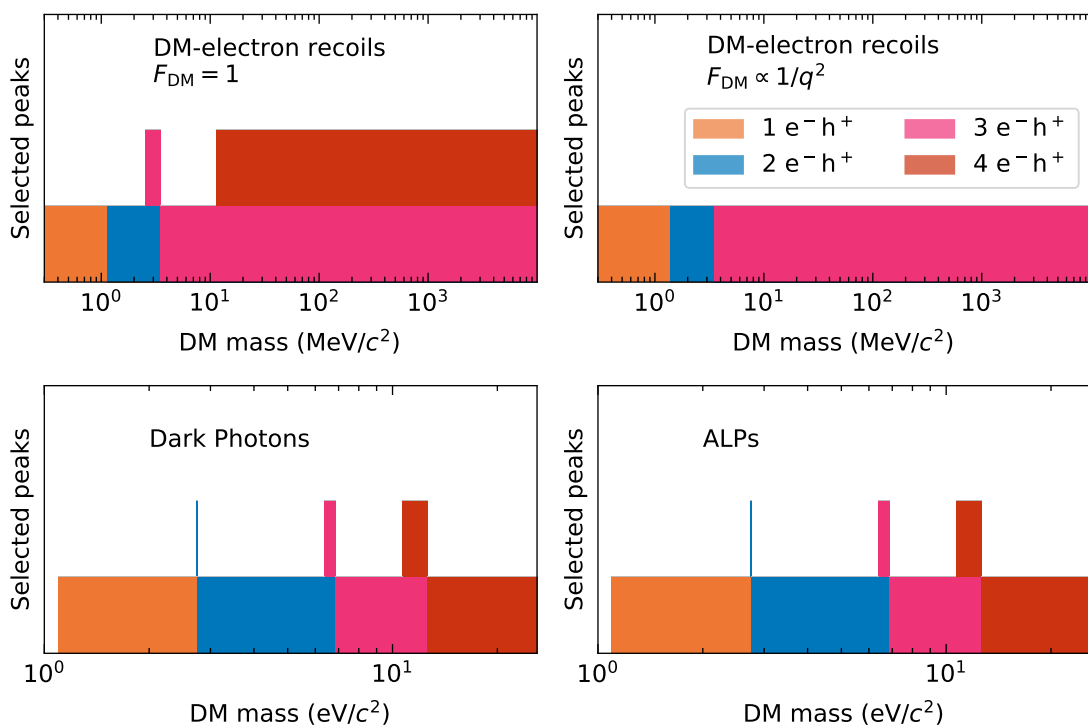


Figure 5.31: $e^- h^+$ -pair peaks selected for the limit-setting as described in text for Dark Matter (DM)-electron recoils with form-factors $F_{\text{DM}} = 1$ (upper left) and $F_{\text{DM}} \propto 1/q^2$ (upper right), Dark Photon (DP) absorption (lower left) and Axion-Like Particle (ALP) absorption (lower right). Courtesy of Taylor Aralis.

5.5.4 Limits without Earth Shielding Effects

With the energy windows preselected for each DM model and mass, we calculate DM limits using the remaining 90% of the science data as described in Section 5.5.2 with the CL corrected by Equation 5.14, with n being the number of preselected energy windows and c being the desired 90% CL. For masses with more than one preselected energy window, we combine the limits by taking the strongest one. This does not introduce bias from statistical fluctuations due to the applied CL correction, as described in Section 5.5.2.

To estimate the effect of the uncertainties in the calibration, resolution, data selection efficiency, CTII probabilities and photoelectric absorption cross section, we calculate the limits 5000 times with all the listed parameters randomly drawn from their corresponding distributions, listed in Table 5.2. Then we construct a band that encompasses 68% of the produced limits and use it as an estimate of the effect of the parameter uncertainties on the DM limits.

Table 5.2: Distributions of parameters used for the limit uncertainty estimation

Parameter	Distribution
Energy calibration	Gaussian with $\mu = 0$ and $\sigma = 1^\dagger$
Energy resolution	Uniform in [3.03, 5.49] eV interval
CT probability	Gaussian with $\mu = 12.8\%$ and $\sigma = 1.5\%$
II probability	Gaussian with $\mu = 1.6\%$ and $\sigma = 1.8\%$
Event selection efficiency	Gaussian with $\mu = 90.05\%$ and $\sigma = 0.05\%$
Photoelectric absorption cross section	Gaussian with $\mu = 0$ and $\sigma = 1^\dagger$

[†] The values drawn from the Gaussian distribution are multiplied by one standard deviation of the parameter of interest (energy-dependent calibration or photoelectric cross section) and added to the nominal values of that parameter. Such values are sometimes referred to as *n-sigma* in literature.

Figure 5.32 shows the Run 3 results for the upper limits on the considered DM model signal strengths: DM-electron recoil cross section for the ultralight and heavy mediator, DP kinetic mixing and ALP axio-electric coupling. The limits demonstrate an improvement of up to a factor of 20 compared to the Run 1 results, although they do not cover any new parameter space for the DM-electron recoil and DP absorption searches. In the case of ALPs, new parameter space is covered in the mass region between 3 and 20 eV/ c^2 . However, this parameter space is disfavored by astrophysical observations [155–157].

For most of the DM masses and models, the effect of the parameter uncertainties is less than 10%, reaching up to 25% for the masses, at which the $e^- h^+$ -pair peak used for the limits changes.

A “kink” in the DM-electron recoil limit with the form factor $F_{\text{DM}} = 1$ at the mass of

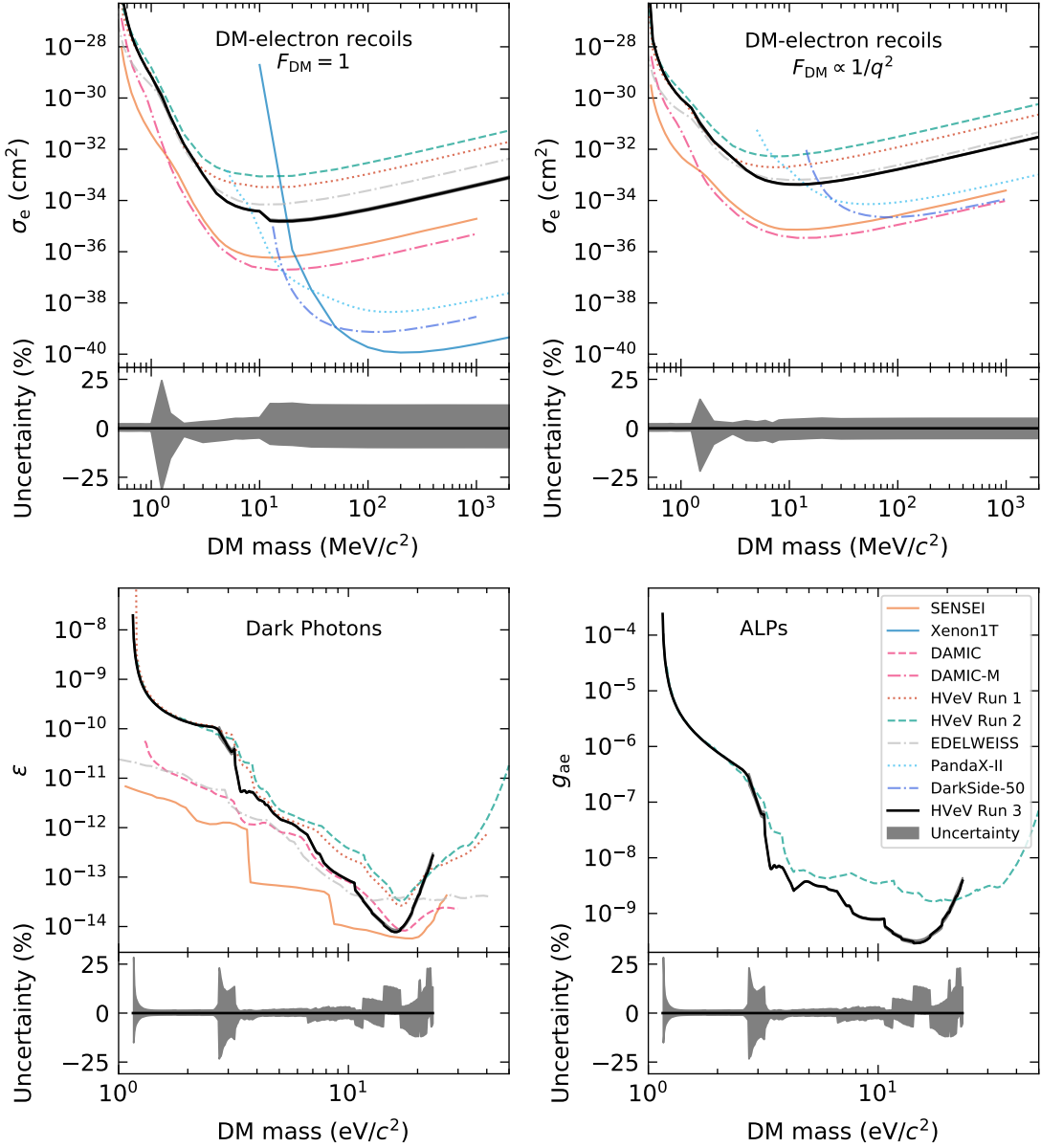


Figure 5.32: 90% confidence level limits on Dark Matter (DM)-electron recoil cross section with form-factors $F_{\text{DM}} = 1$ (upper left) and $F_{\text{DM}} \propto 1/q^2$ (upper right), Dark Photon (DP) kinetic mixing (lower left) and Axion-Like Particle (ALP) axio-electric coupling (lower right). HVeV Run 3 limits are shown in black. Other limits, shown as colored lines, are from SENSEI [80], XENON1T [85], DarkSide-50 [86], DAMIC [82], DAMIC-M [88], SuperCDMS HVeV Run 1 [83] and Run 2 [84], EDELWEISS [81] and PandaX-II [87]. Gray bands around the HVeV Run 3 limits show the sensitivity of the limit to systematic uncertainties. The band is nearly invisible in the logarithmic scale, therefore, it is shown below the limits as a ratio to the HVeV Run 3 limit in percents.

$10 \text{ MeV}/c^2$ is caused by the peak preselection procedure: the fourth $e^- h^+$ -pair peak is used to set the limit for the masses above $10 \text{ MeV}/c^2$, while for the masses below $10 \text{ MeV}/c^2$ other peaks are used, as the fourth peak was not preselected for the limit calculation at these masses.

5.5.5 Earth Shielding Effect

As in Chapter 4, we consider the effect of Earth shielding to determine the maximum signal strength values that are probed by our experiment. At the higher interaction strength value, the DM particles do not reach our detector due to the stopping power of the Earth's atmosphere and rock overburden.

DM-Electron Recoils

The `verne` model used in Chapter 4 is not applicable for DM masses below $10 \text{ MeV}/c^2$. For these masses, a MC simulation of the DM interactions in the Earth's crust and atmosphere is required. In this analysis, we use the DaMaSCUS-CRUST approach [158, 159] to account for the Earth shielding effect. It assumes a model in which the DM halo consists of DM fermions interacting with the Standard Model fermions via a DP. In such a model DM particles recoil off of electrons as well as of nuclei, and the relation between the two cross sections depends only on the masses of the DM fermion and mediator [158, 160–162]. It is shown in Ref. [158] that the DM flux attenuation due to electron recoils in the overburden is strongly subdominant to the attenuation caused by nuclear recoils. Therefore, we only consider nuclear recoils in the overburden when calculating the Earth shielding effect. Interactions in the Earth's atmosphere are neglected as subdominant.

Within the DaMaSCUS-CRUST package, a simulation is used to calculate how the standard DM halo velocity distribution is distorted when DM particles traverse the overburden. Both the energy loss distribution and the scattering angle distribution are considered in the simulation. The velocity distributions are then passed to the `QEdark` model, hardcoded within the DaMaSCUS-CRUST package, to produce electron recoil energy spectra in the detector. The spectra are integrated above a specified detector threshold, and a cross-section-dependent expected number of events for the specified exposure is calculated. The point at which the expected counts curve crosses for the first time the experimentally measured number of events (corrected by the Poisson statistic to provide a 90% CL upper limit) defines the lower boundary of the cross-section exclusion region. Unlike the case in which the shielding is not taken into account, the expected number of events with shielding does not grow monotonically with cross section: at some cross-section value the expected number of interactions in the detector drops steeply, intersecting with the measured number of events again, thus defining the upper boundary of the exclusion region (see Figure 5.33). If the measured number of events is higher than the expected number of events for a certain DM

mass for all cross-section values, no cross-section values can be excluded for this DM mass. The experiment's sensitivity to these DM masses is canceled by the shielding effect.

The limit itself, that is the lower boundary of the exclusion region, depends on the shielding very weakly. Therefore, we use DaMaSCUS-CRUST to calculate only the upper boundaries of the exclusion regions, while taking the limits calculated in the previous section as the lower boundaries. It is important to list the numerous shortcomings of the DaMaSCUS-CRUST package and how we employ it:

- when specifying the depth of the overburden (107 m), we assume that the DM particles arrive to the detector vertically from above, ignoring the DM wind flux direction and its daily variations. This is a major simplification that affects the upper boundary estimation by a factor of $\sim 2\text{--}4$;
- we assume the standard continental crust composition for the overburden [163], as it is done in the default DaMaSCUS-CRUST configuration file;
- an earlier version of the QEDark model is hard-coded within the DaMaSCUS-CRUST package. This version is slightly different from the one used to calculate the limits in Section 5.5.4;
- DaMaSCUS-CRUST only allows energy regions of the form $[E_{\text{th}}; +\infty)$, with E_{th} being the threshold energy in units of number of e^-h^+ pairs. We run DaMaSCUS-CRUST for four cases with E_{th} set to 1, 2, 3 or 4 e^-h^+ pairs. These energy regions are different from the regions used in Section 5.5.4;
- a simplistic ionization model is used within DaMaSCUS-CRUST to convert the threshold E_{th} given in the number of e^-h^+ pairs to the recoil energy E_r measured in eV: $E_{\text{th}} = \text{Floor}((E_r - E_{\text{gap}})/\epsilon)$ with $E_{\text{gap}}=1.11\text{ eV}$ and $\epsilon=3.6\text{ eV}$ being the values of Si band gap energy and the average energy to produce an e^-h^+ pair hardcoded in the DaMaSCUS-CRUST simulation;
- resolution and CTII effects are not included into the DaMaSCUS-CRUST limit-setting pipeline;
- individual upper boundaries of the exclusion regions for four different E_{th} values are calculated with 90% CL and then an upper envelope of them is taken, ignoring the CL correction described by Equation 5.14.

Figure 5.34 shows the calculated exclusion regions, with the upper boundaries estimated as described. The sensitivity of our experiment to the DM masses above $\sim 100\text{ MeV}/c^2$ for the heavy mediator case ($F_{\text{DM}} = 1$) is canceled by the shielding effect. Considering all the listed shortcomings, we only claim that the upper boundaries of the exclusion regions are order-of-magnitude estimations, with further work required to calculate them more precisely.

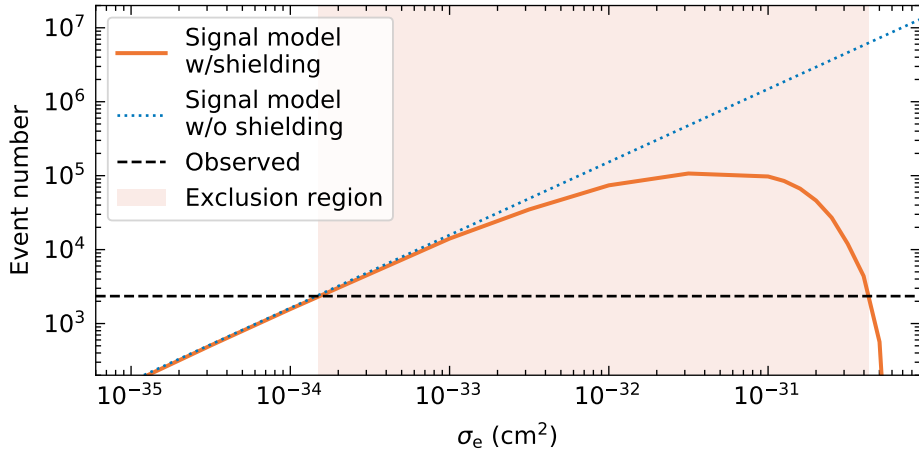


Figure 5.33: Expected number of events in the second $e^- h^+$ -pair peak and above ($E_{\text{th}} = 2$) with the HVeV Run 3 exposure for Dark Matter (DM)-electron recoils with 20 MeV/ c^2 DM mass and form-factor $F_{\text{DM}} = 1$ with (orange line) and without (blue dotted line) shielding. The black dashed line shows the number of events observed in the same energy region, corrected to obtain 90% confidence level. The intersections of the shielded model line with the observed counts line define the exclusion region (shaded area).

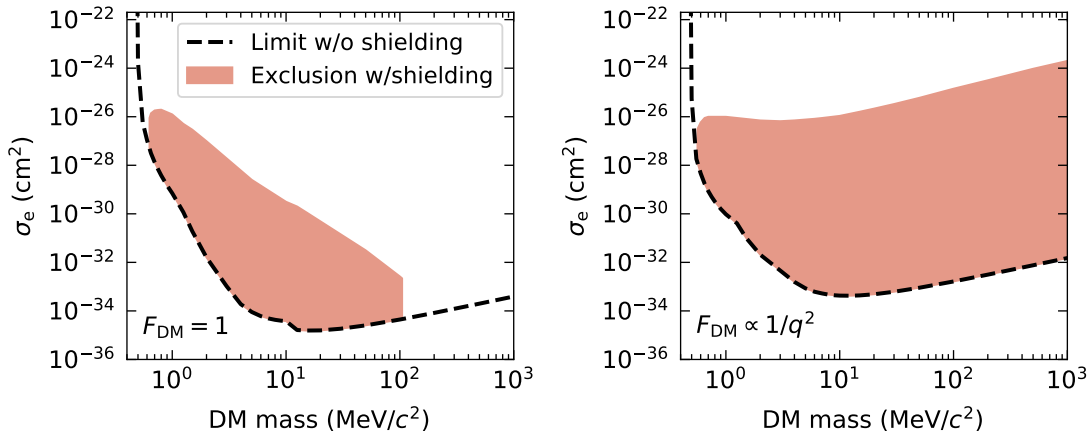


Figure 5.34: 90% confidence level exclusion regions (shaded areas) of Dark Matter (DM)-electron recoil cross section with form-factors $F_{\text{DM}} = 1$ (left) and $F_{\text{DM}} \propto 1/q^2$ (right). The lower boundary is calculated without taking shielding into account. The upper boundary is calculated with DaMaSCUS-CRUST. The limits calculated in Section 5.5.4 are shown as dashed lines.

DM Absorption

Assuming that electron absorption is the dominant channel of interaction in the overburden, the calculation of the overburden effect on the DP and ALP absorption limits is simpler comparing to the DM-electron recoil case. The DM velocity distributions remain unchanged,

but the overall DM flux is attenuated as

$$\Phi = \Phi_0 e^{-\rho L \sigma}, \quad (5.15)$$

where Φ and Φ_0 are the attenuated and unattenuated DM flux respectively, σ is the DP or ALP absorption cross section measured in cm^2/g , ρ is the overburden density and L is the length the DM particles traverse in the overburden.

The rates of DP and ALP electron absorption are given by Equations 1.12 and 1.14, respectively. Converting the DM interaction rates to the mass attenuation coefficients σ using the $R = \rho_{\text{DM}} \sigma v_{\text{DM}} / m_{\text{DM}}$ relation, we find:

$$\sigma_{\text{DP}} = \frac{\varepsilon_{\text{eff}}^2 \sigma_1}{\rho v_{\text{DM}}} = \frac{\varepsilon^2 m_{A'}^2 \sigma_1}{(m_{A'}^2 - 2m_{A'}\sigma_2 + \sigma_1^2 + \sigma_2^2)\rho v_{\text{DM}}}, \quad (5.16)$$

$$\sigma_{\text{ALP}} = \frac{3g_{ae}^2 m_a^2 \sigma_1}{16\pi\alpha m_e \rho v_{\text{DM}}}, \quad (5.17)$$

where $\sigma_{\text{DP(ALP)}}$ is the DP (ALP) mass attenuation coefficient, ε is the kinetic mixing, ε_{eff} is the effective kinetic mixing that takes into account in-medium effects, g_{ae} is the axio-electric coupling, v_{DM} is the DM velocity, σ_1 and σ_2 are real and imaginary parts of the complex conductivity of the material at the energy equal to the DM mass, ρ is the material density, $m_{A'}$ the DP mass, m_a is the ALP mass, and m_e is the electron mass.

Following Ref. [164], we make an order-of-magnitude estimation of the kinetic mixing and axio-electric coupling, at which the overburden attenuates the DM flux by a factor of e (Euler's number), by setting $\sigma_{\text{DP(ALP)}} \rho L$ to unity, where L is the distance traveled in the overburden:

$$\varepsilon_{\text{max}} = \left(\frac{\sigma_1 L m_{A'}^2}{v_{\text{DM}} (m_{A'}^2 - 2m_{A'}\sigma_2 + \sigma_1^2 + \sigma_2^2)} \right)^{-1/2}, \quad (5.18)$$

$$g_{ae,\text{max}} = \left(\sigma_1 \frac{3m_a^2 L}{16\pi\alpha m_e v_{\text{DM}}} \right)^{-1/2}. \quad (5.19)$$

Figure 5.35 shows the estimates obtained with Equation 5.18 and Equation 5.19 together with the limits obtained in Section 5.5.4. Again, we assume that DM particles come vertically from above, traversing 107 m of the NEXUS overburden. Similarly to Ref. [164], the overburden is assumed to be made of Si at room temperature, which is a very simplistic assumption. The reason for this is a lack of complex conductivity measurements for the materials comprising the Earth's crust and atmosphere at the energies of interest of this analysis. Therefore, we only claim a very rough order-of-magnitude estimate of the signal strength levels at which the overburden attenuates the DM signal by a factor of e . At some point above this level the Earth shielding attenuates the flux so strongly that no DM particles reach the detectors.

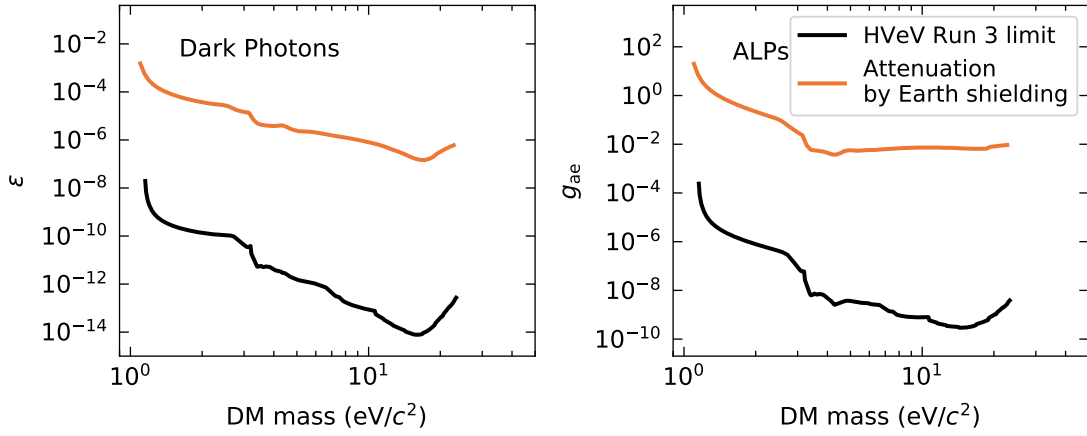


Figure 5.35: 90% confidence level limits from Section 5.5.4 (black) for Dark Photon (DP) (left) and Axion-Like Particle (ALP) (right) absorption and an order-of-magnitude estimation of the signal strength at which Earth shielding attenuates the DM signal by a factor of e (orange).

5.6 Discussion

The dominant background in the two previous HVeV runs was an unidentified source of burst events. It was suggested that burst events could be indirectly caused by cosmic rays: they could activate some scintillating material in the vicinity of the detector or produce Cherenkov or transition radiation when cosmic rays of their secondaries pass through the surrounding materials [165]. Therefore, when starting Run 3, we hoped to improve the sensitivity to DM-electron interactions by reducing the rate of burst events by means of the two changes: improved shielding from cosmic rays and anti-coincidence event selection.

When developing the processing algorithm for this analysis, particular attention was paid to burst events. We developed a trigger algorithm that resolves individual pulses that occur with a time separation as little as 120 μ s. This allowed us to identify and count burst events. In addition to the analysis described in this chapter, we reprocessed the Run 2 HV data with the same algorithm that allowed us to compare the burst rate between the two runs. We defined a burst as an event with three more events occurring within the next 4 ms. With such definition, the rate of bursts in Run 2 and Run 3 was measured to be (0.093 ± 0.006) Hz and (0.144 ± 0.004) Hz, respectively. Thus, the rate of bursts has increased by a factor of 1.5 when moving from a surface run to an underground run. This result tentatively refutes the hypothesis of cosmogenic secondaries as a cause of burst events.

The increased rate of burst events would have harmed the sensitivity to DM interactions, if it had not been counteracted by the anti-coincidence event selection. We showed that most of the events observed in Run 3 was observed in coincidence in multiple detectors. This allowed us to remove these events, which greatly reduced the background rate in our

experiment. As a result, the exclusion limits obtained in Run 3 demonstrate an improvement of up to a factor of 20 for some of the DM models and masses compared to the Run 1 and Run 2 limits. In particular, the best improvement is seen for the DM-electron scattering via a heavy mediator for DM masses above $10 \text{ MeV}/c^2$ (factor of 20). For the case of bosonic DM, such as DPs and ALPs, the highest improvement is achieved for masses above $10 \text{ eV}/c^2$ (factor of 5–10).

Despite these improvements, the only new direct search parameter space excluded by the Run 3 is the ALP axio-electric coupling. For all the other considered DM models, CCD-based experiments, such as DAMIC and SENSEI, demonstrate sensitivities, surpassing the HVeV Run 3 sensitivity by up to two orders of magnitude. If SENSEI and DAMIC data were used to probe the ALP parameter space, they would also surpass the Run 3 limits by the same factor. The difference between the HVeV Run 3 limits and the CCD limits is especially large in the lowest probed DM masses. Sensitivity in these regions is defined by the rate of $1-e^-h^+$ -pair events. We did not observe any improvement in this rate between Run 1 and Run 3, therefore, identification and mitigation of the source of the low-energy background remains crucial for the HVeV detectors. We discuss the progress in this regard in the next chapter.

Chapter 6

Conclusion and Outlook

This chapter summarizes the work described in this dissertation and gives an outlook on the ongoing developments in the HVeV program.

After introducing the topic of DM and describing the SuperCDMS detectors and their working principles, we started the main part of this dissertation by developing an improved detector response model for detectors utilizing NTL amplification. The component of the response model that we improve upon is the CTII effects, that is the disappearance and creation of new charge carriers by charges drifting in the crystal under the influence of an electric field. By modeling the CTII effects of different types as independent effects with certain mean free paths and considering their combinations, we derived PDFs of NTL energy expected in bulk and surface events. We showed that the CTII model used in previous HVeV analyses does not accurately describe the detector response to interactions occurring in the bulk of the detector. As the DM interactions are expected to occur in the bulk, our improved modeling is crucial for DM searches that utilize full spectral shapes of measured and expected signals. For example, the shape of the entire expected DM spectrum is required for analyses based on the profile likelihood ratio method. Moreover, since the shapes of the surface and bulk event spectra are different within our model, it can provide additional information for studies of unidentified types of background, or even statistically distinguish between DM and background components in measured energy spectra.

Moving from the detector response modeling to the experimental data, the first data analysis we conducted within the scope of this dissertation is the so-called 0VeV analysis — the first DM search analysis with an HVeV detector operated without an applied voltage bias, and thus without the NTL amplification. This operation mode is well suited for nuclear recoil searches since it is insensitive to ionization yield — a parameter with high systematic uncertainty. In this analysis, we benefited from an improved resolution of (2.65 ± 0.02) eV of a second generation HVeV detector and set a very low energy threshold of 9.2 eV. This allowed us to reach energies that correspond to nuclear recoils of DM with masses as low as ~ 70 MeV/c². However, with the energy threshold pushed into the noise-dominated region,

the extracted upper bound on the DM-nucleon scattering cross section for masses between 70 and 90 MeV/ c^2 turned out to be very high, of the order of 10^{-27} cm^2 . With such a high cross section, all the DM flux would be shielded by the Earth's atmosphere. The Earth shielding effect eliminates sensitivity of the experiment to the masses below 92 MeV/ c^2 . We conclude that setting an energy threshold within the noise-dominated region gives no immediate advantage. However, it could still be beneficial if the noise component is carefully modeled and subtracted from the spectrum. In general, to gain sensitivity to nuclear recoils of DM with masses lower than 92 MeV/ c^2 , a detector with a better energy resolution is required. Anecdotally, the next generation of HVeV detectors will boast a two-fold improvement of the resolution, which will push the HVeV sensitivity to the unprobed parameter space.

Above the noise-dominated region, an excess of low-energy events was observed in the 0VeV spectrum. Similar excesses, known as the LEE in the LDM-search community, are observed in multiple other cryogenic and CCD-based semiconductor detectors [78, 90]. Understanding and mitigating the LEE is the most crucial step towards improving the sensitivity of solid state detectors to nuclear recoils of DM with masses below 1 GeV/ c^2 . The following possible LEE sources are hypothesised: Cherenkov radiation, transition radiation, or luminescence in materials surrounding detectors [165], stress-related crystal microfractures [166], or long-lived metastable states in crystals [167].

The second analysis presented in this dissertation is the analysis of the first HVeV data taken underground — the HVeV Run 3 data. In contrast to the 0VeV analysis, the data used in the Run 3 analysis was acquired in the HV mode, which allowed us to probe DM-electron interactions. Special care was taken in reconstructing burst events — pile-ups of time-correlated events that had a detrimental effect on the sensitivity of the first two HVeV runs to electron-coupled DM. We observed that the rate of bursts did not decrease despite the $\sim 100 \text{ m}$ rock overburden. However, we improved upon exclusion limits obtained in the previous runs for DM-electron scattering cross section and DP absorption, and reached previously unexplored by direct detection experiments parameter space of ALP absorption. This was achieved by means of the event selection based on the anti-coincidence between multiple HVeV detectors, operated in the same housing. The best improvement is achieved in the limits calculated using area of the measured spectrum corresponding to 3 and 4 $e^- h^+$ pairs produced in the crystal. For example, an improvement by a factor of 20 is achieved for the DM-electron scattering via a heavy mediator for DM masses above 10 MeV/ c^2 . Limits calculated from the one- $e^- h^+$ -pair part of the spectrum, on the other hand, did not demonstrate an improvement compared to the previous runs. The rate of one- $e^- h^+$ -pair events remained approximately the same, of the order of 2 Hz. As in the case of nuclear recoil searches, understanding and mitigating this background is needed to improve the sensitivity of HVeV detectors to electron-coupled DM interactions.

The ability of the HVeV detectors to operate in two different modes, with and without NTL amplification, opens up a unique way of studying backgrounds. In Ref. [130], a

comparative analysis of the HVeV Run 2 data acquired in the HV and 0V modes led to a hypothesis that the observed LEE (or a part of it) in both modes is caused by luminescence of materials surrounding the detector. Silicon dioxide in the detector holders is named as a possible source of luminescence, causing the LEE.

For the next HVeV run, HVeV Run 4, a new detector holder shown in Figure 6.1 was designed, with no components containing silicon dioxide. Four HVeV detectors mounted in such holders are deployed in this run at NEXUS, Fermilab. No burst events are observed in the HV mode in Run 4, confirming the silicon dioxide hypothesis. This leads to a significant improvement in the observed background rate, which in turn leads to a significant improvement of the DM sensitivity. As the analysis is still ongoing, we do not share the spectrum or the expected DM limits at this point. It remains to be seen which fraction of the LEE observed in the 0VeV analysis was caused by the bursts from silicon dioxide.

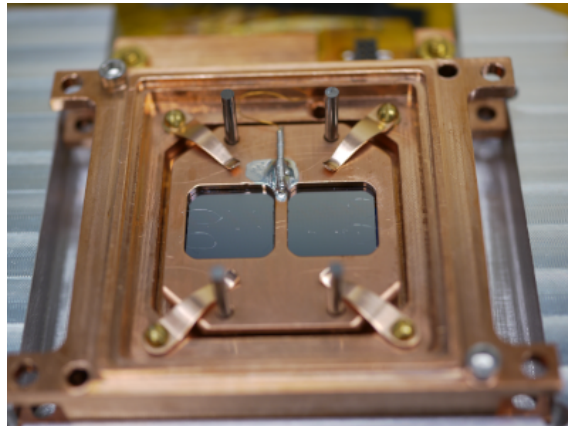


Figure 6.1: HVeV Run 4 detector holder with two out of four deployed detectors visible. The new detector holder does not contain silicon dioxide which was identified as a source of burst events in previous HVeV runs.

With the problem of burst events solved, the remaining background in the HV mode is in the energy region corresponding to one NTL-amplified $e^- h^+$ pair. Leakage of charges from the electrodes is the current hypothesis for the source of this background. To test this hypothesis, a new type of HVeV detector with an insulating layer between the electrodes and the crystal was developed. The next HVeV run is planned for early 2024 at SNOLAB, before the start of the SuperCDMS SNOLAB experiment. Both the current generation and the next generation of HVeV detectors will be deployed. It remains to be seen whether the new HVeV detectors can further expand our knowledge of DM and low energy background.

Bibliography

- [1] V. C. Rubin, W. K. Ford, "Rotation of the Andromeda Nebula from a Spectroscopic Survey of Emission Regions", *Astrophys. J.* 159 (1970) 379. doi:10.1086/150317.
- [2] Planck Collaboration, N. Aghanim *et al.*, "Planck 2018 results. VI. Cosmological parameters", *Astron. Astrophys.* 641 (2020) A6. doi:10.1051/0004-6361/201833910.
- [3] F. Zwicky, "Die Rotverschiebung von Extragalaktischen Nebeln. German.", *Helvetica Physica Acta* 6 (1933) 110–127.
URL <https://ui.adsabs.harvard.edu/abs/1933AcHPh...6..110Z/abstract>
- [4] F. Zwicky, "On the Masses of Nebulae and of Clusters of Nebulae", *Astrophys. J.* 86 (1937) 217–246. doi:10.1086/143864.
- [5] A. Bosma, "21-cm line studies of spiral galaxies. II. The distribution and kinematics of neutral hydrogen in spiral galaxies of various morphological types", *Astron. J.* 86 (1981) 1825–1846. doi:10.1086/113063.
- [6] Y. Sofue, "Rotation and mass in the Milky Way and spiral galaxies", *Publ. Astron. Soc. Japan* 69 (2017) R1. doi:10.1093/pasj/psw103.
- [7] E. Corbelli, P. Salucci, "The extended rotation curve and the dark matter halo of M33", *Mon. Notices Royal Astron. Soc.* 311 (2000) 441–447. doi:10.1046/j.1365-8711.2000.03075.x.
- [8] J. F. Rothe, "Low-Threshold Cryogenic Detectors for Low-Mass Dark Matter Search and Coherent Neutrino Scattering", Ph.D. thesis, TU München (2021).
URL <https://publications.mppmu.mpg.de/?action=search&language=en&mpi=MPP-2021-243>
- [9] A. Einstein, "Lens-Like Action of a Star by the Deviation of Light in the Gravitational Field", *Science* 84 (1936) 506. doi:10.1126/science.84.2188.
- [10] EROS-2 Collaboration, P. Tisserand *et al.*, "Limits on the Macho content of the Galactic Halo from the EROS-2 Survey of the Magellanic Clouds", *Astron. Astrophys.* 469 (2007) 387–404. doi:10.1051/0004-6361:20066017.

- [11] J. A. Tyson, G. P. Kochanski, I. P. Dell'Antonio, "Detailed Mass Map of CL 0024+1654 from Strong Lensing", *Astrophys. J.* 498 (1998) L107–L110. doi:10.1086/311314.
- [12] J. D. Bekenstein, "Relativistic gravitation theory for the modified Newtonian dynamics paradigm", *Phys. Rev. D* 70 (2004) 083509. doi:10.1103/PhysRevD.70.083509.
- [13] D. Clowe, M. Bradač, A. H. Gonzalez, M. Markevitch, S. W. Randall, C. Jones, D. Zaritsky, "A Direct Empirical Proof of the Existence of Dark Matter", *Astrophys. J.* 648 (2006) L109. doi:10.1086/508162.
- [14] A. Liddle, "An introduction to modern cosmology", John Wiley & Sons, 2015.
- [15] D. J. Fixsen, "The Temperature of the Cosmic Microwave Background", *Astrophys. J.* 707 (2009) 916. doi:10.1088/0004-637X/707/2/916.
- [16] C. Bennett *et al.*, "Four-Year COBE DMR Cosmic Microwave Background Observations: Maps and Basic Results", *Astrophys. J.* 464 (1996) L1. doi:10.1086/310075.
- [17] C. L. Bennett *et al.*, "Nine-Year Wilkinson Microwave Anisotropy Probe (WMAP) Observations: Final Maps and Results", *Astrophys. J., Suppl. Ser.* 208 (2013) 20. doi:10.1088/0067-0049/208/2/20.
- [18] Planck Collaboration, N. Aghanim *et al.*, "Planck 2018 results I. Overview and the cosmological legacy of Planck", *Astron. Astrophys.* 641 (2020) A1. doi:10.1051/0004-6361/201833880.
- [19] S. Dodelson, "Modern cosmology", Elsevier, 2003.
- [20] D. J. Eisenstein *et al.*, "Detection of the Baryon Acoustic Peak in the Large-Scale Correlation Function of SDSS Luminous Red Galaxies", *Astrophys. J.* 633 (2005) 560. doi:10.1086/466512.
- [21] Planck Collaboration, P. A. R. Ade *et al.*, "Planck 2015 results. XIII. Cosmological parameters", *Astron. Astrophys.* 594 (2016) A13. doi:10.1051/0004-6361/201525830.
- [22] Planck Collaboration, R. Adam *et al.*, "Planck 2015 results. I. Overview of products and scientific results", *Astron. Astrophys.* 594 (2016) A1. doi:10.1051/0004-6361/201527101.
- [23] R. W. Schnee, "Introduction to Dark Matter Experiment", in: Physics of the Large and the Small, World Scientific, 2011, pp. 775–829. doi:10.1142/9789814327183_0014.
- [24] G. Jungman, M. Kamionkowski, K. Griest, "Supersymmetric dark matter", *Phys. Rep.* 267 (1996) 195–373. doi:10.1016/0370-1573(95)00058-5.

- [25] LUX-ZEPLIN Collaboration, J. Aalbers *et al.*, “First Dark Matter Search Results from the LUX-ZEPLIN (LZ) Experiment”, Phys. Rev. Lett. 131 (2023) 041002. doi:10.1103/PhysRevLett.131.041002.
- [26] XENON Collaboration, E. Aprile *et al.*, “First Dark Matter Search with Nuclear Recoils from the XENONnT Experiment”, Phys. Rev. Lett. 131 (2023) 041003. doi:10.1103/PhysRevLett.131.041003.
- [27] PandaX-II Collaboration, Q. Wang *et al.*, “Results of dark matter search using the full PandaX-II exposure”, Chin. Phys. C. 44 (2020) 125001. doi:10.1088/1674-1137/abb658.
- [28] H. Baer, V. Barger, D. Sengupta, S. Salam, K. Sinha, “Status of weak scale supersymmetry after LHC Run 2 and ton-scale noble liquid WIMP searches”, Eur. Phys. J. Spec. Top. 229 (2020) 3085–3141. doi:10.1140/epjst/e2020-000020-x.
- [29] B. W. Lee, S. Weinberg, “Cosmological Lower Bound on Heavy-Neutrino Masses”, Phys. Rev. Lett. 39 (1977) 165. doi:10.1103/PhysRevLett.39.165.
- [30] J. Alexander *et al.*, “Dark Sectors 2016 Workshop: Community Report” (2016). arXiv:1608.08632.
- [31] D. Hooper, K. M. Zurek, “Natural supersymmetric model with MeV dark matter”, Phys. Rev. D 77 (2008) 087302. doi:10.1103/PhysRevD.77.087302.
- [32] C. Bœhm, P. Fayet, “Scalar dark matter candidates”, Nucl. Phys. B 683 (2004) 219–263. doi:10.1016/j.nuclphysb.2004.01.015.
- [33] L. J. Hall, K. Jedamzik, J. March-Russell, S. M. West, “Freeze-in production of FIMP dark matter”, J. High Energy Phys. 2010 (2010) 080. doi:doi.org/10.1007/JHEP03(2010)080.
- [34] D. E. Kaplan, M. A. Luty, K. M. Zurek, “Asymmetric dark matter”, Phys. Rev. D 79 (2009) 115016. doi:10.1103/PhysRevD.79.115016.
- [35] Y. Hochberg, E. Kuflik, T. Volansky, J. G. Wacker, “Mechanism for Thermal Relic Dark Matter of Strongly Interacting Massive Particles”, Phys. Rev. Lett. 113 (2014) 171301. doi:10.1103/PhysRevLett.113.171301.
- [36] E. Kuflik, M. Perelstein, N. R.-L. Lorier, Y.-D. Tsai, “Elastically Decoupling Dark Matter”, Phys. Rev. Lett. 116 (2016) 221302. doi:10.1103/PhysRevLett.116.221302.

- [37] J. Lewin, P. Smith, “Review of mathematics, numerical factors, and corrections for dark matter experiments based on elastic nuclear recoil”, *Astropart. Phys.* 6 (1996) 87–112. doi:10.1016/S0927-6505(96)00047-3.
- [38] R. H. Helm, “Inelastic and Elastic Scattering of 187-MeV Electrons from Selected Even-Even Nuclei”, *Phys. Rev.* 104 (1956) 1466–1475. doi:10.1103/PhysRev.104.1466.
- [39] F. Mayet *et al.*, “A review of the discovery reach of directional Dark Matter detection”, *Phys. Rep.* 627 (2016) 1–49. doi:10.1016/j.physrep.2016.02.007.
- [40] D. Baxter *et al.*, “Recommended conventions for reporting results from direct dark matter searches”, *Eur. Phys. J. C* 81 (2021) 907. doi:10.1140/epjc/s10052-021-09655-y.
- [41] CDMS Collaboration, Z. Ahmed *et al.*, “Search for inelastic dark matter with the CDMS II experiment”, *Phys. Rev. D* 83 (2011) 112002. doi:10.1103/PhysRevD.83.112002.
- [42] R. Essig, M. Fernández-Serra, J. Mardon, A. Soto, T. Volansky, T.-T. Yu, “Direct detection of sub-GeV dark matter with semiconductor targets”, *J. High Energ. Phys.* 2016 (2016) 46. doi:10.1007/JHEP05(2016)046.
- [43] R. Catena, T. Emken, M. Matas, N. A. Spaldin, E. Urdshals, “Crystal responses to general dark matter-electron interactions”, *Phys. Rev. Res.* 3 (2021) 033149. doi:10.1103/PhysRevResearch.3.033149.
- [44] R. Essig, M. Fernández-Serra, J. Mardon, A. Soto, T. Volansky, T.-T. Yu, “QEdark”, GitHub repository (2021). Last accessed 13 August 2023.
URL <https://github.com/tientienyu/QEdark>
- [45] S. Knapen, J. Kozaczuk, T. Lin, “Python package for dark matter scattering in dielectric targets”, *Phys. Rev. D* 105 (2022) 015014. doi:10.1103/PhysRevD.105.015014.
- [46] S. M. Griffin, K. Inzani, T. Trickle, Z. Zhang, K. M. Zurek, “Extended calculation of dark matter-electron scattering in crystal targets”, *Phys. Rev. D* 104 (2021) 095015. doi:10.1103/PhysRevD.104.095015.
- [47] C. E. Dreyer, R. Essig, M. Fernández-Serra, A. Singal, C. Zhen, “Fully ab-initio all-electron calculation of dark matter–electron scattering in crystals with evaluation of systematic uncertainties” (2023). arXiv:2306.14944.
- [48] M. Pospelov, A. Ritz, M. Voloshin, “Bosonic super-WIMPs as keV-scale dark matter”, *Phys. Rev. D* 78 (2008) 115012. doi:10.1103/PhysRevD.78.115012.

- [49] I. M. Bloch, R. Essig, K. Tobioka, T. Volansky, T.-T. Yu, "Searching for dark absorption with direct detection experiments", *J. High Energy Phys.* 2017 (2017) 087. doi:10.1007/JHEP06(2017)087.
- [50] P. Arias, D. Cadamuro, M. Goodsell, J. Jaeckel, J. Redondo, A. Ringwald, "WISPy cold dark matter", *J. Cosm. Astropart. Phys.* (2012) 013. doi:10.1088/1475-7516/2012/06/013.
- [51] A. E. Nelson, J. Scholtz, "Dark light, dark matter, and the misalignment mechanism", *Phys. Rev. D* 84 (2011) 103501. doi:10.1103/PhysRevD.84.103501.
- [52] Y. Hochberg, T. Lin, K. M. Zurek, "Absorption of light dark matter in semiconductors", *Phys. Rev. D* 95 (2017) 023013. doi:10.1103/PhysRevD.95.023013.
- [53] R. D. Peccei, H. R. Quinn, "CP Conservation in the Presence of Pseudoparticles", *Phys. Rev. Lett.* 38 (1977) 1440–1443. doi:10.1103/PhysRevLett.38.1440.
- [54] R. D. Peccei, H. R. Quinn, "Constraints imposed by CP conservation in the presence of pseudoparticles", *Phys. Rev. D* 16 (1977) 1791–1797. doi:10.1103/PhysRevD.16.1791.
- [55] S. Weinberg, "A New Light Boson?", *Phys. Rev. Lett.* 40 (1978) 223–226. doi:10.1103/PhysRevLett.40.223.
- [56] J. Preskill, M. B. Wise, F. Wilczek, "Cosmology of the invisible axion", *Phys. Lett. B* 120 (1983) 127–132. doi:10.1016/0370-2693(83)90637-8.
- [57] A. R. Zhitnitsky, "On Possible Suppression of the Axion Hadron Interactions. (In Russian)", *Sov. J. Nucl. Phys.* 31 (1980) 260.
- [58] M. Dine, W. Fischler, M. Srednicki, "A simple solution to the strong CP problem with a harmless axion", *Phys. Lett. B* 104 (1981) 199–202. doi:10.1016/0370-2693(81)90590-6.
- [59] J. E. Kim, "Weak-Interaction Singlet and Strong CP Invariance", *Phys. Rev. Lett.* 43 (1979) 103–107. doi:10.1103/PhysRevLett.43.103.
- [60] M. Shifman, A. Vainshtein, V. Zakharov, "Can confinement ensure natural CP invariance of strong interactions?", *Nucl. Phys. B* 166 (1980) 493–506. doi:10.1016/0550-3213(80)90209-6.
- [61] C. B. Adams *et al.*, "Snowmass 2021 White Paper: Axion Dark Matter" (2022). arXiv:2203.14923.
- [62] J. Cooley *et al.*, "Report of the Topical Group on Particle Dark Matter for Snowmass 2021" (2022). arXiv:2209.07426.

- [63] E. W. Kolb, D. J. H. Chung, A. Riotto, “WIMPZILLAS!” (1998). [arXiv:hep-ph/9810361](https://arxiv.org/abs/hep-ph/9810361).
- [64] B. J. Carr, S. W. Hawking, “Black Holes in the Early Universe”, Mon. Not. R. Astron. Soc. 168 (1974) 399. doi:[10.1093/mnras/168.2.399](https://doi.org/10.1093/mnras/168.2.399).
- [65] E. Witten, “Cosmic separation of phases”, Phys. Rev. D 30 (1984) 272–285. doi:[10.1103/PhysRevD.30.272](https://doi.org/10.1103/PhysRevD.30.272).
- [66] A. Boyarsky, M. Drewes, T. Lasserre, S. Mertens, O. Ruchayskiy, “Sterile neutrino Dark Matter”, Prog. Part. Nucl. Phys. 104 (2019) 1–45. doi:[10.1016/j.ppnp.2018.07.004](https://doi.org/10.1016/j.ppnp.2018.07.004).
- [67] R. K. Leane, “Indirect Detection of Dark Matter in the Galaxy” (2020). [arXiv:2006.00513](https://arxiv.org/abs/2006.00513).
- [68] C. Pérez de los Heros, “Status, Challenges and Directions in Indirect Dark Matter Searches”, Symmetry 12 (2020). doi:[10.3390/sym12101648](https://doi.org/10.3390/sym12101648).
- [69] O. Buchmueller, C. Doglioni, L.-T. Wang, “Search for dark matter at colliders”, Nature Phys. 13 (2017) 217–223. doi:doi.org/10.1038/nphys4054.
- [70] R. Bähre *et al.*, “Any light particle search II — Technical Design Report”, J. Instrum. 8 (2013) T09001. doi:[10.1088/1748-0221/8/09/T09001](https://doi.org/10.1088/1748-0221/8/09/T09001).
- [71] D. S. Akerib *et al.*, “Snowmass2021 Cosmic Frontier Dark Matter Direct Detection to the Neutrino Fog” (2022). [arXiv:2203.08084](https://arxiv.org/abs/2203.08084).
- [72] J. Aalbers *et al.*, “DARWIN: towards the ultimate dark matter detector”, J. Cosm. Astropart. Phys. 2016 (2016) 017. doi:[10.1088/1475-7516/2016/11/017](https://doi.org/10.1088/1475-7516/2016/11/017).
- [73] XENON Collaboration, E. Aprile *et al.*, “Search for Coherent Elastic Scattering of Solar ${}^8\text{B}$ Neutrinos in the XENON1T Dark Matter Experiment”, Phys. Rev. Lett. 126 (2021) 091301. doi:[10.1103/PhysRevLett.126.091301](https://doi.org/10.1103/PhysRevLett.126.091301).
- [74] SuperCDMS Collaboration, R. Agnese *et al.*, “Search for low-mass dark matter with CDMSlite using a profile likelihood fit”, Phys. Rev. D 99 (2019) 062001. doi:[10.1103/PhysRevD.99.062001](https://doi.org/10.1103/PhysRevD.99.062001).
- [75] DAMIC Collaboration, A. Aguilar-Arevalo *et al.*, “Results on Low-Mass Weakly Interacting Massive Particles from an 11 kg d Target Exposure of DAMIC at SNOLAB”, Phys. Rev. Lett. 125 (2020) 241803. doi:[10.1103/PhysRevLett.125.241803](https://doi.org/10.1103/PhysRevLett.125.241803).
- [76] EDELWEISS Collaboration, E. Armengaud *et al.*, “Searching for low-mass dark matter particles with a massive Ge bolometer operated above ground”, Phys. Rev. D 99 (2019) 082003. doi:[10.1103/PhysRevD.99.082003](https://doi.org/10.1103/PhysRevD.99.082003).

- [77] CRESST Collaboration, A. H. Abdelhameed *et al.*, “First results from the CRESST-III low-mass dark matter program”, Phys. Rev. D 100 (2019) 102002. doi:10.1103/PhysRevD.100.102002.
- [78] CRESST Collaboration, G. Angloher *et al.*, “Results on sub-GeV dark matter from a 10 eV threshold CRESST-III silicon detector”, Phys. Rev. D 107 (2023) 122003. doi:10.1103/PhysRevD.107.122003.
- [79] SuperCDMS Collaboration, I. Alkhateb *et al.*, “Light Dark Matter Search with a High-Resolution Athermal Phonon Detector Operated above Ground”, Phys. Rev. Lett. 127 (2021) 061801. doi:10.1103/PhysRevLett.127.061801.
- [80] SENSEI Collaboration, L. Barak *et al.*, “SENSEI: Direct-Detection Results on sub-GeV Dark Matter from a New Skipper CCD”, Phys. Rev. Lett. 125 (2020) 171802. doi:10.1103/PhysRevLett.125.171802.
- [81] EDELWEISS Collaboration, Q. Arnaud *et al.*, “First Germanium-Based Constraints on Sub-MeV Dark Matter with the EDELWEISS Experiment”, Phys. Rev. Lett. 125 (2020) 141301. doi:10.1103/PhysRevLett.125.141301.
- [82] DAMIC Collaboration, A. Aguilar-Arevalo *et al.*, “Constraints on Light Dark Matter Particles Interacting with Electrons from DAMIC at SNOLAB”, Phys. Rev. Lett. 123 (2019) 181802. doi:10.1103/PhysRevLett.123.181802.
- [83] SuperCDMS Collaboration, R. Agnese *et al.*, “First Dark Matter Constraints from a SuperCDMS Single-Charge Sensitive Detector”, Phys. Rev. Lett. 121 (2018) 051301. doi:10.1103/PhysRevLett.121.051301.
- [84] SuperCDMS Collaboration, D. W. Amaral *et al.*, “Constraints on low-mass, relic dark matter candidates from a surface-operated SuperCDMS single-charge sensitive detector”, Phys. Rev. D 102 (2020) 091101. doi:10.1103/PhysRevD.102.091101.
- [85] XENON Collaboration, E. Aprile *et al.*, “Light Dark Matter Search with Ionization Signals in XENON1T”, Phys. Rev. Lett. 123 (2019) 251801. doi:10.1103/PhysRevLett.123.251801.
- [86] P. Agnes *et al.*, “Search for dark matter particle interactions with electron final states with DarkSide-50” (2022). arXiv:2207.11968.
- [87] PandaX-II Collaboration, C. Cheng *et al.*, “Search for Light Dark Matter–Electron Scattering in the PandaX-II Experiment”, Phys. Rev. Lett. 126 (2021) 211803. doi:10.1103/PhysRevLett.126.211803.

- [88] DAMIC-M Collaboration, I. Arnquist *et al.*, "First Constraints from DAMIC-M on Sub-GeV Dark-Matter Particles Interacting with Electrons", Phys. Rev. Lett. 130 (2023) 171003. doi:10.1103/PhysRevLett.130.171003.
- [89] M. Battaglieri *et al.*, "US Cosmic Visions: New Ideas in Dark Matter 2017: Community Report" (2017). arXiv:1707.04591.
- [90] P. Adari *et al.*, "EXCESS workshop: Descriptions of rising low-energy spectra", SciPost Phys. Proc. (2022) 001. doi:10.21468/SciPostPhysProc.9.001.
- [91] A. Aguilar-Arevalo *et al.*, "Confirmation of the spectral excess in DAMIC at SNOLAB with skipper CCDs" (2023). arXiv:2306.01717.
- [92] CDMS Collaboration, D. S. Akerib *et al.*, "First Results from the Cryogenic Dark Matter Search in the Soudan Underground Laboratory", Phys. Rev. Lett. 93 (2004) 211301. doi:10.1103/PhysRevLett.93.211301.
- [93] CDMS Collaboration, D. S. Akerib *et al.*, "Limits on Spin-Independent Interactions of Weakly Interacting Massive Particles with Nucleons from the Two-Tower Run of the Cryogenic Dark Matter Search", Phys. Rev. Lett. 96 (2006) 011302. doi:10.1103/PhysRevLett.96.011302.
- [94] CDMS Collaboration, Z. Ahmed *et al.*, "Search for Weakly Interacting Massive Particles with the First Five-Tower Data from the Cryogenic Dark Matter Search at the Soudan Underground Laboratory", Phys. Rev. Lett. 102 (2009) 011301. doi:10.1103/PhysRevLett.102.011301.
- [95] SuperCDMS collaboration, R. Agnese *et al.*, "Search for Low-Mass Weakly Interacting Massive Particles Using Voltage-Assisted Calorimetric Ionization Detection in the SuperCDMS Experiment", Phys. Rev. Lett. 112 (2014) 041302. doi:10.1103/PhysRevLett.112.041302.
- [96] SuperCDMS Collaboration, R. Agnese *et al.*, "New Results from the Search for Low-Mass Weakly Interacting Massive Particles with the CDMS Low Ionization Threshold Experiment", Phys. Rev. Lett. 116 (2016) 071301. doi:10.1103/PhysRevLett.116.071301.
- [97] SuperCDMS Collaboration, R. Agnese *et al.*, "Results from the Super Cryogenic Dark Matter Search Experiment at Soudan", Phys. Rev. Lett. 120 (2018) 061802. doi:10.1103/PhysRevLett.120.061802.
- [98] M. F. Albakry *et al.*, "A Strategy for Low-Mass Dark Matter Searches with Cryogenic Detectors in the SuperCDMS SNOLAB Facility" (2022). arXiv:2203.08463.

- [99] S. Yellin, "Finding an upper limit in the presence of an unknown background", Phys. Rev. D 66 (2002) 032005. doi:10.1103/PhysRevD.66.032005.
- [100] S. Yellin, "Extending the optimum interval method" (2007). arXiv:0709.2701.
- [101] J. Billard, E. Figueroa-Feliciano, L. Strigari, "Implication of neutrino backgrounds on the reach of next generation dark matter direct detection experiments", Phys. Rev. D 89 (2014) 023524. doi:10.1103/PhysRevD.89.023524.
- [102] F. Ruppin, J. Billard, E. Figueroa-Feliciano, L. Strigari, "Complementarity of dark matter detectors in light of the neutrino background", Phys. Rev. D 90 (2014) 083510. doi:10.1103/PhysRevD.90.083510.
- [103] SENSEI Collaboration, O. Abramoff *et al.*, "SENSEI: Direct-Detection Constraints on Sub-GeV Dark Matter from a Shallow Underground Run Using a Prototype Skipper CCD", Phys. Rev. Lett. 122 (2019) 161801. doi:10.1103/PhysRevLett.122.161801.
- [104] K. Ramanathan, N. Kurinsky, "Ionization yield in silicon for eV-scale electron-recoil processes", Phys. Rev. D 102 (2020) 063026. doi:10.1103/PhysRevD.102.063026.
- [105] C. Stanford, M. J. Wilson, B. Cabrera, M. Diamond, N. A. Kurinsky, R. A. Moffatt, F. Ponce, B. von Krosigk, B. A. Young, "Photoelectric absorption cross section of silicon near the bandgap from room temperature to sub-Kelvin temperature", AIP Advances 11 (2021) 025120. doi:10.1063/5.0038392.
- [106] C. Chang, C. Hu, R. W. Brodersen, "Quantum yield of electron impact ionization in silicon", J. Appl. Phys. 57 (1985) 302–309. doi:10.1063/1.334804.
- [107] K. Ramanathan, personal communication, September 23, 2022.
- [108] SuperCDMS Collaboration, M. F. Albakry *et al.*, "First Measurement of the Nuclear-Recoil Ionization Yield in Silicon at 100 eV", Phys. Rev. Lett. 131 (2023) 091801. doi:10.1103/PhysRevLett.131.091801.
- [109] J. Lindhard, V. Nielsen, M. Scharff, P. V. Thomsen, "Integral equations governing radiation effects. (Notes on atomic collisions, III)", Kgl. Danske Videnskab., Selskab. Mat. Fys. Medd. 33 (1963).
URL <https://www.osti.gov/biblio/4701226>
- [110] R. Ren *et al.*, "Design and characterization of a phonon-mediated cryogenic particle detector with an eV-scale threshold and 100 keV-scale dynamic range", Phys. Rev. D 104 (2021) 032010. doi:10.1103/PhysRevD.104.032010.

- [111] W. A. Page, "Searching for Low-Mass Dark Matter with SuperCDMS Soudan Detectors", Ph.D. thesis, The University of British Columbia (2019).
URL <https://www.slac.stanford.edu/exp/cdms/ScienceResults/Theses/bpage.pdf>
- [112] B. S. Neganov, V. N. Trofimov, "Possibility of producing a bulky supersensitive thermal detector at a temperature close to absolute zero", Sov. J. Exp. Theor. Phys. 28 (1978) 328.
- [113] P. N. Luke, "Voltage-assisted calorimetric ionization detector", J. Appl. Phys. 64 (1988) 6858–6860. doi:10.1063/1.341976.
- [114] M. J. Wilson, "A New Search for Low-mass Dark Matter and an Examination and Reduction of the Uncertainty due to the Photoelectric Absorption Cross Section using a Cryogenic Silicon Detector with Single-charge Sensitivity", Ph.D. thesis, University of Toronto (2022).
URL <https://www.osti.gov/biblio/1887835>
- [115] H. J. Maris, "Phonon propagation with isotope scattering and spontaneous anharmonic decay", Phys. Rev. B 41 (1990) 9736–9743. doi:10.1103/PhysRevB.41.9736.
- [116] M. H. Kelsey *et al.*, "G4CMP: Condensed matter physics simulation using the Geant4 toolkit", Nucl. Instrum. Methods Phys. Res. A: Accel. Spectrom. Detect. Assoc. Equip. 1055 (2023) 168473. doi:doi.org/10.1016/j.nima.2023.168473.
- [117] K. D. Irwin, S. W. Nam, B. Cabrera, B. Chugg, B. A. Young, "A quasiparticle-trap-assisted transition-edge sensor for phonon-mediated particle detection", Rev. Sci. Instrum. 66 (1995) 5322–5326. doi:10.1063/1.1146105.
- [118] S. L. Watkins, "Athermal Phonon Sensors in Searches for Light Dark Matter", Ph.D. thesis, University of California, Berkeley (2022).
URL <https://www.slac.stanford.edu/exp/cdms/ScienceResults/Theses/watkins.pdf>
- [119] L. N. Cooper, "Bound Electron Pairs in a Degenerate Fermi Gas", Phys. Rev. 104 (1956) 1189–1190. doi:10.1103/PhysRev.104.1189.
- [120] S. A. Kivelson, D. S. Rokhsar, "Bogoliubov quasiparticles, spinons, and spin-charge decoupling in superconductors", Phys. Rev. B 41 (1990) 11693. doi:10.1103/PhysRevB.41.11693.
- [121] SuperCDMS Collaboration, R. Agnese *et al.*, "Projected sensitivity of the SuperCDMS SNOLAB experiment", Phys. Rev. D 95 (2017) 082002. doi:10.1103/PhysRevD.95.082002.

- [122] R. Romani *et al.*, "Thermal detection of single e-h pairs in a biased silicon crystal detector", *Appl. Phys. Lett.* 112 (2018) 043501. doi:10.1063/1.5010699.
- [123] F. Ponce *et al.*, "Modeling of Impact Ionization and Charge Trapping in SuperCDMS HVeV Detectors", *J. Low Temp. Phys.* 199 (2020) 598–605. doi:10.1007/s10909-020-02349-x.
- [124] F. Ponce *et al.*, "Measuring the impact ionization and charge trapping probabilities in SuperCDMS HVeV phonon sensing detectors", *Phys. Rev. D* 101 (2020) 031101. doi:10.1103/PhysRevD.101.031101.
- [125] M. J. Wilson, A. Zaytsev, B. von Krosigk, "Catalog of single-electron-hole-pair solutions for the exponential charge trapping and impact ionization mode", in preparation.
- [126] M. J. Wilson, private communication (Aug. 2023).
- [127] Z. Hong *et al.*, "Single Electron-Hole Pair Sensitive Silicon Detector with Surface Event Rejection", *Nucl. Instrum. Methods Phys. Res. A: Accel. Spectrom. Detect. Assoc. Equip.* 963 (2020) 163757. doi:10.1016/j.nima.2020.163757.
- [128] N. Kurinsky, "The Low-Mass Limit: Dark Matter Detectors with eV-Scale Energy Resolution", Ph.D. thesis, Stanford U., Phys. Dept. (2018).
URL <https://www.slac.stanford.edu/exp/cdms/ScienceResults/Theses/kurinsky.pdf>
- [129] N. I. Fisher, "Statistical Analysis of Circular Data", Cambridge University Press, 1993.
- [130] SuperCDMS Collaboration, M. F. Albakry *et al.*, "Investigating the sources of low-energy events in a SuperCDMS-HVeV detector", *Phys. Rev. D* 105 (2022) 112006. doi:10.1103/PhysRevD.105.112006.
- [131] F. J. Kerr, D. Lynden-Bell, "Review of galactic constants", *Mon. Not. R. Astron. Soc.* 221 (1986) 1023. doi:10.1093/mnras/221.4.1023.
- [132] M. C. Smith *et al.*, "The RAVE survey: constraining the local Galactic escape speed", *Mon. Not. R. Astron. Soc.* 379 (2007) 755. doi:10.1111/j.1365-2966.2007.11964.x.
- [133] R. Schönrich, J. Binney, W. Dehnen, "Local kinematics and the local standard of rest", *Mon. Not. R. Astron. Soc.* 403 (2010) 1829. doi:10.1111/j.1365-2966.2010.16253.x.
- [134] R. Pincus, "Distribution of the Maximal Gap in a Sample and its Application for Outlier Detection", Springer Netherlands, 1984, pp. 90–91. doi:10.1007/978-94-009-6528-7_22.

- [135] S. Watkins, C. Fink, “RQpy”, GitHub repository (2018). Last accessed 9 August 2023.
URL <https://github.com/spice-herald/RQpy>
- [136] CRESST Collaboration, G. Angloher *et al.*, “Results on MeV-scale dark matter from a gram-scale cryogenic calorimeter operated above ground”, *Eur. Phys. J. C* 77 (2017) 637. doi:[10.1140/epjc/s10052-017-5223-9](https://doi.org/10.1140/epjc/s10052-017-5223-9).
- [137] DAMIC Collaboration, A. Aguilar-Arevalo *et al.*, “Search for low-mass WIMPs in a 0.6 kg day exposure of the DAMIC experiment at SNOLAB”, *Phys. Rev. D* 94 (2016) 082006. doi:[10.1103/PhysRevD.94.082006](https://doi.org/10.1103/PhysRevD.94.082006).
- [138] NEWS-G Collaboration, Q. Arnaud *et al.*, “First results from the NEWS-G direct dark matter search experiment at the LSM”, *Astropart. Phys.* 97 (2018) 54–62. doi:[10.1016/j.astropartphys.2017.10.009](https://doi.org/10.1016/j.astropartphys.2017.10.009).
- [139] J. I. Collar, “Search for a nonrelativistic component in the spectrum of cosmic rays at Earth”, *Phys. Rev. D* 98 (2018) 023005. doi:[10.1103/PhysRevD.98.023005](https://doi.org/10.1103/PhysRevD.98.023005).
- [140] J. I. Collar, F. T. Avignone, “Effect of elastic scattering in the Earth on cold dark matter experiments”, *Phys. Rev. D* 47 (1993) 5238–5246. doi:[10.1103/PhysRevD.47.5238](https://doi.org/10.1103/PhysRevD.47.5238).
- [141] C. Kouvaris, I. M. Shoemaker, “Daily modulation as a smoking gun of dark matter with significant stopping rate”, *Phys. Rev. D* 90 (2014) 095011. doi:[10.1103/PhysRevD.90.095011](https://doi.org/10.1103/PhysRevD.90.095011).
- [142] G. Zaharijas, G. R. Farrar, “Window in the dark matter exclusion limits”, *Phys. Rev. D* 72 (2005) 083502. doi:[10.1103/PhysRevD.72.083502](https://doi.org/10.1103/PhysRevD.72.083502).
- [143] B. J. Kavanagh, “Earth scattering of superheavy dark matter: Updated constraints from detectors old and new”, *Phys. Rev. D* 97 (2018) 123013. doi:[10.1103/PhysRevD.97.123013](https://doi.org/10.1103/PhysRevD.97.123013).
- [144] T. Emken, C. Kouvaris, “DaMaSCUS: the impact of underground scatterings on direct detection of light dark matter”, *J. Cosm. Astropart. Phys.* (2017) 031. doi:[10.1088/1475-7516/2017/10/031](https://doi.org/10.1088/1475-7516/2017/10/031).
- [145] M. S. Mahdawi, G. R. Farrar, “Closing the window on GeV Dark Matter with moderate (μb) interaction with nucleons”, *J. Cosm. Astropart. Phys.* (2017) 004. doi:[10.1088/1475-7516/2017/12/004](https://doi.org/10.1088/1475-7516/2017/12/004).
- [146] B. J. Kavanagh, “Verne”, astrophysics Source Code Library (2016). Last accessed 10 August 2023, doi:[10.5281/zenodo.7193430](https://doi.org/10.5281/zenodo.7193430).
URL <https://github.com/bradkav/verne>

- [147] G. D. Starkman, A. Gould, R. Esmailzadeh, S. Dimopoulos, “Opening the window on strongly interacting dark matter”, Phys. Rev. D 41 (1990) 3594–3603. doi:10.1103/PhysRevD.41.3594.
- [148] T. Emken, C. Kouvaris, “How blind are underground and surface detectors to strongly interacting dark matter?”, Phys. Rev. D 97 (2018) 115047. doi:10.1103/PhysRevD.97.115047.
- [149] J. H. Davis, “Probing Sub-GeV Mass Strongly Interacting Dark Matter with a Low-Threshold Surface Experiment”, Phys. Rev. Lett. 119 (2017) 211302. doi:10.1103/PhysRevLett.119.211302.
- [150] R. Essig, T. Volansky, T.-T. Yu, “New constraints and prospects for sub-GeV dark matter scattering off electrons in xenon”, Phys. Rev. D 96 (2017) 043017. doi:10.1103/PhysRevD.96.043017.
- [151] R. Essig, A. Manalaysay, J. Mardon, P. Sorensen, T. Volansky, “First Direct Detection Limits on Sub-GeV Dark Matter from XENON10”, Phys. Rev. Lett. 109 (2012) 021301. doi:10.1103/PhysRevLett.109.021301.
- [152] A. J. Biffl, “Simulating neutron backgrounds to rare event searches”, Ph.D. thesis, U. of Colorado (2023).
URL <https://www.slac.stanford.edu/exp/cdms/ScienceResults/Theses/biffl.pdf>
- [153] D. Bryman, J. Bueno, K. Davis, V. Kaminski, Z. Liu, D. Oldenburg, M. Pilkington, R. Sawyer, “Muon Geotomography — Bringing New Physics to Orebody Imaging”, Economic Geology Special publication (2014). doi:10.5382/SP.18.11.
- [154] J. Aalbers, “Robust new physics searches with unknown backgrounds”, Phys. Rev. D 106 (2022) 052006. doi:10.1103/PhysRevD.106.052006.
- [155] PandaX-II Collaboration, C. Fu *et al.*, “Limits on Axion Couplings from the First 80 Days of Data of the PandaX-II Experiment”, Phys. Rev. Lett. 119 (2017) 181806. doi:10.1103/PhysRevLett.119.181806.
- [156] N. Viaux, M. Catelan, P. B. Stetson, G. G. Raffelt, J. Redondo, A. A. R. Valcarce, A. Weiss, “Neutrino and Axion Bounds from the Globular Cluster M5 (NGC 5904)”, Phys. Rev. Lett. 111 (2013) 231301. doi:10.1103/PhysRevLett.111.231301.
- [157] M. M. Miller Bertolami, B. E. Melendez, L. G. Althaus, J. Isern, “Revisiting the axion bounds from the Galactic white dwarf luminosity function”, J. Cosm. Astropart. Phys. (2014) 069. doi:10.1088/1475-7516/2014/10/069.

- [158] T. Emken, R. Essig, C. Kouvaris, M. Sholapurkar, “Direct detection of strongly interacting sub-GeV dark matter via electron recoils”, *J. Cosm. Astropart. Phys.* (2019) 070. doi:10.1088/1475-7516/2019/09/070.
- [159] T. Emken, “DaMaSCUS-CRUST v1.1”, Computer software (2019). doi:10.5281/zenodo.2846401.
- [160] P. Galison, A. Manohar, “Two Z’s or not two Z’s?”, *Phys. Lett. B* 136 (1984) 279–283. doi:10.1016/0370-2693(84)91161-4.
- [161] B. Holdom, “Two U(1)’s and ϵ charge shifts”, *Phys. Lett. B* 166 (1986) 196–198. doi:10.1016/0370-2693(86)91377-8.
- [162] M. Kaplinghat, S. Tulin, H.-B. Yu, “Direct detection portals for self-interacting dark matter”, *Phys. Rev. D* 89 (2014) 035009. doi:10.1103/PhysRevD.89.035009.
- [163] R. Rudnick, S. Gao, “3.01 - Composition of the Continental Crust”, in: H. D. Holland, K. K. Turekian (Eds.), *Treatise on Geochemistry*, Pergamon, Oxford, 2003, pp. 1–64. doi:10.1016/B0-08-043751-6/03016-4.
- [164] SENSEI Collaboration, M. Crisler, R. Essig, J. Estrada, G. Fernandez, J. Tiffenberg, M. S. Haro, T. Volansky, T.-T. Yu, “SENSEI: First Direct-Detection Constraints on Sub-GeV Dark Matter from a Surface Run”, *Phys. Rev. Lett.* 121 (2018) 061803. doi:10.1103/PhysRevLett.121.061803.
- [165] P. Du, D. Egana-Ugrinovic, R. Essig, M. Sholapurkar, “Sources of Low-Energy Events in Low-Threshold Dark-Matter and Neutrino Detectors”, *Phys. Rev. X* 12 (2022) 011009. doi:10.1103/PhysRevX.12.011009.
- [166] R. Anthony-Petersen *et al.*, “A Stress Induced Source of Phonon Bursts and Quasi-particle Poisoning” (2022). arXiv:2208.02790.
- [167] D. Baxter, F. Wagner, “EXCESS workshop: a community effort towards understanding low energy excesses”, conference materials (2023). Last accessed 1 September 2023.
URL <https://indico.cern.ch/event/1199289/contributions/5449536/attachments/2706589/4698851/EXCESS%20workshop%20summary.pdf>